IST Project 2000-30129

Front-End Models for Silicon Future Technology

FRENDTECH

Deliverable (Public)

Public Final Report

The FRENDTECH Consortium

October 13, 2004

Contents

1 Introduction 2

2 Formation of Extended Defects 2

2.1 Structural Evolution of Extended Defects during Annealing 2
2.2 Extraction of Extended-Defect Parameters with a Genetic Algorithm 6
2.3 Modeling of Extended Defect Kinetics upon Annealing: Reduction of the Number of Equations and of the Calculation Time 10

3 Diffusion and Activation in Silicon 13

3.1 Direct Evidence of the Recombination of Silicon Interstitial Atoms at the Silicon Surface . . 13
3.2 Injection of Silicon Interstitial into the Substrate from Low Energy As Implantation 14
3.3 The Crucial Impact of the Oxygen Content on the Diffusion of Nitrogen Implanted in Silicon 17
3.4 Indium: Experimental Results and Modeling 19
3.5 Indium: *Ab Initio* Calculations 22
3.6 Quantitative Measurements of Two-Dimensional Ultra-Shallow B Profiles in Si 23
3.7 Extraction of the Binding Energy of Boron-Interstitial Clusters from Dedicated Experiments 28
3.8 Modeling the Formation of Ultra-Shallow Junctions after Non-Amorphizing Boron Implants 29
3.9 Solid Phase Epitaxy - Activation and Deactivation of Boron in Ultra-Shallow Junctions . . . 32
3.10 A Quest for BICs 34
3.11 Cluster Formation in Ultra–Low Energy High–Dose B^+–Implanted Si 36
3.12 Mechanisms of F effect on B Diffusion and Activation 38

4 Diffusion in SiGe and Strain Effects 43

4.1 Implantation and Diffusion of Boron in Germanium 43
4.2 Effects of Defect Injection on Sb Diffusion in Si and SiGe 45
4.3 Effects of Defect Injection on As Diffusion in Si and SiGe 45

5 Oxidation 47

5.1 On the Dry Oxidation Kinetics of Ultra-Thin Oxide 47
5.2 On the Simulation of Oxynitridation Process 49
5.3 High quality Ultra-Thin Oxides by Oxidation of Nitrogen-Implanted Silicon 57

6 Software development 60

7 Publications of the consortium 62

8 Contributors 66

References 68

1 Introduction

For the continuous miniaturization of silicon devices, various alternatives are tested during front-end process development. Because of the enormous costs of experimental validation, and to save time, technology-computer-aided design (TCAD) is used extensively in the industry. But the success of TCAD is limited when device simulation is based on incorrect doping distributions. However, the technological progress in the semiconductor industry is very rapid and predictive models needed for simulating advanced devices are required now in areas where they do not exist or where models are not sufficiently accurate to be used in industrial applications. A list of top priorities for such models has been specified by the leading European semiconductor manufacturers organized in the ESPRIT User Group “UPPER” [1]. Based on these top priorities, the European project FRENDTECH was initiated by the UPPER group. Its overall objective is to provide the European semiconductor industry with these missing top priority simulation models for front-end semiconductor processing. Driven by the demands of UPPER, models were developed in particular for diffusion and and oxidation.

In the following parts of this document, some of the findings are highlighted in dedicated contributions. For further information on the topics, please contact the person indicated at its end.

2 Formation of Extended Defects

2.1 Structural Evolution of Extended Defects during Annealing

It is well known that transient enhanced diffusion (TED) is one of the major obstacles to the achievement of ultra-shallow junctions. The reliable simulation of this physical phenomenon is one of the major objectives of the FRENDTECH project. TED is directly related (and controlled) by a concomitant phenomenon occuring in ion implanted silicon during annealing: the formation and evolution of extended defects. Actually, depending on dopant, dose, energy and annealing conditions, these defects may range from small interstitial clusters to $\{113\}$ defects and to perfect and faulted dislocation loops. This is why one of the project’s workpackages was entirely dedicated to the experimental study of defect formation in ion implanted silicon under both non-amorphising and amorphising implants. While providing a reliable experimental data base for the subsequent development of simulation models, this work has allowed us to clarify some controversial points concerning the defect evolution mechanism and, more importantly, to give a more general picture of this phenomenon.

Non-amorphising implants

In a first part of our activity, the evolution of $\{113\}$ defects in non-amorphised structures has been investigated under different implantation and annealing conditions, depending on which, $\{113\}$ defects may either grow and transform into dislocation loops, or completely dissolve during annealing. The experimental results have been discussed and critically compared to those already available in the literature.

$\{113\}$ defects dissolution

One of the experiments consisted in repeating the well known Eaglesham’s experiment [2] on the dissolution of $\{113\}$ defects. However, our experiment was run using CVD wafers (provided by IMEC-Philips) containing several boron marker layers, in order to directly compare the evolution of the extended defects to that of the enhaced diffusion. A special care has been devoted to the choice of the weak beam dark field (WBDF)

imaging conditions in the electron microscope. This is particularly important when very long {113} defects are present which, depending on their orientation, may intersect the TEM specimen surfaces. As an exemple, figure 1 shows TEM micrographs taken from the same area under different imaging conditons. In the case

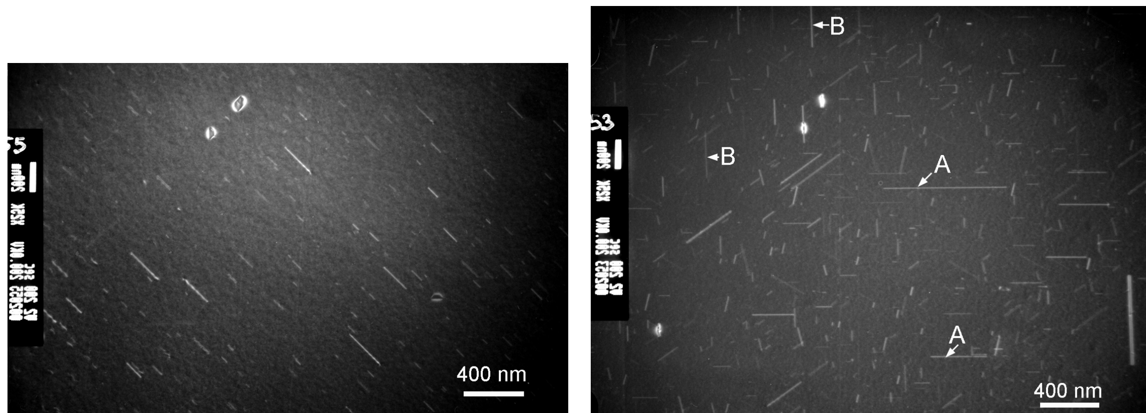

Figure 1: WBDF TEM micrographs from the same area of a sample annealed at 850°for 200 sec, using different imaging conditions. *(a)*: $\vec{B}$=[001], $\vec{g}$=<400>. *(b)*: $\vec{B}$=[113], $\vec{g}$=<442>.

of "conventional" conditions ($\vec{B}$=[001], $\vec{g}$=<400>, figure 1a) all the visible defects are inclined at 45°with respect to the sample surface. On the other hand, many more defects are visible in figure 1b ($\vec{B}$=[113], $\vec{g}$=<442>). Among these defects, only those appearing as horizontal or vertical lines on the micrograph (labelled A and B, respectively) are parallel to the specimen surface and their length can therefore be measured correctly. Indeed, a higher value of the average defect length is found when considering only these defects. A similar analysis has been carried out on all samples studied in this work, whenever necessary.

Figure 2a shows a comparison (number of atoms stored in the defects) of the experimental results found in this work (filled symbols) with those of Eaglesham et al. (empty symbols). Our results clearly indicate that the defect evolution and dissolution process is characterised by two separate regimes [3, 4]. In the first, a classical Ostwald ripening process occurs (increasing size, decreasing density), during which a weak interstitial loss from the defect band is observed. This is seen for instance at 700°between 15 min and 3 hours annealing time. Following this initial period, defect dissolution occurs very rapidly with a much higher dissolution rate than the one observed at the early stages of the annealing. It has to be noted that, although the two sets of results are in good agreement concerning the time required for achieving a complete defect dissolution, the data from Eaglesham clearly do not support our description of 2 different regimes leading to a complete defect dissolution. In addition, with the exception of the 815°data set, the dissolution rates found by Eaglesham is systematically higher than in our case (cf. different curves' slope in figure 2a). This result might suggest that the dissolution rate of {113} defects is not an intrinsic characteristics of the defects themselves, but depends on the combined effect of all process parameters (substrate type, implantation energy and dose, annealing ambient and temperature).

The discrepancy is more evident in figure 2b, where a linear time scale is used to plot the results found at 740°. The exponential fit of our data for annealing times up to 1h, clearly indicates that a much stronger dissolution mechanism must take place between 1h et 2h, with the number of atoms stored in the defects

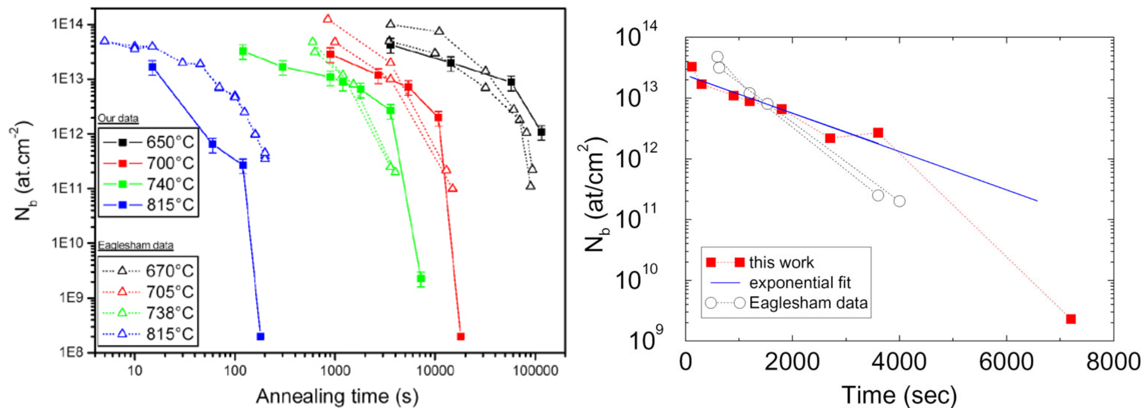

Figure 2: Time evolution of the number of atoms stored in {113} defects during annealing following Si^+ implantation at 40 keV to a dose of 6x10^{13} cm^{-2}: comparison with data from Eaglesham et al. [2]. (a) All temperatures. Log-log scale. (b) 740°. Linear-log scale.

decreasing by as much as 3 orders of magnitude. In contrast, it is suggested in ref. [2] that each data set can be fitted by a single exponential decay function throughout the annealing process.

Although a direct quantitative comparison of similar experiments performed in different laboratories is somehow a "dangerous" practice, we estimate that a more accurate analysis in the work of Eaglesham and co-workers, might have resulted is a similar {113} behaviour to that reported here. Indeed, with reference to their own data, Stolk et al. [5] suggested that the various uncertainties limiting the accurate defect measurement in the final stages of the {113} decay *"...could imply that the decay curves are not purely exponential, but are likely to be more convex instead"*. Indeed, predictive simulations based on the atomistic model developed within the consortium (shown elsewhere in this report), are in perfect agreement with the observed "2-regimes" dissolution behaviour.

{113}-to-DLs transformation

The transformation of {113} defects into dislocation loops has been studied in detail within the FRENDTECH project. In fact, due to the different formation energies associated to the two defect types, their relative contribution to the total defect population may have a strong impact on the TED measured during annealing in these structures.

A first set of experiments [6] showed that, whenever observed, the transformation is always progressive, i.e. the two defect populations coexist during annealing and, more importantly, long {113} defects are still observed even after long annealing times when the vast majority of defects already consist of dislocation loops. The results were explained in terms of an energy barrier limiting the defect transformation process, suggesting that the annealing temperature plays a crucial role in determining the defect transformation rate.

In a more recent experiment, we have implanted Si wafers with Si^+ions at a fixed energy and different non-amorphising doses. The implanted samples were annealed using different conditions but with similar thermal budget. All samples were implanted and annealed at IMEL, Athens.

An exemple is given in figure 3 showing TEM images obtained after annealing at 800°7 min for three different implantation doses. It is found that for the lowest implant dose (5x$10^{13}$$cm^{-2}$) only {113} defects

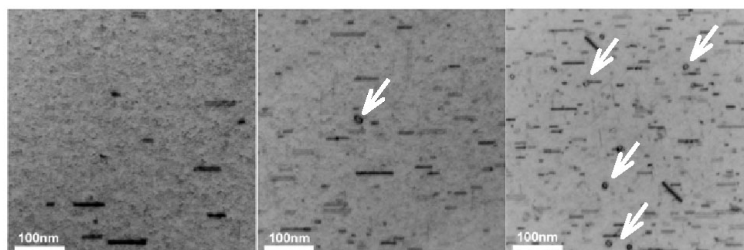

Figure 3: Weak Beam Dark Field images from samples implanted with Si^{+}ions at 100 keV and annealed in N_2 at 800°for 7 min. *(a)* 5x10^{13}cm^{-2}. *(b)* 1x10^{14} cm^{-2}. *(c)* 2x10^{14} cm^{-2}.

are found, whereas for an intermediate dose of 1x10^{14}cm^{-2} isolated dislocation loops are already formed (white arrows in figure 3b). Their density clearly increases with the implanted dose, as seen in figure 3c for a dose of 2x10^{14}cm^{-2}. In addition, the overall defect density increases with the implanted dose. The same behaviour is found for similar thermal budgets at lower temperatures, with the lowest dose implanted sample always exhibiting {113} defects only.

These results give a more complete picture of the {113}-to-DLs transformation process, clarifying the role played by the various experimental parameters. Indeed, for a starting 100% {113} s population, two conditions are required in order to trigger the transformation process: *(i)* during annealing, the {113} defects have to grow up to sizes at which the transformation into DLs is energetically favourable (cf. formation energy vs. defect size plots, [7]). The defect growth rate is clearly controlled by the thermal budget (temperature, time) used for the annealing step. *(ii)* for a {113} defect "ready" to transform, the interstitial exchange rate with the surrounding supersaturation field must be high enough to increase the probability of the defect to overcome the energy barrier for the transformation. This condition is fulfilled when the defect population density is sufficiently high to sustain the equilibrium with the surrounding supersaturation field. However, as it was mentioned above, when the defect density decreases below a critical level during annealing, the interstitial flow towards the recombining surface "breaks" this equilibrium and the defects enter the dissolution regime. The implant dose therefore plays a crucial role by determining the defect density at the beginning of the anneal.

Preliminary simulations that consider the presence of both defect type in the defect population, are in qualitative agreement with the observed results. However, quantitative analysis of these experiments will certainly constitute a database for further improvements of the defect kinetics model to be carried out after the end of this project.

Amorphising implants

Because of the increasing interest for the use of a preamorphisation step in conjunction with ultralow energy boron implantation to achieve ultrashallow junctions, dedicated experiments were carried out within the project to gain knowledge on the evolution of the extended defects formed during annealing of preamorphised silicon and to evaluate the possible extension of the atomistic model (initially developed for non-amorphising implants) to this different experimental conditions.

TEM studies of the defect evolution indicated that, independently of the experimental conditions used, the extended defects formed after a preamorphisation step (EOR defects) exhibit a similar behaviour to that found in the case of non-amorphising implants. At low annealing temperature (625°), they only consist

of {113} defects despite the high amount of excess interstitials introduced during the preamorphisation step. A higher temperature is necessary to trigger their transformation into dislocation loops of two types. An exemple is given in figure 4, in which the {113}-to-DLs transformation is investigated in preamorphised structures provided by Mattson Thermal Products [8,9]. Following SPE at low temperature, selected samples

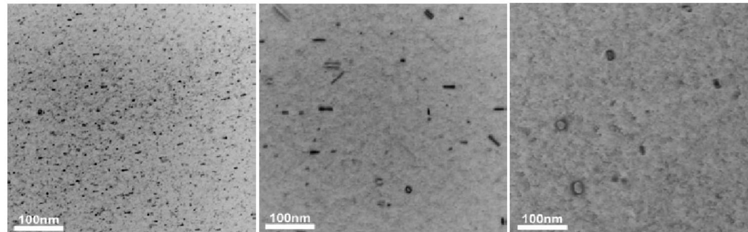

Figure 4: Weak Beam Dark Field images from samples implanted with 30 keV $Ge^{+}$to a dose of $1x10^{15}cm^{-2}$, followed by 0.5 keV B^{+}at $1x10^{15}cm^{-2}$ and initially annealed at 650°for 5 sec. Subsequent post-anneal was carried out at 800°. *(a)* 10 sec. *(b)* 120 sec. *(c)* 900 sec.

were post-annealed at 800°. Similarly to the case of non-amorphising implants, an initially 100% {113} population progressively transforms into dislocation loops (virtually no {113} s are left after 900 sec anneal, see figure 4c). TEM analysis of post-annealed samples at different temperatures (not shown) reveals that the transformation occurs for all the investigated temperatures, with a transformation rate rapidly increasing with temperature, in agreement with the description given above. These observations give a further evidence that no fundamental difference exists between amorphised and non-amorphised structures with respect to the formation and evolution of extended defects.

Finally, this similarity in the defect evolution mechanism in both non-amorphising and amorphising implants, has also been observed in TED measurements. As an exemple, figure 5 shows the comparison between diffusion enhancements measured after non-amorphising implants [10] (black symbols and lines) for different annealing temperatures and after amorphising implants (blue symbols). These results clearly indicate that, similarly to the case of non-amorphising implants, in the early stages of a low temperature anneal, the interstitial supersaturation in a preamorphised structure is dominated by small interstitial clusters that evolve into {113} defects, with no further decrease in the supersaturation until defect dissolution occurs. This conclusion is particularly interesting, when considering that, despite the various differences in the experimental conditions, the two studies give virtually the same results. Indeed, in this work the structures have been preamorphised (no amorphisation in Cowern's work), a high Si dose has been implanted ($6x10^{15}$ cm^{-2} vs. $2x10^{13}$ cm^{-2} in ref. [10]) and the defects are very far from the surface (790 nm vs. 60 nm).

It is therefore possible to conclude that the atomistic model initially developed within the consortium for the case of non-amorphising implants can be extended to the case in which preamorphisation is performed, provided the effect of a moving a/c interface is also included in the model in order to correctly simulate the interstitial depth distribution during SPE, especially at the early stages of a low temperature anneal.

For further information, please contact F. Cristiano, CEMES/LAAS-CNRS (fuccio@laas.fr).

2.2 Extraction of Extended-Defect Parameters with a Genetic Algorithm

Extraction of parameters plays an important role in the development of physically based models. Indeed, process and device simulations all require valid input parameters for their results to be adequate. However,

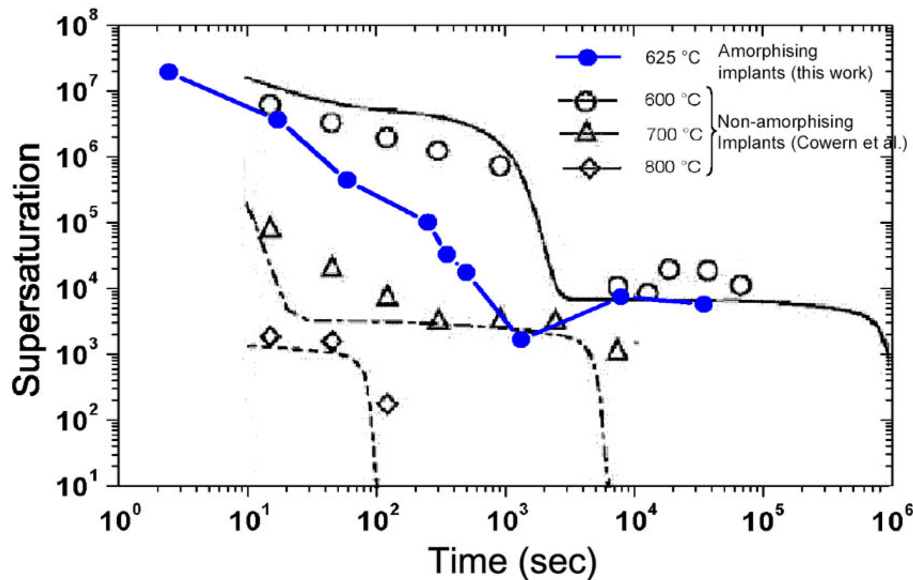

Figure 5: *(a)* Comparison between diffusion enhancements measured after non-amorphising implants (black symbols and lines, various annealing temperatures) and amorphising implants (blue symbols, 400 keV Si^{+}6x10^{15}cm^{-2}, 625°).

extraction of parameters is not always an easy task and can be CPU time consuming, especially when several parameters have to be extracted at the same time from the measured data. Genetic Algorithms (GA) are robust search algorithms based on the theory of natural selection and evolution. The advantage of GA is that it balances the need for exploitation and exploration in the search space. The GA uses the concept of solutions encoded as binary strings where a bit is analogous to a gene and the string is analogous to a chromosome. A population of strings (i.e. individuals or solutions) is initialized at random and evolves to the next generation by genetic operators such as selection, crossover and mutation. The fitness function is used to evaluate each of the solutions in the population. In this work we used a genetic algorithm to extract parameters that play a major role in the modeling of boron TED. It is now well-known that boron TED is strongly influenced by the presence of {113} defects and smaller self-interstitial clusters that maintain a high interstitial supersaturation in their vicinity. Therefore, it is of main importance to know parameters related to their kinetics.

A one–dimensional model accounting individually for the formation of small self-interstitial clusters as well as the formation of {113} defects was implemented in PROMIS 1.5 since the other tools available within the consortium were at that time not able to handle the several hundred equations required for a full physical description. This simulator was linked to the GA developed by T. Fühner [11] at Fraunhofer IISB in order to extract parameters such as the binding energies of small self-interstitial clusters ($n < 9$ atoms), the stacking–fault energy of {113} defects, as well as the self–diffusivity of silicon via self–interstitials at different temperatures. Different types of experimental data, obtained under different experimental conditions, were combined in the same optimization strategy in order to eliminate unphysical solutions and find the optimum set of parameters. These data included, on one hand, the evolution of the self-interstitial supersaturation measured by Cowern et al. [12] at 600°and 800°following a Si^{+} implantation of 2x10^{13}cm^{-2}at

40 keV and, on the other hand, the mean size evolution of 113 defects obtained by transmission electronic microscopy (TEM) analysis obtained by CEMES/LAAS-CNRS within FRENDTECH [13]. TEM measurements were carried out on samples implanted with Si^+ at 40 keV for a dose of $6x10^{13}cm^{-2}$and annealed at 740°.

Figure 6 shows an excellent agreement between experimental supersaturation at 600 and 800°and simulations after optimization of the parameters (dashed line). The ultrafast TED phase, the steep drop of the

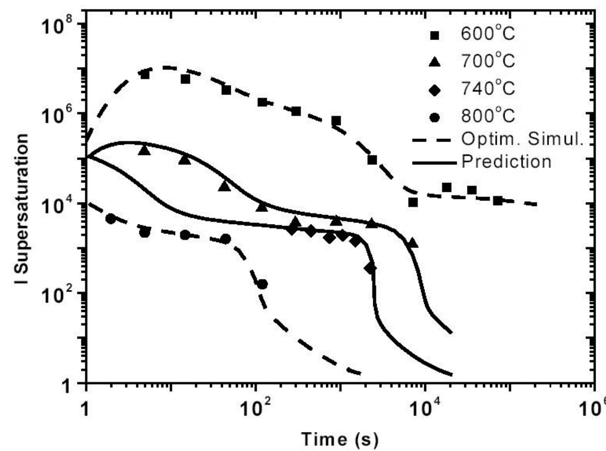

Figure 6: Comparison between experimental supersaturation, simulations after optimization (dashed line) and predictions with the optimized set of parameters (solid lines).

supersaturation at 600°and the plateau region are very well described by the model. Taking into account uncertainties that are inherent to TEM analysis, a good agreement is also obtained between the simulated (dashed line) and experimental mean size for a temperature of 740°, as can be seen on figure 7. The extracted values for the formation energies (figure 8) of small clusters ($n<10$) exhibit two minima at n=4 and n=8. This confirms what Cowern et al. [12] found with a zero-dimensional model. Also, the value found for the asymptotical formation energy of very large 113 defects (0.7 eV) is in good agreement with recent works [14–16].

To test the validity of the model as well as the consistency of the extracted parameters, the calibrated model was then used to simulate independent experimental Supersaturation/TEM results obtained in different works [12, 13, 17, 18]. Figure 6 clearly shows the very good agreement between the measured and the predicted (solid line) I supersaturation at 700 and 740°, using the previously optimized set of parameters. Also, on figure 7 we reported the prediction (solid line) for the mean size evolution obtained by Eaglesham et al. [17] at 815°for an implantation dose of $5x10^{13}cm^{-2}$. Again, the evolution of the extended defects is well predicted by the model, demonstrating the consistency of the parameters set. Finally, figure 9 presents simulations of the defect density as a function of depth. The simulations are compared to recent experimental results obtained by Colombeau et al. [18] on samples implanted with Si^+ at 40 keV for a dose of $6x10^{13}cm^{-2}$and annealed at 740°for 15 and 45 min. As evidenced by figure 9, the model is able to predict the overall density decrease due to Ostwald Ripening of the defects, but also the shift of the defect depth distribution towards larger depths for long annealing times. This last result is a consequence of the preferential dissolution of defects located near the surface, where interstitials recombine at high velocity.

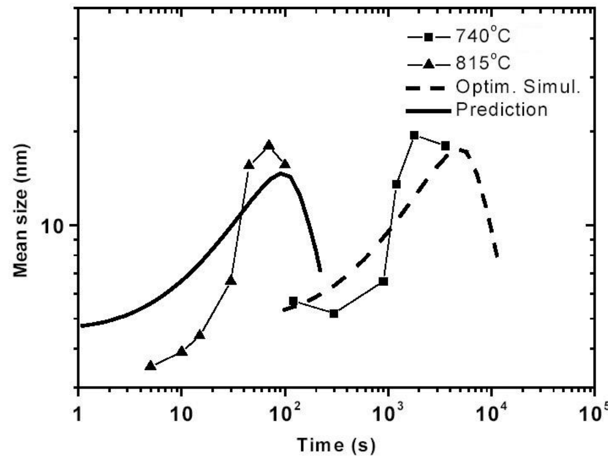

Figure 7: Comparison between experimental mean size evolution, simulation after optimization (dashed line) and prediction with the optimized set of parameters (solid line).

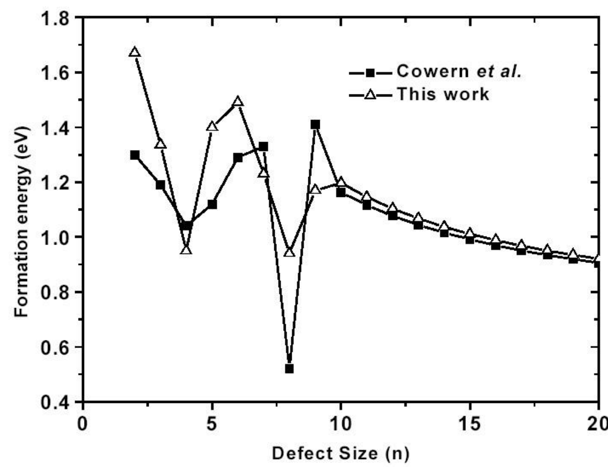

Figure 8: Formation energy of defects extracted by GA optimization (triangles) and from Cowern et al. [12] (squares).

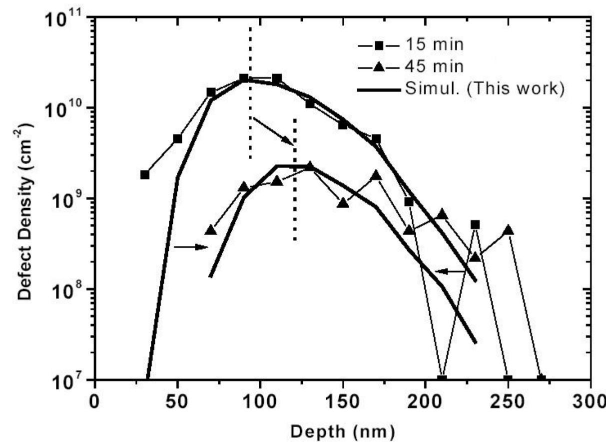

Figure 9: Comparison between experimental defect depth distribution and simulations at 740°for two different annealing times.

In conclusion, we used a genetic algorithm for the extraction of parameters related to {113} defect kinetics. GA offers flexibility and efficiency in the search of parameters and will be used in our future work to extract parameters such as binding energies of BICs from SIMS and SRP profiles. A full account of the work can be found in [19].

For further information, please contact P. Pichler, Fraunhofer IISB (peter.pichler@iisb.fraunhofer.de).

2.3 Modeling of Extended Defect Kinetics upon Annealing: Reduction of the Number of Equations and of the Calculation Time

The modeling of the kinetics of extended defects upon annealing is no more a problem for the partners of FRENDTECH: a well-established modeling has been implemented in 0D[1] and in 1D (see above). This modeling is based on the resolution of a system of $N_{\max}$ equations where $N_{\max}$ is the maximum defect size for example equal to 10000. The modeling has been and is currently being validated by testing the evolution of the supersaturation of interstitials, the mean size of the defects and even the evolution of concomitant B profiles. However, the integration of the model in FLOOPS can not be envisaged with such a high number of equations and the calculation time should also be not prohibitive for the future user. Moreover, the optimisation of the parameters used in the model requires short calculation times which is not the case for the 0D program. Therefore we have worked on the 0D program to reduce the number of equations to be solved and decrease the calculation time. The methods were applied to a case where small clusters and {113} defects are considered (not the dislocation loops).

The calculation time was first reduced by changing the resolution method following a suggestion from C. Ortiz. The initial method was a Runge-Kutta one which is adpated to the solution of systems of ordinary differential equations in general. It has been replaced by a direct method more adapted to the specifics of the problem, the Choleski method. The results of the calculation with the two methods are shown on Fig. 10

[1] Ion Implantation Group, LAAS-CEMES, Toulouse

for the supersaturation of free Si interstitials, Fig. 11 for the density of entended defects and Fig. 12 for the size histogram (red and green curves respectively). The results of the simulation are identical even for the quantity of atoms in the defects and the mean number of atoms per defects (not shown). The gain in CPU time is considerable: from nearly 3 hours with the Runge Kutta method to 6 mn with the Choleski one.

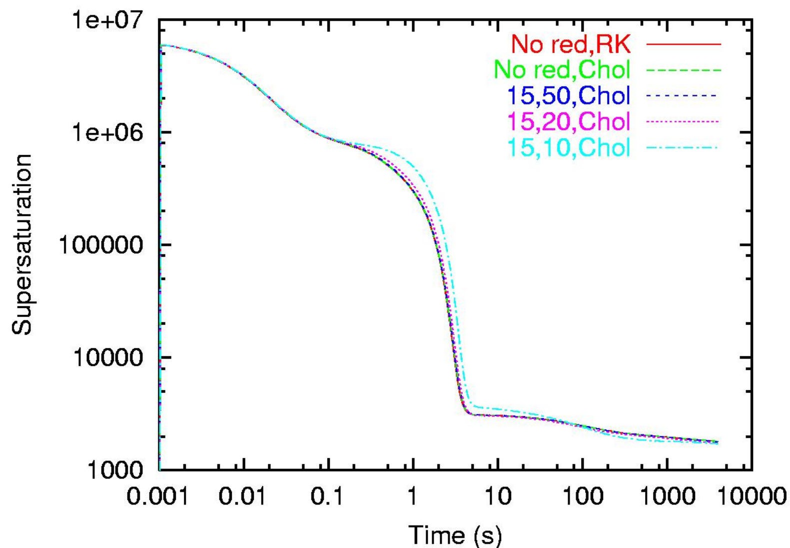

Figure 10: Supersaturation of Si interstitials at the extended defects depth during annealing at 740 ° C.

The number of differential equations was then reduced following an original proposal from N. Cowern[2]. The idea is to solve exactly the small sizes (n=2 to 15 typically), and then apply a reduction method in 4 steps :

- Start from the discrete size variable n and density N_n
- Render them continuous and call them x for the size variable and $\rho(x)$ for the density
- Change to a logarithmic scale, with size variable u and density $\rho(u)$
- Discretize u to allow the implementation

The figures 10 to 12 show the results with 10, 20 or 50 points in the reduced region. The size histogram is well approximated and the supersaturation and the decrease of the density of extended defects is perfectly given by 15+20 equations, and even not so bad for 15+10 equations. The reduction is thus considerable: 10000 to 35 equations. The calculation time is reduced to 5s.

The drastic reduction of the calculation time (factor $\approx$ 2000) and of the number of equations (factor $\approx$ 300) for the 0D program is very promising for the integration of the modeling of extended defects in FLOOPS.

For further information, please contact E. Lampin, ISEN/IEMN (Evelyne.Lampin@isen.iemn.univ-lille1.fr).

[2] ATI, Surrey Univ, Guildford

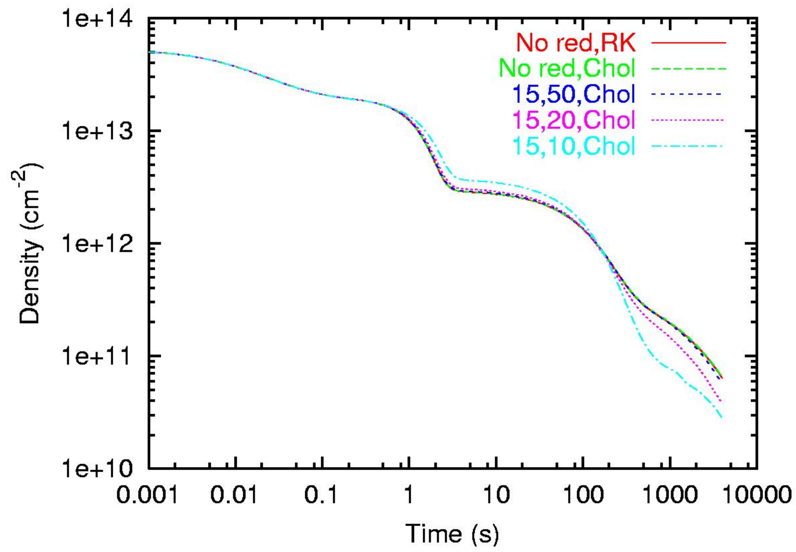

Figure 11: Density of extended defects during annealing at 740 ° C.

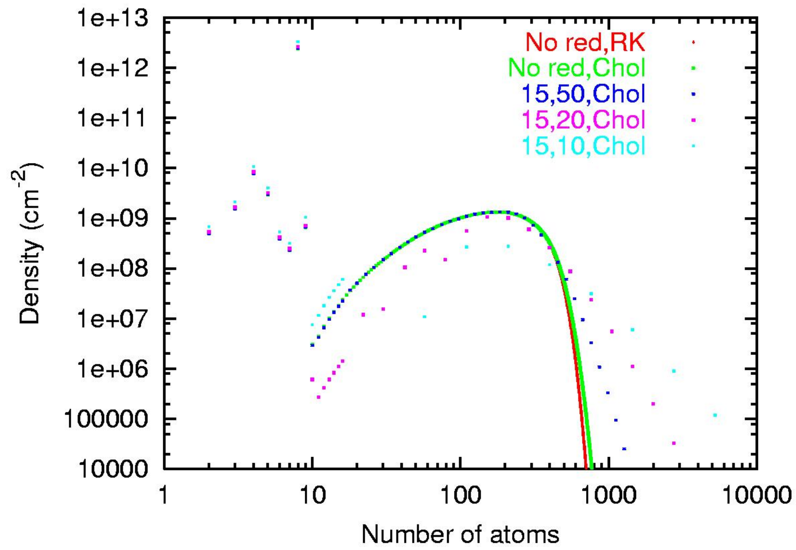

Figure 12: Histogram of size (N_n) of the extended defects after 10s of annealing.

3 Diffusion and Activation in Silicon

3.1 Direct Evidence of the Recombination of Silicon Interstitial Atoms at the Silicon Surface

The silicon surface has long been suspected to play an important role on the TED evolution. Indeed, some experiments on defect evolution [20, 21] or boron diffusion [22, 23] have indirectly shown that the surface is an effective trap for silicon interstitial atoms. Based on these experimental results, the atomistic model developed within our consortium assumes that a gradient of the depth distribution of the Si interstitial supersaturation exists between the defect region and the surface, as schematically shown in figure 13. The

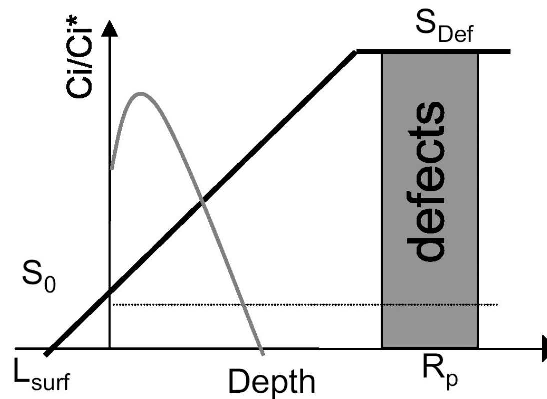

Figure 13: Depth variation of the amplitude of the Si_{int}s supersaturation in the surface region.

consequent interstitial flux is finally responsible for the complete defect dissolution during thermal annealing. However, no direct evidence of this gradient was yet available. In addition, in some works [24, 25], it is still proposed that the capture efficiency of the surface is negligible. We have therefore carried out a boron TED study using CVD Si structures (provided by Infineon Technologies, Munich) containing several boron marker layers, in order to evaluate the Si interstitial supersaturation at different depths in the substrate [26]. This approach has allowed us to confirm that the surface is an efficient trapping site for $Si_{int}s$ and, more importantly, to give a first direct evidence of the $Si_{int}s$ supersaturation gradient between the defect region and the surface.

Figure 14a shows boron profiles measured in the as-grown structure and after annealing at 850°for 15 sec and 300 sec, following a Si^+implantation at 100 keV to a dose of $2x10^{14}cm^{-2}$. Of the four boron marker layers, only the second one at 0.4 μm is located within the defect region. A qualitative analysis of the SIMS profiles clearly indicates that the deep marker layers (at 0.7 μm and 1 μm, respectively) diffuse more than those located closer to the surface. A fitting method based on the interstitial kick-out mechanism of B diffusion [27] has been used to extract the diffusion enhancement, D_B/D_B^*, corresponding to each B marker layer for all the annealing time intervals. In addition, the diffusion enhancement gives a direct measurement of the silicon interstitial supersaturation: $D_B/D_B^* = C_i/C_i^* = S$. The results are reported in figure 14b, where the variation of the diffusion enhancement is reported as a function of depth for the various time intervals studied. It is found that for all annealing times the diffusion enhancement is highest for the two deepest delta layers (located below the defect band) and gently decreases towards the surface. If we

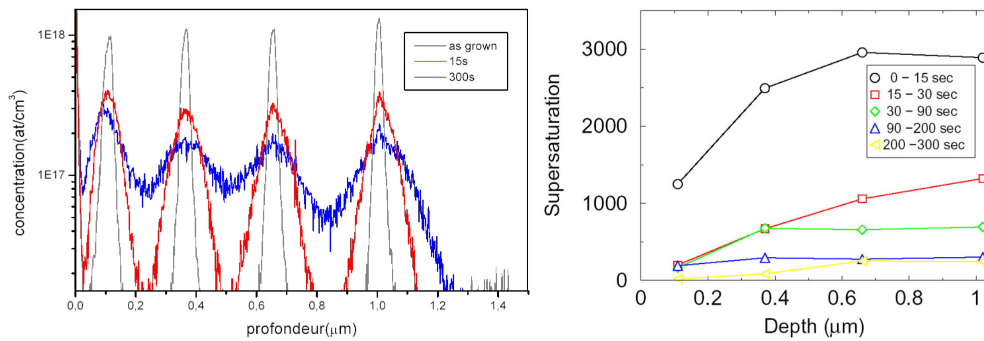

Figure 14: *(a)* Boron depth distribution profiles following Si^+implantation at 100 keV to a dose of 2x10^{14}cm^{-2}and annealing at 850°. *(b)* Diffusion enhancement of B marker layers during annealing at 850°following Si^+implantation at 100 keV to a dose of 2x10^{14}cm^{-2}.

consider that the diffusion enhancement coincides with the interstitial supersaturation, this figure represents a direct measurement of the interstitial supersaturation gradient between the defect band and the surface.

According to the schematic description of figure 13, the extrapolation of the $Si_{int}s$ supersaturation level above the silicon surface allows the estimation of the surface recombination length, L_{surf}, that is the mean free path travelled on the surface by a Si interstitial atom before recombining. Our results indicate an upper limit of about 200 nm for the surface recombination length at an annealing temperature of 850°, in agreement with the values proposed by previous TED simulation studies [23, 28].

For a further confirmation of this result, our atomistic model was used to simulate the measured supersaturation levels (figure 14b). The simulated $S(t)$ curve was then coupled to the set of equations for the B kick-out diffusion through a generation/recombination term in the diffusion equation of the Si self-interstitials [28]. This coupling was made in the process simulator IMPACT developed at IEMN (prior to the model transfer to FLOOPS-ISE).

Figure 15a shows the corresponding depth profile of B and $Si_{int}s$ after 30 s. The agreement between the calculated and measured B profiles is evident. In particular, the flat $Si_{int}s$ profile below the defect region is the result of the assumption that no $Si_{int}s$ traps are present in the bulk of high-quality CVD layers. The good agreement with the measured B profiles clearly justifies this choice. On the other hand, the gradient in the $Si_{int}s$ concentration profile between the defect region and the surface exhibits a linear decrease (see figure 15b plotted using a linear concentration scale), therefore validating our initial description for the surface recombination mechanism.

For further information, please contact F. Cristiano, CEMES/LAAS-CNRS (fuccio@laas.fr).

3.2 Injection of Silicon Interstitial into the Substrate from Low Energy As Implantation

High-dose, low energy arsenic implantation is a process that is typically used for the formation of S/D regions in silicon transistors. Relatively to other dopants such boron and phosphorus, fewer studies have been performed for the TED of arsenic [29, 30]. This is mainly because these effects are of moderate intensity at high temperatures and are more significant for very shallow junction, less than 100nm. In addition, research

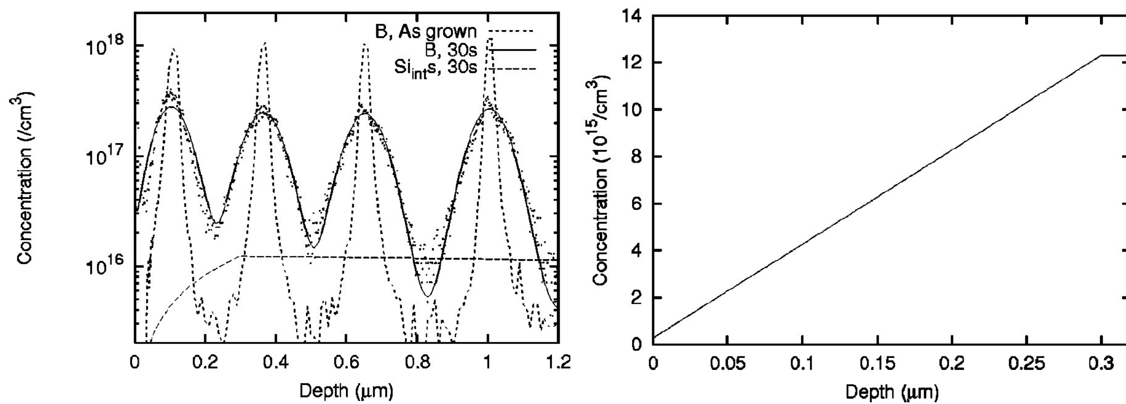

Figure 15: *(a)* B and Si_{int}s profiles after annealing at 850°for 30 s. Dashed line: reference as-grown profile. Dotted lines: measured profile (SIMS). Solid line: simulated profiles (fully coupled method). The points are the measurements. The lines are the simulations with the full coupled model. Longdashed line: $Si_{int}s$ profile.*(b)* Simulated Siints profile (linear time-scale) after annealing at 850°for 30 s.

on arsenic is generally associated with high concentrations, where Fermi level dependence of dopant diffusion and point defects introduced by clustering or precipitation complicate the analysis of the implantation induced TED. Our objective is to investigate the damage generated by low-energy, high dose As implantation performed at room temperature.

Silicon wafers containing two boron δ- layers at depth of 600 and 1100 nm respectively were implanted with arsenic at energies of 3, 10 and 25 KeV and dose of 1-2$\times 10^{15}$ cm^{-2} . The boron layers were grown by Philips and their concentration was of the order of 1×10^{18} cm^{-2} cm^{-3}. Silicon etching was performed at very low temperatures by a two step process [31]: (a) During the first step the samples are immersed into the oxidizing solution (H_2O_2), where an oxide in formed on the silicon surface. (b) During the second step the samples as immersed in an HF solution, that dissolves the formed oxide. The amount of the etched silicon was dependent on the location of the amorphous / crystalline interface and varies as a function of the implantation energy. Subsequently, the samples were annealed in RTA at 900°C for various times in inert ambient. RTA anneals were performed by Mattson.

Figure 16 shows SIMS profile of the Boron δ-layers. From this figure we can notice that the broadening of the Boron δ-layers is, with experimental error, independent of the etching process.

In order to have a more clear idea of the obtained results it is useful to discuss about the various mechanisms that influence point defect kinetics in the case of low energy implanted silicon. It is accepted that the Transient Enhanced Diffusion (TED) is due to the interstitial supersaturation induced by the implantation damage. An interstitial supersaturation is maintained during the Ostwald ripening process that is taking place during the formation and evolution of the extended defects. When the band of the defects is located away from the surface the ripening process is conservative and the number of bounded interstitials within the loops remains almost constant. This number represents the recoiled interstitials survived the recombination with vacancies at the crystalline part. This is the part of the implantation damage responsible for anomalous dopant diffusion. However, when the surface is very close to the defect band the ripening process is non - conservative since the surface is a strong sink for interstitials. From our experiments we expect that decreasing the distance between the defect band and the surface would lead to a reduction of the interstitial

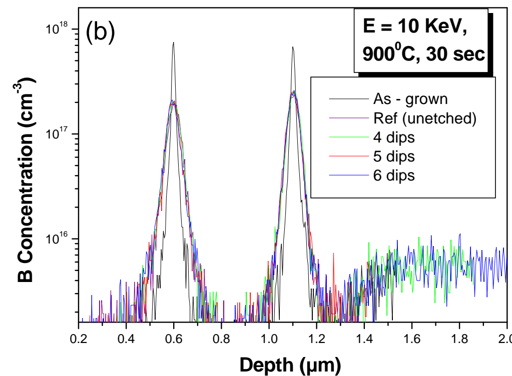

Figure 16: Boron δ-layer profiles after the etching and annealing process at 900°C in samples implanted with arsenic at 10 KeV with dose $\times 10^{15}$ cm^{-2}.

supersaturation, and of the enhanced diffusion of boron δ - layers. However, no such differences in the diffusion of the boron profile were observed. This indicates that the TED of boron is not only due to the supersaturation maintained during defect evolution.

There are two more sources for point defects, especially in the case on high arsenic concentration. When the arsenic concentration exceeds the solid solubility of arsenic in silicon, arsenic clustering may occur. Electrical activation studies have attributed arsenic clusters to be the cause of dopant deactivation in silicon [32]. These studies have also determined a critical concentration for arsenic cluster formation, which is a function of the annealing temperature. Theoretical studies and experimental evidence indicate that As clusters form around a vacancy with the consequent injection of silicon interstitials. The proposed mechanism can be described by the reaction

$$nAs \Longleftrightarrow As_n V + I \tag{1}$$

where n assumes values between 2 and 4.

In a recent work, Solmi et al [33] estimated that about one third of the TED observed in the first 20 min of annealing is due to the defects produced by clustering. It is very probable that this is the main mechanism that is responsible for TED in our experimental conditions. Another possible mechanism that might influence defect kinetics is As precipitation. It has been reported that extended defects at the projected range are absent when the arsenic concentration approaches the critical value for precipitation. This in probably due to vacancies released during SiAs precipitation leading to the annihilation for extended defects. However, the formation of SiAs precipitates is not very probable in our experimental conditions due to the very high values of the solid solubility of As in Si and the difficulty of nucleation of this conjugate phase.

For further information, please contact C. Tsamis, IMEL/NCSR ”Demokritos”
(C.Tsamis@imel.demokritos.gr).

3.3 The Crucial Impact of the Oxygen Content on the Diffusion of Nitrogen Implanted in Silicon

Nitrogen is currently attracting a broad interest in the semiconductor industry due to the possibility it offers to improve thin oxide reliability, prevent dopant penetration, silicide stability, and to control grown-in defects during the Si ingot growth. [34–36] Several theoretical studies have been performed in order to explain the preferred locations of the nitrogen atoms in the silicon lattice and some possible diffusion paths. [37–39] Moreover, from the experimental point of view, some striking discrepancies can be found for example between the mobility that allows nitrogen to diffuse out of the sample through the surface, as reported by Adam [40], and the partial immobility close to the surface, associated with long range diffusion (for several microns) into the bulk, reported by Hockett. [41]

Within the frame of FRENDTECH we explored the nitrogen diffusion by intentionally varying the impurity content of the silicon substrate in which nitrogen is implanted at medium energy. Our approach, not used so far in other experiments reported in the literature, allows one to learn more about the diffusion behaviour of nitrogen, through the establishment of the conditions under which nitrogen may diffuse easily at low temperatures for several microns or when the tendency for nitrogen to form complexes with impurities or itself prevails.

We used epitaxially grown Si layers (Epi), Float zone (FZ) and Czochralski (CZ) wafers with different concentrations of intrinsic contaminants, from the most pure Epi to the Cz material rich of C and O (i.e. [C] and [O] varied in the range $10^{15} - 10^{18}/\mathrm{cm}^3$). These samples were implanted with N and annealed in dry N_2 and characterized by chemical and electrical profiling, as well as by Deep Level Transient Spectroscopy (DLTS) in order to identify N associated levels in the Si bandgap.

As an example of the N diffusion behaviour, as a function of the purity of Si, Fig. 17 shows for a representative subset of times the diffusion behaviour of nitrogen in Cz-Si, in comparison with Epi-Si. At 750°C nitrogen is immobile in Epi-Si, whereas it diffuses in the first 30 min for several microns in Cz-Si. An increase in the thermal budget causes the evolution of the peak into a double structure with a dip in the middle (see the curve for 850°C 120 s in Cz-Si). When this happens, the surface-near peak does not act as a source of N for diffusion anymore, since nitrogen contained in the peak region is stabilised into complexes resistant to break-up. Therefore the nitrogen in the bulk of the wafer starts to be influenced by the surface and out-diffuses. In the Epi-Si case the clusters are slowly emitting mobile N, so there is still a source of N from the peak towards the bulk of the wafer. While the diffusion in Cz-Si reproduces closely that reported by Hockett, [41] in Epi-Si the nitrogen diffusion behaviour is completely different. It is remarkable that up to 750°C 30min nitrogen is immobile in Epi substrates, whereas for the same thermal treatment it diffuses for $\simeq 8\mu m$ into the bulk in Cz-Si. Moreover, the peaks located at $\simeq 3\mu m$ in Cz-Si are not present at all in Epi-Si after similar annealings; at depths beyond the maximum these peaks show a first order exponential decay with a decay length of $\simeq 3\mu m$ after 2 h at 750°C and $\simeq 2.8\mu m$ after 120 s at 850°C. In Epi-Si, when nitrogen diffuses, the profiles show a similar first-order exponential decay.

In Fz substrates, where the O content is comparable to that in Epi, the diffusion of N would represent an intermediate case. If carbon affects the nitrogen diffusivity, one would expect a diffusion behavior similar to that of Cz-Si while diffusion should be similar to that of Epi if oxygen mediates nitrogen diffusion. After careful SIMS analysis we observed that, regardless of the process parameters, nitrogen diffusion in Fz closely reproduced the diffusion in Epi. In particular, we never observed the double-peak structure as in Cz-Si.

From the comparison of Cz, Fz and Epi materials it is certainly possible to conclude that the nitrogen solubility limit, which in silicon is generally very poor, is significantly increased in the presence of oxygen; moreover, high concentration of oxygen (in Cz-Si) causes relevant nitrogen diffusion either through the formation of some energetically favoured complex or by an enhanced release of mobile point defects from

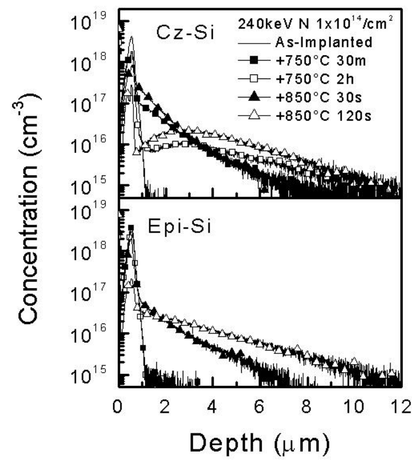

Figure 17: SIMS profiles of nitrogen implanted at 240keV to a dose of $1 \times 10^{14}\text{cm}^{-2}$ into Si substrates of variable purity and annealed simultaneously at high temperature.

the near-surface peak.

In order to further reduce the impact of N-N complexes and (eventually) enhance that of O concentration on N diffusion, our work included the study of implants with dose one order of magnitude lower than that reported in Fig. 17 (i.e. $1 \times 10^{13}/\text{cm}^2$) (see Fig. 18). Although the nitrogen peak was now as low as $4 \times 10^{17}/\text{cm}^3$ in this case, we have observed the same diffusive behaviour of nitrogen as that reported in Fig. 17. In fact, N out-diffuses from the peak at a level of one order of magnitude lower than the higher dose implant case. This fact suggests that clusters formed in the peak have similar stability regardless of the implant dose in the investigated range.

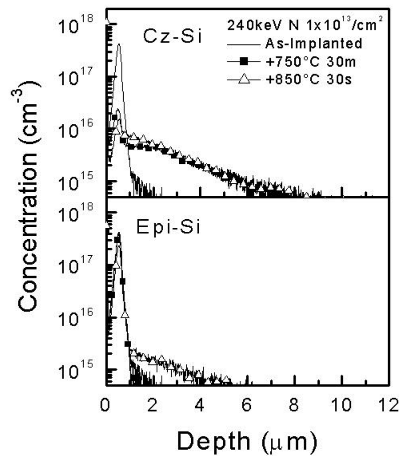

Figure 18: SIMS profiles of nitrogen implanted at 240 keV to a dose of $1 \times 10^{13}\text{cm}^{-2}$ into Si substrates of variable purity and annealed simultaneously at high temperature.

In the work of Itoh and Abe [42] it was assumed that the diffusion of nitrogen proceeds as a bound nitrogen pair. However, such a pair was previously identified as the dominant immobile complex of nitrogen in silicon and therefore an alternative to the diffusion of N_2 as a pair was proposed to be the dissociation of N_2 into mobile nitrogen interstitials. Our findings are in contrast with these conclusions and depict a new scenario for the N diffusion. In fact, the double-peaked diffusion profile is not necessarily caused only by the formation and breaking of N_2 pairs, being the anomaly of diffusion absent in pure epitaxial Si substrates, where oxygen is absent. It seems rather evident that the nitrogen profile shape strongly depends instead on oxygen concentration, through the formation of nitrogen-oxygen complexes. [43]

For further information, please contact V. Privitera, IMM-CNR (vittorio.privitera@imm.cnr.it).

3.4 Indium: Experimental Results and Modeling

The study of indium as p-type dopant in silicon has recently gained an increasing interest due to the shallow and steep doping profile, which can be obtained by implantation because of the heavy mass of In ions. However, concerning the electrical activation, the use of In as p-dopant could have some limitations due to incomplete ionisation caused by its relatively deep-lying acceptor level. [44] An improvement of indium electrical activation can be achieved by means of C co-implantation. [45] Within the FRENDTECH activity, silicon wafers were implanted with In or co-implanted with In and C. As an example, Fig. 19 show the comparisons between the chemical In profiles measured in samples implanted with 183 keV In or co-implanted with In and 33 keV C, after 900°C thermal annealing.

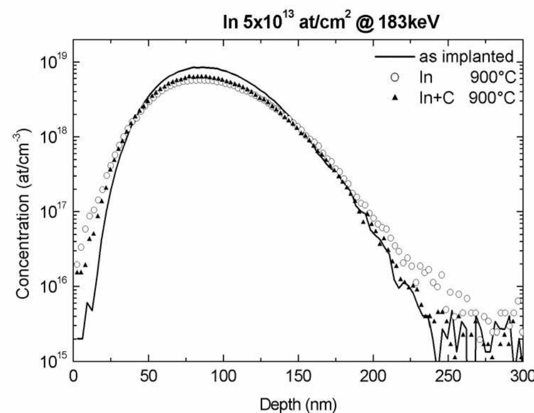

Figure 19: In profiles measured by SIMS for In implanted samples (with and without C co-implantation, before and after thermal annealing at 900°C for 30 s.

Indium diffusion is reduced when C is co-implanted, as suggested by the peak shrinking and increase, whereas the carrier concentration profiles in the implanted and co-implanted samples, measured by Spreading Resistance Profiling (SRP) after annealing at 900°C (Fig. 20), show a huge difference in the electrical activation: the active residual In fraction is 4% for the single In implant and rises up to 28% in the case of C co-implantation.

This enhancement in the electrical activation along with the reduction of the In diffusion and the shrinkage of the C profile can be explained by the formation of InC pairs. C immobilizes In by forming such complexes, which play a role in the enhanced electrical activation, due to the shallower level they introduce into the Si band gap ($E(\text{InC}) = E_v + 0.111$ eV), with respect to the rather deep level ($E(\text{In}) = E_v + 0.156$ eV) of In alone. [46]

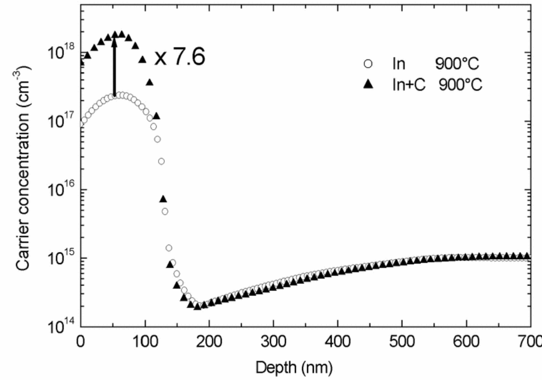

Figure 20: Carrier concentration profiles of the implanted and co-implanted samples measured by SRP after annealing at 900°C for 30 s).

In order to quantify this scenario, we developed and integrated in FLOOPS [47] a model, aimed to simulate both the TED and electrical activation of In implanted into Si in the presence of C contamination.

In the model, the evolution of the density of unpaired In, C_{In}, is ruled by the following equations, which couple C_{In}, the density C_X of the native defects (X = I or V), the density C_{YX} of the YX pairs (Y= C or In) and the density C_{InC} of the InC pairs:

$$\begin{aligned}\dot{C}_{In} &= -R_{InI} - R_{InV} - R^{CI}_{InC} \\ \dot{C}_{InC} &= R^{InI}_{InC} + R^{CI}_{InC} \\ \dot{C}_{InX} &= \nabla\left[D_{InX}\nabla C_{InX}\right] + R_{InX} - R^{InX}_{InC} \quad ;\end{aligned}$$

here $\dot{C} = \partial C/\partial t$ and the reaction terms R are given by

$$\begin{aligned}R_{InX} &= 4\pi D_X a_{Si}\left[C_{In}C_X - K_{In,X}C_{InX}\right] \\ R^{InI}_{InC} &= F_{InI,C}\left[C_{InI}C_C - K_{InI,C}C_{InC}\right] \\ R^{CI}_{InC} &= F_{CI,In}\left[C_{CI}C_{In} - K_{CI,In}C_{InC}\right] \quad ,\end{aligned}$$

where a_{Si} is the Si lattice spacing. $K_{A,B}$ is the binding parameter, which depends on the energy gain through an Arrhenius type expression $K_{A,B} = K^0_{A,B} \times exp[-E_b(A,B)/kT]$. $F_{A,B}$ is the formation rate of the InC reaction, which we consider activated-like, i.e., $F_{A,B} = D_A a_{Si} F^0_{A,B} \times exp[-E_a(A,B)/kT]$. The diffusivity of the mobile pairs D_{XY} can be expressed in terms of the defect equilibrium density C^*_X and the equilibrium diffusivity D^*_{In} by $D^*_{In} = C^*_I D_{InI}/K_{In,I} + C^*_V D_{InV}/K_{In,V}$.

Model parameters have been taken from the literature or calculated *ab initio*, as described in the following section. Since In and InC complex introduce two relatively deep levels into the Si band gap, the active fraction of the residual In dose is dependent on In and InC profiles. In order to derive the active profile from the density profiles C_{In} and C_{InC} we considered the following expression for the active dose N^- as function of the Fermi level E_F

$$N^- = C_{In}\,(1+g_{In}\times\exp\{[E(\mathrm{In})-E_F]/kT\})^{-1} + \\ + C_{InC}\,(1+g_{InC}\times\exp\{[E(\mathrm{InC})-E_F]/kT\})^{-1} \quad , \tag{2}$$

where the degeneracy factors are $g_{In}=4$ and $g_{InC}=2$ for the spherical In^- and non-spherical InC^- states. We can insert the above expression in the Poisson equation

$$\Delta\Phi = -q\,\varepsilon^{-1}\times(p-N^-) \tag{3}$$

for the potential $q\Phi=(E_F-E_v)$ and calculate numerically N^-. In Eq. 3 the hole density is $p=N_v\times exp(-q\Phi/kT)$, where N_v is the denstiy of states at the valence edge.

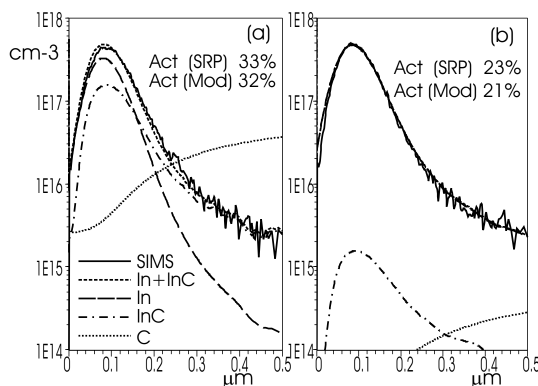

Figure 21: SIMS In profiles (solid line) obtained after thermal annealing at 900°C, 10 s (implanted dose $5\times10^{12}\mathrm{cm}^{-2}$, ion energy 180 keV, CZ (a) and EPI (b) substrates), together with simulated profiles: chemical In (i.e., In+InC) (small dashes), In (large dashes), InC (dots and dashes), C (dots).

In Fig. 21 the In profiles measured by SIMS, after 183 keV In implantation and annealing at $T=900$°C 10 s are shown for two types of Si substrates: (a) CZ silicon (p-type, 20-30 Ωcm) and (b) epitaxial (EPI) Silicon (p-type, 100 Ωcm) respectively. The C contamination background is in the range $10^{16}-10^{17}\mathrm{cm}^{-3}$ in the CZ-silicon and below $10^{15}\mathrm{cm}^{-3}$ in the EPI wafer. The simulated In chemical profiles (In+InC) are in excellent agreement with the SIMS one.

Furthermore, we calculated the active fraction using the simulated diffusion profile as input for the activation model (Eqs. (1,2)). This procedure gives electrically active fractions of $\sim 21\%$ and $\sim 32\%$ for the EPI and CZ wafers, respectively, in good agreement with the experimental values.

For further information, please contact V. Privitera, IMM-CNR (vittorio.privitera@imm.cnr.it).

3.5 Indium: *Ab Initio* Calculations

Our work [48] was also aimed to fill the lack of atomistic theoretical investigations on In defects in silicon, providing a well-founded *ab initio* picture of defect energetics and diffusivity over which a continuum diffusion model is built. From a first principle study of In interactions with native defects in silicon (performed within Density Functional Theory and using the Vienna Ab-Initio Simulation Package [49]), we obtained the energetics of different complexes formed by In with self-interstitial atoms (I) and vacancies (V), together with the relative diffusion parameters. We then integrated the *ab initio* results into the continuum model described above, to simulate the InC complex formation and allow the direct comparison with diffusion data.

We calculated the formation energy E_f of several q-charged defects starting from initial guessed geometries and relaxing at first the atomic forces until they are lower than $0.02\,\text{eV}/\text{Å}$. Then, E_f is obtained from the total energy E_{tot} of the supercell containing N_{Si} Si atoms and N_{In} In atoms, as $E_f = E_{tot} - \sum_i N_i \mu_i - q\mu_{\text{F}}$, where μ_i are the chemical potentials of the host and dopant specie and μ_{F} the Fermi level. We choose the cohesive energy of bulk silicon as μ_{Si}, while we fixed μ_{In} by setting the formation energy of substitutional In as the reference energy for all In-X^q defects (X=I,V). We considered also binding energies $E_b(\text{In-X})^q$, i.e. formation energy differences between initial and final products of reactions involving a In-X complex and isolated I, V, In_s defects, i.e. $\text{In}_\text{s}^{q_1} + \text{X}^{q_2} \rightarrow \text{In-X}^{q_1+q_2}$. We tested the convergence of the *ab initio* results with respect to all cut-off parameters, assigning a $\simeq 50$ meV accuracy to our calculated formation energies.

Among all In-related defect configurations containing an interstitial atom, the lowest energy structure for any values of μ_F consists of a In_s atom with a Si interstitial in a nearby tetrahedral (Td) position, shown in Fig.22*(a)* and denoted in the following as InI. The defect has formation energy $E_f(\text{InI}^0) = 2.6$ eV and binding energy $E_b(\text{InI}^0) = -1.2$ eV. The configurations with In sitting in the tetrahedral (In_{Td}) and the hexagonal (In_{Hx}) positions (Fig.22*(b,c)*) have larger formation energy with respect to InI. Other interstitial structures (In a bond-centered (In-BC) position between two silicon atoms, the mixed In-Si dumbbell configuration) are unstable and relax towards the InI geometry.

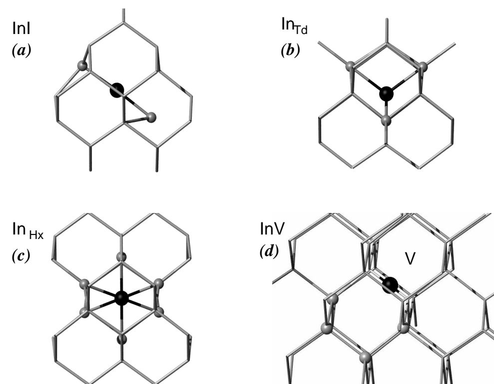

Figure 22: Relaxed configurations of neutral In-interstitial defects, InI, In_{Td} and In_{Hx} and InV (*(d)*). The In atom is shown as a black sphere, its nearest-neighbor Si atoms with smaller grey spheres.

In order to determine the activation energy for the interstitial-mediated diffusion process, we identified the migration path of the InI complex and located the saddle point with the aid of the Nudged Elastic Band (NEB) [50] method, capable to search the minimum energy path in the defect configurations space. The path

connecting two InI configurations centered on nearest-neighbor lattice sites has the In-BC configuration as saddle point configuration, with a small energy barrier ($\simeq$ 0.3 eV). To complete a diffusion step, the Si_{Td} moves around the In_s without dissociating and forms a new InI configuration oriented along a different $\langle 111 \rangle$ direction. This rearrangement has barrier energy $\simeq$ 0.6 eV, with Si_{Td} in the second nearest-neighbor (2nn) site of In_s as saddle point. Thus, the interstitial-mediated diffusion mechanism has activation energy $E_{act} = E_f + E_m \simeq 3.2$ eV.

The relaxed geometry of the neutral indium-vacancy complex (InV^0) is plotted in Fig.22(*d*). Starting from the ideal configuration with V and In_s on nearest-neighbor sites and checking against possible artificial symmetry-induced biases, we found that the atomic relaxations shift the In atom into a BC position between two empty lattice sites. The defect has formation energy $E_f(InV^0) = 1.48$ eV and binding energy $E_b(InV^0) = -2.4$ eV (considering the reaction $In_s^- + V^+ \rightarrow InV^0$). This value is larger than for other dopant-V complexes such as P-V, As-V eV. [51] Moreover, the shift of the dopant atom towards the BC site (found for the SnV complex, but not for the PV and AsV defects) suggests a strong bonding character of the InV complex that might be typical of dopant with large atomic radius. As regards charged In-V complexes, we found the same atomic relaxations as for InV^0.

In general, the first step of V-mediated diffusion mechanism is the exchange of atomic positions between In_s and Si-V. The Si-V moves then away up to the 3nn site and returns close to the In_s atom through jumps over different 2nn and 1nn sites on the hexagonal ring. The overall energy barrier is thus given by the energy difference ΔE between the InV and the 3nn configuration, plus the barrier for the 3nn $\rightarrow$ 2nn jump of the vacancy. Assuming with reasonable confidence that the latter is the migration energy of the isolated vacancy (E_m(Si-V) = 0.2 eV), we estimated the activation energy for the V-mediated pair diffusion. We found in fact that ΔE is roughly constant as a function of the Fermi energy, increasing by 0.2 eV in *p*-type doping conditions with respect to the $\Delta E = 1.9$ eV value of the intrinsic regime. Thus, $E_m = \Delta E + E_m$(Si-V) = 2.1 eV and the associated activation energy is $E_{act} = 3.6$ eV.

The results of the *ab initio* calculations have been used in FLOOPS, integrated with our InC model, as illustrated in the previous section. As an example, in Fig.23 we show the experimental chemical profile of 40 keV implanted indium, further annealed at $T = 800°$C for different times, $t = 20$ s (Fig.23*(a)*), $t = 5$ m (Fig.23*(b)*) and $t = 15$ m (Fig.23*(c)*), compared with the simulated profiles. The noteworthy agreement between the experimental data and the results of the modeling demonstrates the accuracy of our *ab initio* results and the validity of the present combined approach to model In diffusion.

For further information, please contact V. Privitera, IMM-CNR (vittorio.privitera@imm.cnr.it).

3.6 Quantitative Measurements of Two-Dimensional Ultra-Shallow B Profiles in Si

Within the frame of the FRENDTECH activity, the possibility to extract the active dopant distribution from the contour line, obtained by selective chemical etching in combination with Transmission Electron Microscopy (TEM), was explored.

While the one-dimensional characterisation techniques are well established and developed, the same cannot be claimed for two-dimensional analytical methods, that are of crucial importance to control the depth and the lateral distribution of the dopant atoms.

The selective chemical etching, combined with (TEM) [53–56] can be used after an appropriate sample preparation in order to obtain two dimensional (2D) profiling of doped silicon layers. Selective etching takes place only if the dopant is active, therefore a thermal process is required for the activation after the implant. We performed a characterisation of ultra-shallow B implanted layers in one-dimension by Secondary Ion

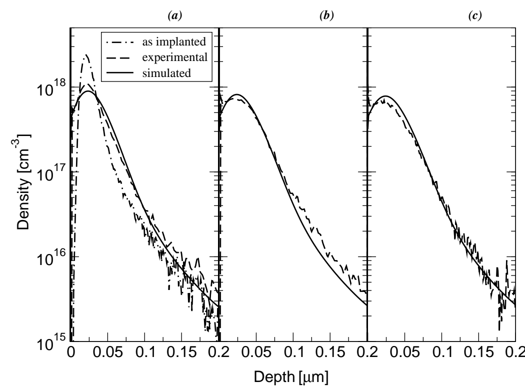

Figure 23: SIMS (dashed lines) and simulated (solid lines) In profiles obtained after thermal annealing at different times (see text). In the left graph the as-implanted profile is also shown (dots-dashed line).

Mass Spectrometry (SIMS) and Spreading Resistance Profiling (SRP) and in two-dimensions by TEM combined with selective etch. A model for the etching process is suggested and the main parameters which have to be taken into account are identified, in order to simulate the experimental data. We show that, by means of simulations, a quantitative correlation between the experimentally obtained etch depth and the active dopant distribution can be obtained.

A code based on the self-consistent coupling between an electrical device simulator (implementing the drift diffusion model) and a profile solver (a level-set method for evolving surfaces) [for a detailed description see Ref. [57]] was used to simulate the chemical etch process, in order to describe the effects of the etch solution on the different samples. In particular, the etch-depth dependence on the local electrical fields, forming at the interface between the solution and the surface of the sample and at the junction between the p-type dopant implant and the n-type silicon substrate, was investigated.

The 1D measurements obtained by SIMS and SRP are shown in fig. 24(a) and 24(b), respectively, in the case of 0.25 keV B implant before and after thermal processing at 1000°C for several times. We observe the presence of an immobile peak at the surface, even after 60 s annealing, related to B trapped by the implant damage. As a matter of fact, the SRP analysis shows that the surface B peak is not electrically active.

By comparing the chemical and the carrier concentration profiles, the electrical active fraction can be calculated, as reported in fig. 25, also for a 1 keV B implant. The electrical activation is obviously harder to achieve for lower implant energy due to the higher peak concentration: it ranges between 12% and 28% for the lower energy and between 22% and 38% for the higher energy implant. These information are necessary for the simulation work, since the electrically active dopant profile has to be used as the input in the etch process simulation.

The cross section TEM images achieved for a patterned sample implanted with 0.25 keV B and annealed at 1000°C for several times, after selective etching, are reported in fig. 26. The etch process takes place along the z-direction and the sample surface is protected by the glue used for the cross-TEM preparation. B diffusion with time is reflected by the TEM images, that show an expansion of the etched region in both y and x direction, with good spatial resolution. In most of the previous works, [54–57] the contourline defining the etched region was related to an isoconcentration doping level.

In principle, by measuring the lateral (y) and vertical (x) extension of the etched region, the dopant diffusion in both directions should be observed in a very direct way. However, we found that the sensitivity

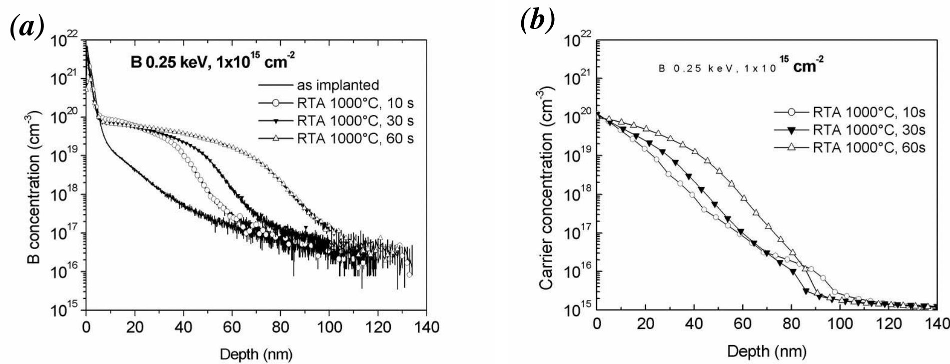

Figure 24: (a) SIMS profiles of a sample implanted with B $1\times10^{15}\mathrm{cm}^{-2}$ at 0.25 keV before and after thermal annealing at 1000°C for 10 s, 30 s and 60 s; (b) SRP profiles of the same sample after annealing.

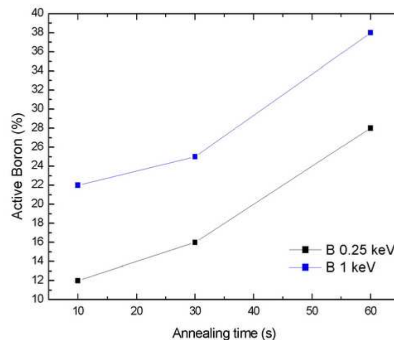

Figure 25: Electrically active fraction of $1\times10^{15}\mathrm{B/cm}^2$ implanted in Si at 0.25 keV and 1 keV after annealing at 1000°C, for different times.

of the technique is not a fixed parameter for all kinds of samples and, then, a quantification of the doping level corresponding to the contourline presents some uncertainties. Hence, we developed a model to correlate the etch process to the dopant distribution and to the local electrical fields, forming on the sample surface in contact with the solution.

Fig. 27 shows a simple diagram of the sample immersed in the etching solution. The p-doped, the n-doped regions and the depletion layer are indicated on the surface. The (x,y) plane is the surface in contact with the solution and an example of the time evolution of the eroded profile along the z direction during the etch process is shown. A TEM image of a patterned sample is reported in the inset, indicating the x, y, z directions. Simulations of the etching process were performed, following the evolution of the eroded profile versus the immersion time. The drift-diffusion code was initialised by means of the known donor (substrate doping level) and acceptor (implanted dopant) distributions measured by SRP after thermal annealing. The free charge availability at the interface rules the etching condition in the different regions of the samples. In general, we can assume that the etch rate is proportional to the number of silicon atoms removed per hole

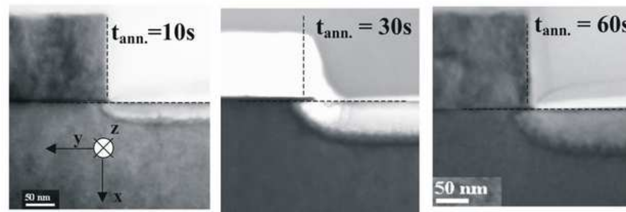

Figure 26: Cross section TEM images of a patterned sample implanted with B $1 \times 10^{15}\mathrm{cm}^{-2}$, 0.25 keV, annealed at 1000°C for (a) 10 s, (b) 30 s and (c) 60 s, after selective etching.

reaching the surface and to the hole flux across the interface. [58,60] The solution-substrate junction behaves as a Schottky contact and so one of the main simulation parameters is the value of the Schottky barrier Φ_B forming at that interface. This value should be considered as a fixed parameter for the Si-electrolyte contact for a given electrolyte composition, and in our case $\Phi_B = 0.1\,\mathrm{V}$, obtained as a fitting parameter. In the case of non-uniform doped substrate, using a reliable approximation in the framework of the Schottky contact theory, the etch rate can be expressed as a function of the local carrier density. [58, 59] However, in the presence of p-n junctions the electric behaviour of the whole system has to be considered, since it can influence the etching results. Therefore, the sample has a Schottky contact on the electrolyte-semiconductor contact and a p+-n- junction in the bulk. The initial surface is flat and the illumination effect is simulated considering a uniform charge generation $qR = 200\,\mathrm{A/cm}^3$ (a typical value for a photoinduced current [60]), where q is the charge and R is the generation/recombination term in the proximity of the surface for a 0.1 mm thickness in depth. The hole-electron pairs generated are separated by the field in the p+-n- junction and the relatively larger hole-flux in the p+ zone causes the selectivity. As a consequence, the simulated etched profile moves faster in the p+ zone.

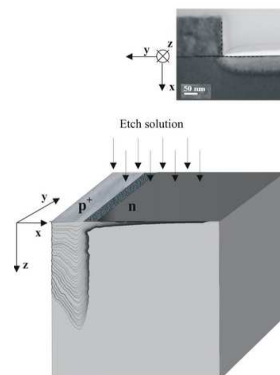

Figure 27: Schematics of the etch process considered in the simulation: the surface in contact with the solution is indicated by the (x, y) plane; the etch process takes place along the x- and the z-direction, where the evolution of the etch profile is simulated as a function of etch time. In the experimental case of a patterned sample (see TEM image in the inset) the third direction (y-axis) must be also considered.

A comparison was performed between the simulated profiles and the etch profiles relative to the experimental images shown in fig. 27. The experimental profiles, that are intensity profiles of the TEM image,

were measured perpendicularly to the surface plane (along the x-axis) from the surface ($x = 0$) towards the bulk. As an example, we show in fig. 28 the excellent agreement between the simulated overall evolution of the etch profile and the experimental etch profile measured in the TEM image, for a sample implanted with B $1 \times 10^{15}\text{cm}^{-2}$ at 0.25 keV and annealed at 1000°C for 60 s. The simulated evolution of the eroded profile is found to stabilize at a vertical etch extension $x = 49\,\text{nm}$, that agrees very well with the experimental value where the etch process stops in the TEM image, indicated by the arrow in fig. 28.

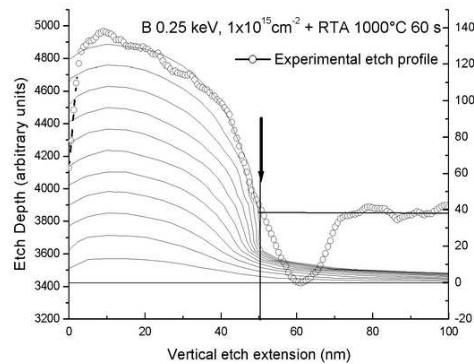

Figure 28: Experimental profile and simulated etch profile evolution relative to the B implant with a dose of $1 \times 10^{15}\text{cm}^{-2}$, at 0.25 keV, after annealing at 1000°C for 60 s.

In fig. 29 we report a summary of all the vertical extensions x of the etched regions obtained experimentally and by simulations for all the investigated B implants (1 keV and 0.25 keV B, $1 \times 10^{15}\text{cm}^{-2}$) after different thermal processes (1000°C for 10 s, 30 s and 60 s). A good agreement is achieved between simulated and experimental values, independently obtained, of the vertical etch extension. Instead, a comparison among the vertical extensions of the etched region in fig. 29 and the active dopant profiles in fig. 24b and fig. 25b shows that, for a given implanted sample with different annealing times, vertical extensions do not correspond exactly to the same doping level. This means that the sensitivity of this experimental technique involving the etch process does not simply depend only on the local dopant concentration, but on the whole dopant profile and the electrical fields generated on the sample.

Coupling a drift-diffusion solver of the electrical problem in the electrolyte-semiconductor system with a simulator of the evolving etch profile is a reliable method to correlate TEM images of selectively etched samples to the dopant profile. Quantitative information on dopant diffusion can hence be potentially extracted from a TEM image of a patterned sample by the inverse calculation, i.e. from the etch profile to the doping profile, with no need of a calibration based on the 1D measurement of the doping level. This is particularly advantageous when the 1D profile cannot be measured by SIMS or SRP because of the absence of special test patterns for such measurements. In principle, information can be extracted also on the lateral diffusion below the mask of a patterned sample, but only if one assumes that the etch contourline is an iso-concentration line. In order to be more rigorous a 3D simulator has to be used, taking into account how the electrical field changes close to the edge of the polysilicon mask.

For further information, please contact V. Privitera, IMM-CNR (vittorio.privitera@imm.cnr.it).

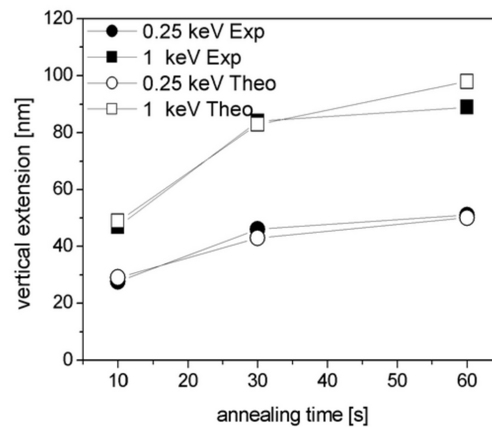

Figure 29: Summary of all the vertical extensions of the etched region obtained experimentally and by simulations for all the B implants investigated (B 1×10^{15}cm^{-2}, 1 keV; B 1×10^{15}cm^{-2}, 0.25 keV) after different thermal processes (1000°C for 10 s, 30 s and 60 s).

3.7 Extraction of the Binding Energy of Boron-Interstitial Clusters from Dedicated Experiments

Work on boron-interstitial clusters in the last seven years resulted in significantly different estimates for their energetic properties. The reason for such discrepancies is certainly that most experimental determinations were based on set-ups in which the redistribution and activation of the implanted boron atoms are used to extract BIC–specific parameters. While such situations are certainly technology-relevant, they do not allow to separate reliably high-concentration diffusion, formation of self-interstitial clusters, the state after ion implantation, and finally the actual formation of BICs. In this work, a set-up suggested first by Solmi et al. [61] is used to separate the effects. It is based on a near-surface generation of self-interstitials by the implantation of silicon (40 keV, $2 \cdot 10^{13}$ cm^{-2}) which induces the formation of BICs in a spatially separated boron-doped layer with a concentration of 10^{19} cm^{-3}. Extraction of energetic parameters is based on a model which comprises a calibrated module for the formation of small self-interstitial clusters and $\{113\}$ defects, a module for the high-concentration diffusion of boron, and a module for the formation of boron-interstitial clusters. In order to find a consistent set of physical parameters, we based our parameter-extraction strategy on a genetic algorithm (GA) developed at Fraunhofer IISB.

Preliminary simulations of our experimental set-up indicated that at low thermal budget, B_2I is the only BIC that clearly influences boron diffusion in the buried structure. On the other hand, simulations also showed that for higher thermal budget, B_2 and B_3I play an important role. It is clear that this conclusion has no general meaning and applies just to our experimental set-up.

Based on our preliminary simulations, the parameter-extraction strategy was divided into two steps. First we extracted the binding energy of B_2I from experimental data obtained at temperatures of 600 and 700 °C for annealing times of 2h and 2 min, respectively. Then, keeping this value fixed, we extracted the binding energies of B_2 and B_3I from SIMS profiles measured after annealing at 740 °C for 45 min and at 800 °C for 1 min.

Figure 30, as an example, shows a comparison between the experimental profiles processed at 600 °C

for 2h and our simulations after optimization of the binding energy of B_2I. The experimental profiles are very well reproduced. The best fit was obtained for a binding energy of -1.85 eV of B_2I^0 with respect to B_s^- and I^+ at mid-gap. This value is in good agreement to the 2.0 eV obtained by Windl et al. [62] within the generalized gradient approximation (GGA). Also indicated in the figures is the effects of varying the binding energy by ±0.2 eV. Varying the binding energies of the other BICs had no significant influence.

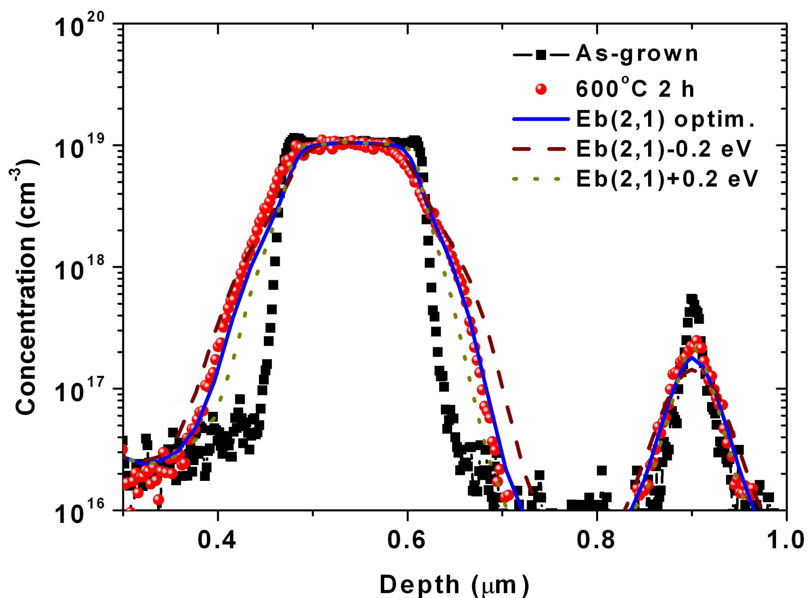

Figure 30: Redistribution of boron during annealing at 600 °C for 2 h

In Figure 31, as an example, the experimental results are shown for the samples annealed at 800 °C for 1 min. Again, the experimental conditions are reproduced very well.

With respect to B_s^- and I^+, the binding energy of $B_2^=$ and B_3I^- were found to be +0.31 eV and -3.0 eV, respectively, at mid-gap. The result for $B_2^=$ confirms that the cluster is instable as unanimously predicted by *ab–initio* calculations. Its binding energy of 0.31 eV obtained within this study is significantly smaller than the GGA value of +0.9 eV calculated by Windl et al. [62]. However, it has to be kept in mind that this value was calculated for a pair of substitutional impurities on next-nearest lattice sites. Farther remote pairs, on the other hand, were shown by Yamauchi et al. [63] and Windl [64] to be more stable. The value of -3.0 eV obtained for the binding energy of B_3I^- is in excellent agreement with the identical GGA value calculated by Windl et al. [62]. Details of the work can be found in [65].

For further information, please contact P. Pichler, Fraunhofer IISB (peter.pichler@iisb.fraunhofer.de).

3.8 Modeling the Formation of Ultra-Shallow Junctions after Non-Amorphizing Boron Implants

One of the main issues of FRENDTECH project is the modeling of boron diffusion in ultra-shallow junctions. In order to predict the redistribution and electrical activation of implanted boron atoms during rapid thermal

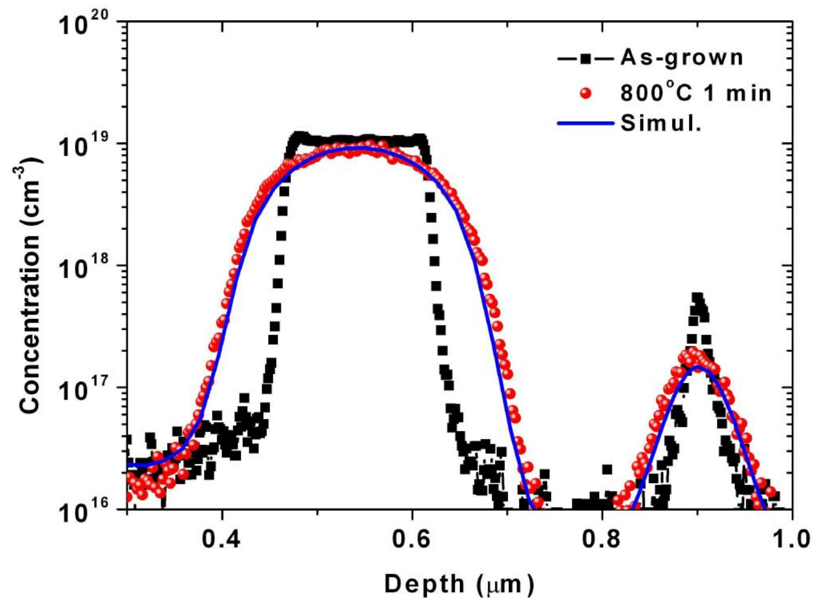

Figure 31: Redistribution of boron during annealing at 800 °C for 1 min

annealing, one must address several phenomena: the diffusion of boron at high concentration, the kick-out mechanism, the agglomeration of the excess interstitials into extrinsic extended defects, the formation of boron-interstitial clusters (BICs) and finally, the recombination of point defects at the surface. Although direct boron implantations are of technological relevance, unfortunately, they do not allow to separate the effects mentioned above. Therefore, during Frendtech, dedicated experimental set-ups were designed to study each effect separately. Each component of the model was then independently validated and calibrated on experimental results. Finally, in order to simulate technology-relevant situations, i.e. the formation of ultra-shallow junctions, the different calibrated components were coupled. In the first case, we simulated the boron redistribution during a soak anneal. Boron was implanted at an energy of 250 eV and for a dose of $1 \cdot 10^{15}$ cm^{-2}. The sample was annealed at 1000 °C for 10 s under an N2 ambient. Experimental results were obtained by IMM. Figure 32 shows a comparison between the SIMS (red dots) and the chemical boron profile obtained by simulation (solid) line. As we can see, the simulation is in good agreement with experimental data. The immobile peak, as well as the tail of the profile are well predicted. In addition, the simulated active profile (open squares) was reported in Figure 32. As expected, the tail of the profile is fully active while only a fraction of the boron atoms contained in the peak are in substitutionnal sites. Indeed, according to the simulation, the immobile peak contains a high concentration of BICs, as expected.

In the second case, boron redistribution during a spike anneal at 1050 °C was studied. Boron was implanted at 500 eV for a dose of $1 \cdot 10^{15}$ cm^{-2} and then annealed following a temperature profile from Mattson. The SIMS profile (red dots) measured after the thermal treatment as well as the corresponding simulation (solid line) are reported in Figure 33 Again, there is a very good agreement between the experimental results and our simulation performed with the full model. As previously, the inactive peak as well as the profile broadening are well reproduced by our model. It is important to note that in our simulations, the physical parameters were kept constant. This demonstrates the validity of our physically-based model but also the

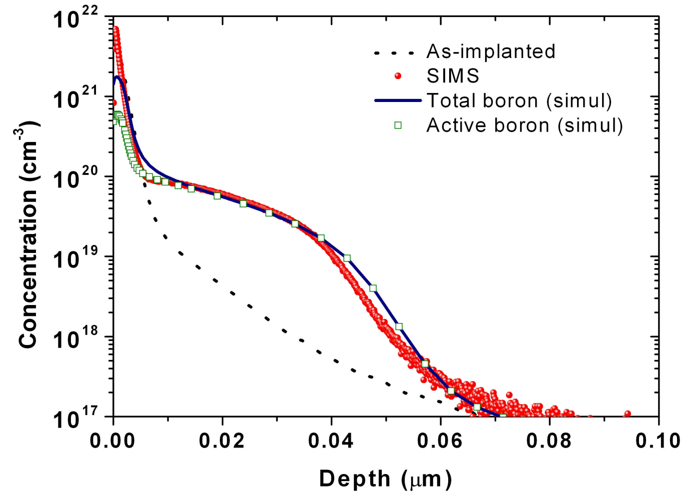

Figure 32: Comparison between simulation and experimental results of a soak annealing for 10 s at 1000 °C after boron implantation with 250 eV and $1 \cdot 10^{15}$ cm^{-2}.

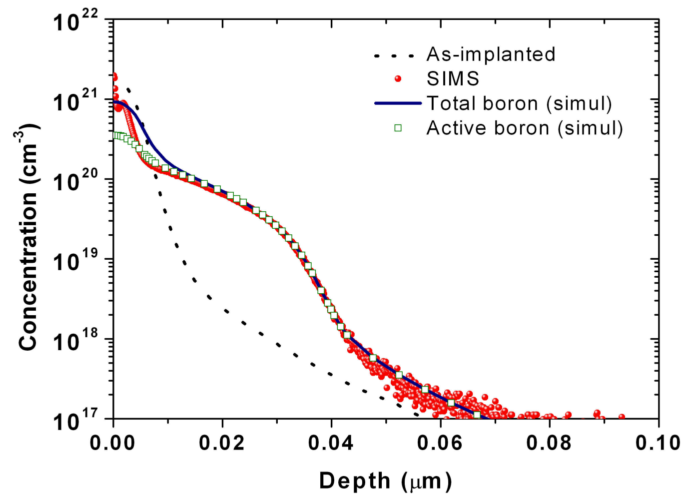

Figure 33: Comparison between simulation and experimental results of a spike annealing at 1050 °C after boron implantation with 250 eV and $1 \cdot 10^{15}$ cm^{-2}.

consistency of the parameters that were extracted independently.

In conclusion, we coupled different simulation modules that were calibrated separately during Frendtech. It is clearly shown that the resulting unified model is able to predict boron redistribution and activation in technology-relevant situations, i.e. for ultra-shallow implants and spike anneals. Details about the work will be published in an invited presentation at the IEDM 2004.

For further information, please contact P. Pichler, Fraunhofer IISB (peter.pichler@iisb.fraunhofer.de).

3.9 Solid Phase Epitaxy - Activation and Deactivation of Boron in Ultra-Shallow Junctions

The Solid Phase Epitaxial Growth (SPEG) technique appears to be a promising method for achieving junction depth and sheet resistance values low enough to meet the performance specifications for the 65 and 45 nm node. However, the dopant electrical activation obtained in this way appears to be metastable and deactivation occurs during a post-annealing step. The availability of reliable experimental data is a necessary condition to allow the validation of predictive models for the simulation of this phenomenon. We have therefore carried out a detailed kinetic study of boron deactivation during thermal processes after SPEG, that includes isothermal anneals at various temperatures, in addition to the typical isochronal studies already available in the literature.

For the experiments, Si wafers were implanted to a dose of $1.0\text{x}10^{15}$ cm^{-2} with $^{11}B+$ (0.5 keV) into a $^{74}Ge^{+}$ preamorphised layer (30 keV $1.0\text{x}10^{15}$ cm^{-2}) where the upper edge of the end-of-range damage (EOR) is at 50 nm. The SPEG process was performed at a temperature of 650°for 5 sec. The regrown wafer was cleaved into 2 x 2 cm2 samples which were subsequently annealed in a Mattson RTP system on a recessed wafer. Post-annealing temperatures ranged from 250°to 1050°, with annealing times ranging from a few seconds up to several hundred seconds. These annealing temperatures were also chosen in order to "'simulate"' typical silicide processes for NiSi or $CoSi_2$ contacts in a standard CMOS process flow.

Figure 34 shows the evolution of the sheet resistance as a function of the post-annealing temperature for a fixed annealing time (30 s). Up to about 750°, the post-annealing step has virtually no effect on the junction activation level. Dopant deactivation is observed at temperatures higher than 750°, with the sheet resistance rapidly increasing from 758 Ω/sq. up to 1300 Ω/sq. in the temperature range 750°-850°. Dopant reactivation is finally observed for temperatures above 900°, with the sheet resistance rapidly decreasing to very low levels.

In order to investigate the deactivation-reactivation process in more detail, isothermal anneals were performed at different temperatures in the critical 750 to 900°temperature range. Figure 35 shows the results obtained at 800°. The two regimes of dopant deactivation and reactivation are observed again at this temperature. For short annealing times (up to 120 s) the sheet resistance rapidly increases almost linearly up to 1500 Ω/sq., about twice the initial value. This is followed by a reactivation regime where the sheet resistance decreases at a much lower rate to about 1100 Ω/sq. for the longest annealing time considered in this study (900 s).

However, dopant diffusion also occurs during the same time interval. It is therefore not possible to establish from sheet resistance measurements only, whether the observed decrease in the resistance values is really related to a dopant reactivation process or simply due to the dopant diffusion during annealing. Using the definition of the sheet resistance and the measured SIMS profiles, it is found that the active dose increases upon annealing from 120 s onwards. This clearly indicates that dopant reactivation does occur already at this temperature. Moreover, for the time interval 300-600 s, it is found that dopant reactivation accounts for more than 70% of the sheet resistance decrease, the remaining 30% being due to dopant diffusion. However,

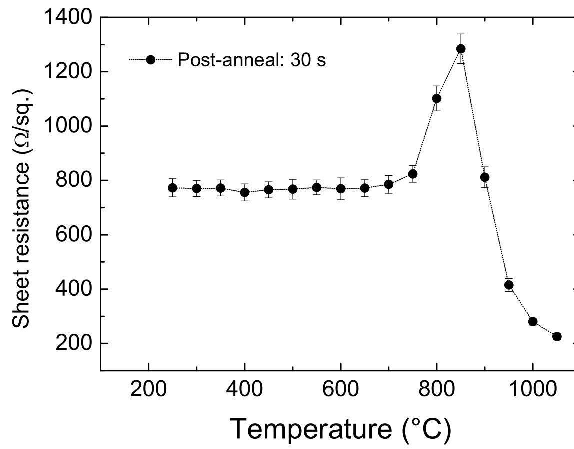

Figure 34: Sheet resistance vs. temperature for SPEG activated junctions (650°5 s) after isochronal post-annealings for 30 s.

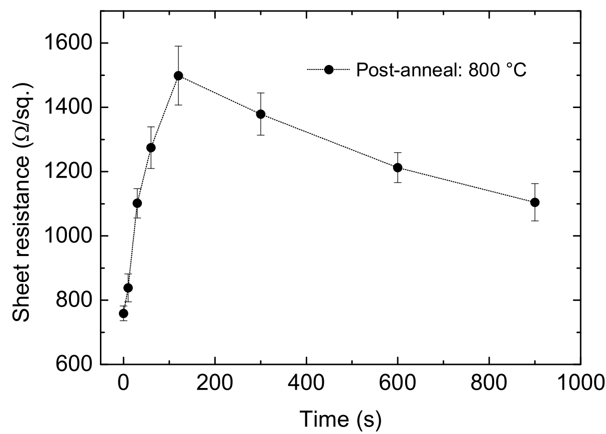

Figure 35: Sheet resistance vs. annealing time for SPEG activated junctions (650°5 s) after isothermal post-annealing at 800°.

it is expected that at higher annealing temperature, dopant diffusion will become the main cause for the sheet resistance decrease upon annealing.

Finally, Figure 36 shows the evolution of the sheet resistance of SPEG activated junctions during isothermal anneals in the temperature range 750-900°. The results indicate that a whole deactivation/re-activation process occurs at all temperatures with kinetics that depend on the temperature.

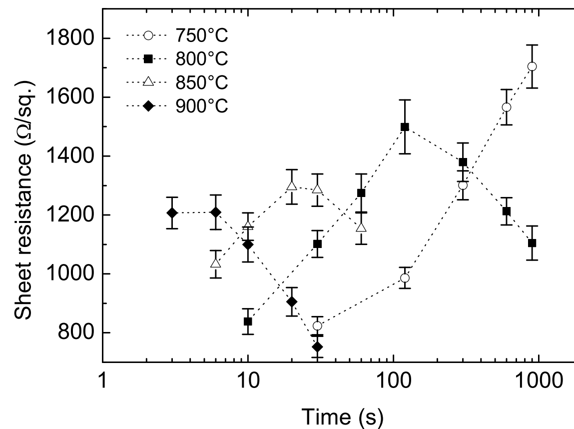

Figure 36: Sheet resistance vs. annealing time for SPEG activated junctions (650°5 s) after isothermal post-annealing for various times.

The observed behaviour therefore appears as the result of a competition between boron clustering (deactivation driven by EOR defect dissolution) vs. cluster dissolution and dopant diffusion (reactivation). In particular, for all the annealing temperatures, it is found that the deactivation mechanism is more efficient at the beginning of the annealing process. In addition, the deactivation and reactivation rates increase with temperature (cf. logarithmic time scale in Fig. 36), indicating that both mechanisms are thermally activated. However, the maximum resistance value (corresponding to the transition from the deactivation to the reactivation regime) decreases with the annealing temperature, suggesting that the reactivation mechanism is characterised by a higher activation energy compared to the deactivation mechanism.

For further information, please contact F. Cristiano, CEMES/LAAS-CNRS (fuccio@laas.fr).

3.10 A Quest for BICs

The activation rate of shallow boron implants can be maximized by optimizing the subsequent annealing, which has to dissolve the boron-interstitial clusters (BIC) formed during implantation. This requires the knowledge of the formation energies of the dominant BICs. Previous theoretical analysis at ab initio level has found a large number of possible complexes and predicted their formation energies with an error bar of about 1 eV. Regarding the number of BICs (15-20) this error introduces uncertainties in kinetic simulations. Therefore, it is desirable to identify the dominant BICs by spectroscopic methods. For that purpose, the measurable properties of all possible BICs have to be calculated a priori with high precision.

Therefore, sophisticated ab initio calculations have been carried out systematically on a large-scale, to establish a data base for the vibration spectra (normal mode frequencies) and electronic structure (one-electron level positions in the gap) for all BICs. After the necessary convergence tests, the silicon crystal, containing the BICs, was simulated by an appropriate supercell model. The total energy and the equilibrium geometry was calculated using density functional theory (DFT) and norm conserving pseudopotentials. The vibration spectra have been determined [66] in the harmonic approximation for all possible isotope composition, using generalized gradient approximation (GGA) and numerical atomic orbitals. The electronic structure was calculated [67] with an optimized hybrid functional and Gaussian orbitals. As a byproduct, some long standing controversies in the interpretation of experimental results on the simplest boron complexes could be solved [68].

Experimental search for characteristic vibrational frequencies

The main task of the vibrational spectroscopy part of the project was to find and identify possible multiboron clusters in B-implanted Si samples. Infrared and Raman spectroscopy is able to provide information on the structure and symmetry of such clusters; the idea was to compare the experimental peak frequencies with theoretical calculations. The main difficulty of this experimental approach is the high number of possible different clusters and their low individual concentration.

Many different types of test samples were produced varying the energy and the dose of implanted B as well as applying different post-implantation annealing. We implanted n-type (100) Si samples with low and high fluence of B (10^{14} - few times 10^{16} cm^{-2}) with energy of 20-90 keV. Multiple energy implantation was applied to create deep uniformly doped regions, a large doped volume in which higher concentration of BICs was expected. The temperature of the post-implantation annealing was varied in order to produce different stable BICs. However no significant characteristic vibrational frequencies were detected on various implanted samples. In order to reduce the background due to the presence of free carriers on the recorded spectra 2 MeV electron beam irradiations were applied with an electron dose of 7-8$\times10^{17}$ cm^{-2}. From this set of experiment we have concluded that electron irradiation alone does not reduce the free carrier concentration significantly. More than 100 different Boron implanted samples were studied by IR and Raman spectroscopy, but no characteristic vibrational frequencies were found.

Ion beam investigation of Boron implanted Si

One of the most important parameter of a shallow junction is the depth distribution (concentration profile) of the dopant species. SIMS method is a widely used tool for exploring shallow B profiles. However SIMS does not provide accurate depth information as it is determined by sputtering processes. An ion beam technique was proposed in the frame of Frendtech project: nuclear reaction analysis (NRA) using the ^{11}B(p,α)^{8}Be reaction at 660 keV proton energies [69, 70]. Nuclear reaction is isotope sensitive, hence only boron can be studied without any disturbing backgrounds of any other elements in the sample, this is the main advantage of the method. The disadvantage of the proposed nuclear reaction is the poor depth resolution what can be achieved. However we combined the NRA experiments with a special sample preparation method: using computer controlled anodic oxidation a very shallow bevelled Si surface can be produce. Boron concentration profile has been determined with high depth resolution from series of NRA measurements on different points of the surface. We demonstrated, that the method is able to follow the redistribution of boron during heat treatments even at the very near surface region of the sample.

N-type (100) Si samples were implanted and annealed with different conditions. From NRA and channeling experiments we can prove that only a part of the Boron atoms sits in substitutional position in the

crystal lattice depending on the applied ion dose and annealing temperature. For example, in case of 20 keV implantation of 1×10^{16} B/cm^2 and annealing at 1100°C, only 55% of Borons is in lattice position, the rest forms mainly interstitial clusters. Performing channeling experiments along different main crystal axes, (100), (110) and (111) we concluded, that boron distributed equally in the crystal, there are no favorable positions or directions for implanted Boron.

For further information, please contact G. Battistig, MTA-MFA (battisti@mfa.kfki.hu).

3.11 Cluster Formation in Ultra–Low Energy High–Dose B^+–Implanted Si

To continue scaling down CMOS devices, ultra–shallow and extremely highly doped p^+/n junctions must be fabricated. As a consequence, boron is implanted at doses that exceed its equilibrium solid solubility limit in silicon. During annealing the boron peak region is therefore found to be immobile and electrical inactive. This is a major roadblock for meeting the ITRS specifications of low sheet resistance in the layers. Previous studies have invoked the formation of either a silicon boride phase like SiB_3 or of Si–B clusters (BICs) made of very few atoms to explain this behavior.

Si wafers were implanted with 0.5 keV B^+ to a dose of 1×10^{15} ions/cm^2 and subsequently annealed at several temperatures in a Mattson 2900 system. SIMS profiles reveal a boron peak concentration of 2×10^{21} cm^{-3} (at a depth of about 2 nm), which is above the solid solubility limit. Boron is therefore expected to easily precipitate. Indeed, an immobile peak is clearly detected after annealing at high temperature (1050 °C), while for lower annealing temperatures (650 °C–750 °C) it is not possible to distinguish any immobile part of the profile (in the peak region) from the mobile one (diffusive tail).

Figure 37a shows a Weak Beam Dark Field (WBDF) plan–view image of a sample annealed at 650 °C. Arrows in the figure indicate the presence of small defect clusters, with diameters ranging from 1 to about 10 nm. Higher temperature annealing results in the disappearance of such defects, indicating that the observed clusters are not the precursors of a stable second phase. In such cases, precipitates are still observed well above 1000 °C. HREM analysis in cross–section samples (Figure 37b) shows that the observed defects are located at a depth of about 2.5 nm below the surface. Figure 38a is an enlarged image of one of these defects while Figure 38b is obtained after Fourier filtering of the experimental image. Such image treatment allows us to identify these defects as being small dislocation loops lying on $\{100\}$ planes and exhibiting an interstitial character (see the extra plane in Figure 38b). Additional experiments show that these defects evolve following an Ostwald ripening mechanism and that they grow when injecting Si atoms during an oxidation step, i. e. they contain Si atoms. However, they cannot be pure Si interstitials defects, as, although small, pure Si defects of such dimensions would contain hundreds of atoms and rearrange in more energetically favorable forms ($\{113\}$s or (111) dislocation loops) easily detectable by TEM. On the other hand, the fact that the defects are formed at the same depth as the peak of Boron concentration, in conjunction with the observation of an immobile B peak even after high temperature annealing, clearly indicates that these defects must contain boron atoms.

The most probable explanation of the results we have obtained is therefore that the $\{100\}$ defects we have observed are boron–Si interstitial complexes i.e., BICs of hundreds of atoms! This might be the first evidence that BICs can be imaged by TEM and thus can be much bigger than generally assumed.

For further information, please contact F. Cristiano, CEMES/LAAS-CNRS (fuccio@laas.fr).

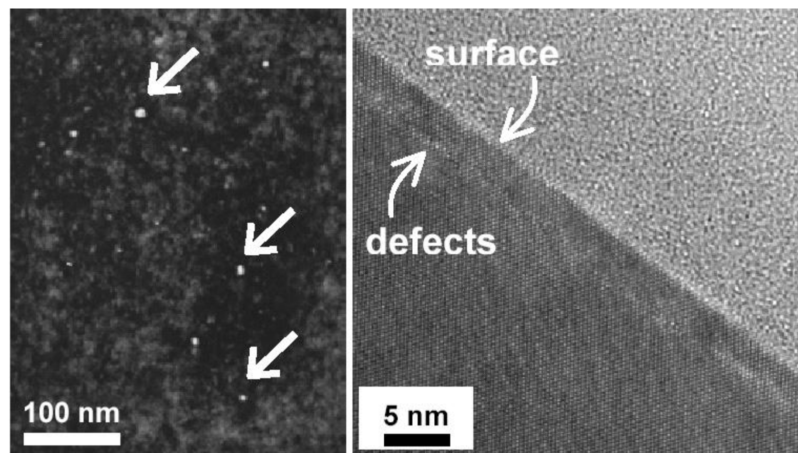

Figure 37: (a) TEM image of a sample annealed at 650 °C. (b) HREM Cross–sectional image showing defects position at 2.5 nm under the surface

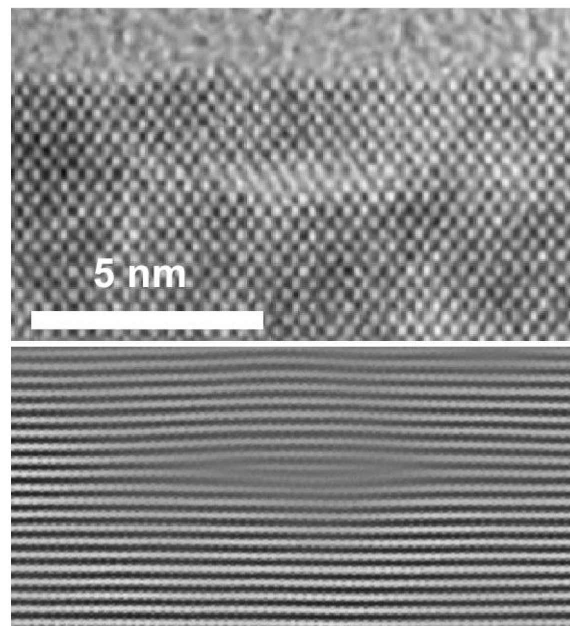

Figure 38: (a) Original HREM image of a defect. (b) Fourier Filtered image obtained using 200 diffracted spots

3.12 Mechanisms of F effect on B Diffusion and Activation

Thermal annealing following preamorphization and solid-phase epitaxy of B implanted ultrashallow junctions leads to unwanted deactivation and diffusion driven by interstitials released from the preamorphization end-of-range defect band. We have shown that F inhibits this process by forming small clusters that act as traps for these back-diffusing interstitials. A competing direct B-F interaction causes deactivation when F and B implant profiles overlap. Both interaction pathways suppress B transient enhanced diffusion.

In future CMOS technology generations, ultrashallow PMOS source-drain (extension) regions will be just a few nanometers thick, and yet will require sheet resistance values well below 1000 Ω/sq. A promising way to achieve this combination is to use preamorphization (PAI) and solid phase epitaxy (SPE) combined with stabilization of B doping by co-implantation of F, C, or other impurities. Stabilizing impurities are a key part of this technology approach, as they prevent B diffusion and deactivation during thermal processing steps following SPE regrowth.

Recently there has been intense interest and controversy over the effect of F on B diffusion during post-regrowth annealing [71] - [72]. In early work within FRENDTECH and the IST ARTEMIS project, B deactivation during post-regrowth annealing of PAI junctions was shown to arise from the interaction between substitutional B atoms and interstitial atoms [73] emitted from PAI end-of-range defects. Excess self interstitials flow down their concentration gradient from the end-of-range (EOR) defect band, where their supersaturation is high as a result of dissociation of interstitials from clusters and 113 defects in the EOR band, to the surface region containing the B profile, where the concentration of interstitials is relatively low as a result of recombination processes. Detailed modeling of the thermal evolution of the EOR band, and of the resulting interactions between the emitted interstitials and B atoms, confirmed this picture quantitatively [74].

At present it is not clear exactly how F intervenes in this process to stabilize B doping profiles against deactivation. It has been proposed that F forms F-V clusters on solid-phase epitaxy, thus providing traps for self interstitials that would otherwise flow towards the surface from the EOR band [75]; F-V clusters have been inferred from positron annihilation experiments [76], and experimental evidence for some form of interstitial trapping mechanism has been collected by Downey et al. and Impellizzeri et al. [71], [72] Other experiments suggest that F forms complexes with B atoms, preventing their diffusion and clustering with other B atoms [77]. It has also been noted that F might increase the stability of EOR defects, thereby reducing the interstitial supersaturation inside the EOR band, and thus the flux of interstitials towards the B profile [72]. An understanding of the actual mechanisms involved, and their relative importance, is essential for the optimization of integrated circuit devices. For example, interstitial trapping and B-F pairing may well have quite different impacts on B electrical activation, leading to very different device optimization strategies.

We have performed a simple but comprehensive experimental study that resolves much of this recent controversy. It clarifies the key importance of the interstitial trapping mechanism for B deactivation control, and shows that direct B-F interactions produce an opposing effect - a degradation in electrical activity. The experiments were performed as follows. Silicon wafers were implanted with 30 keV Ge ions to a dose of 1×10^{15} cm^{-2} and subsequently with 0.5 keV B ions to the same dose. Control wafers were then set aside and the remainder implanted with F ions at 0.9 keV, 10 keV, and 22 keV to doses in the range 3×10^{13} cm^{-2} - 1×10^{15} cm^{-2}, the energies being chosen to place the projected range of the F implant (a) at the depth of the projected range of the B implant, (b) at a depth intermediate between the B implant and the amorphous-crystalline interface created by the Ge implant, and (c) at the depth of the EOR defect band that would subsequently be formed following SPE regrowth. SIMS profiles showing the B implant depth distribution,

the expected location of the EOR defect band, and the three different as-implanted F depth distributions, are shown in Fig. 39.

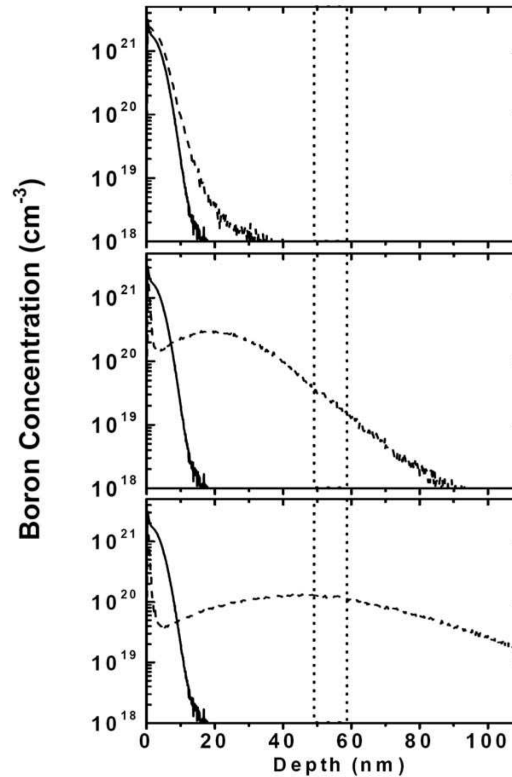

Figure 39: SIMS depth profiles for the 0.5 keV B implant and the 0.9 keV, 10 keV, and 22 keV F implants used in this study, together with the expected depth range of the EOR defect band from the 30 keV Ge PAI implant (indicated by vertical dotted lines). The F implants align (a) with the B implant, (b) with the SPE-regrown region between the B implant and the EOR defect band, (c) with the EOR band.

Following implantation the wafers were cleaved into samples, which were annealed in N_2 ambient at various temperatures ranging from 650-900°using annealing times ranging from 1 sec to 45 min. Samples were subsequently analyzed by four-point probe to determine sheet resistance, R_S, and by secondary ion mass spectrometry (SIMS) to determine atomic profiles of B, Ge and F.

The results show a number of very interesting features of the post-regrowth regime, indicating that F acts on the B dopant through at least two distinct mechanisms, one of which is clearly deleterious for B activation and the other strongly beneficial. To demonstrate this, and identify the likely physical mechanisms involved, we present first SIMS results with and without F co-implantation, and then sheet resistance data showing de-re-activation trends as a function of F co-implant and annealing conditions.

Fig. 40 (a) presents SIMS profiles of a 0.5 keV, 1×10^{15} cm^{-2} B implant, preamorphized by 30 keV

Ge but with no F co-implant, before and after rapid thermal annealing for 1s, 15s, 120s and 2700s at 800°. The profile after 1s is almost identical to that measured immediately after SPE regrowth at 650°(not shown), indicating that extremely rapid diffusion of B has taken place in the amorphous phase, as observed in earlier studies.

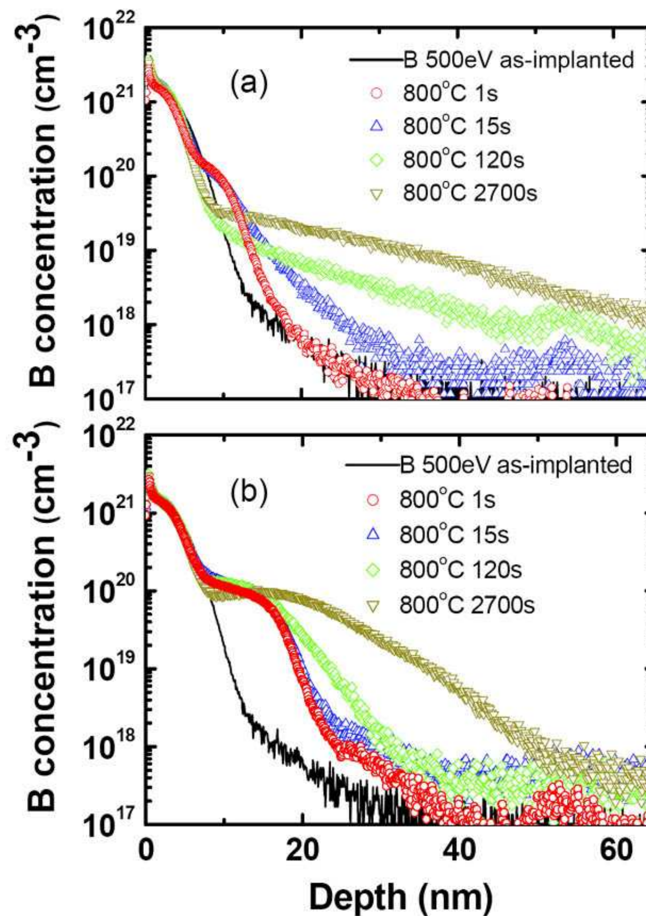

Figure 40: (a) SIMS profiles of a 0.5 keV, 1×10^{15} cm^{-2} B implant, before and after rapid thermal annealing for 2s, 15s, 120s and 2700s at 800°. The profiles exhibit a static peak, 'kink' and fast-diffusing tail, the kink concentration decreasing by an order of magnitude from $\sim 2 \times 10^{20}$ cm^{-3} after 2s to $\sim 2 \times 10^{19}$ cm^{-3} after 120s, followed by an slow increase towards longer times. (b) Corresponding results in the case where F has been co-implanted at an energy of 10 keV and dose of 1×10^{15} cm^{-2}. In this case the diffusion is close to normal values (see text) and the reduction in kink concentration does not occur.

Each of the annealed profiles in Fig. 40 (a) exhibits a static peak, kink and fast-diffusing tail, the kink concentration decreasing by an order of magnitude from $\sim 2\times10^{20}$ cm^{-3} after 1s to $\sim 2\times10^{19}$ cm^{-3} after 120s, followed by an slower increase in the time range from 120s to 2700s. This kink is a well known feature, corresponding to the concentration level above which B forms immobile clusters and is thus unable to diffuse. The initial kink level present at 1s reflects B clustering that has occurred in the amorphous phase prior to regrowth, and the decrease in kink concentration seen at times from 15s to 120s is the expected consequence of interstitial-driven B clustering in the regrown crystalline phase, arising as interstitials flow towards the B profile from the Ge EOR defect band.

Fig. 40 (b) shows corresponding results in the case where F has been co-implanted at an energy of 10 keV to a dose of 1×10^{15} cm^{-2}. The impact of F on B diffusion in the amorphous phase prior to regrowth is to increase the profile broadening after 1s relative to that in Fig. 40 (a). Such increased broadening has been observed in previous studies - it was first attributed to an effect of F on B diffusion in amorphous silicon [78], and later to the role of F in slowing the SPE regrowth rate [79].

Concerning the behavior of B in the recrystallized silicon at times after 1s, the B SIMS profiles in Fig. 40 (b) show no significant decrease in the kink concentration level, indicating that some mechanism is preventing the interstitial-driven deactivation process. Since the F has been implanted well beyond the depth range of the B implant, the F concentration in the B peak region is too low to allow significant trapping of B into B-F complexes. We therefore propose that the 10 keV F implant has suppressed B deactivation by preventing the arrival of interstitials at the location of the B profile, thus suppressing deactivation. Another noticeable feature of Fig. 40 is the rate of B diffusion after the 10 keV F implant, which is much lower than in the case without F. This is again consistent with a reduction in the EOR-driven interstitial supersaturation, due to interactions with an as-yet unknown defect species created by the F implant. Quantitative analysis reveals that the F co-implantation has brought down the interstitial concentration in the B region to near-equilibrium values.

Fig. 41 presents sheet resistance data showing B deactivation during annealing at 800°following high-dose (1×10^{15} cm^{-2}) F implantation at energies chosen (as in Fig. 39) to place the maximum F concentration at the depth of (a) the B implant, (b) the gap between the B implant and the EOR band, (c) the EOR band itself. There are several key features to these results.

In the control case without F implantation, R_S rises to a peak value of 1580 Ω/sq. and then falls at longer annealing times. This behavior is expected from earlier work [73], [74], [80] and can be understood in terms of interstitial trapping to form B-I clusters, followed by reactivation of the clusters and diffusion of B, as we also saw in Fig. 40(a).

The addition of a F implant at 0.9 keV causes a deleterious increase in R_S at short annealing times, suggesting that B interacts directly with F to produce complexes with a lower level of electrical activity than the substitutional B atoms from which they are formed. On further annealing the situation reverses as the value of R_S with the 0.9 keV F implant falls below that found in the control case.

The addition of a 10 keV F implant has no deleterious impact at short times, and almost completely suppresses the deactivation observed in the control case. A slight increase in R_S is observed, peaking at a somewhat shorter anneal time than in the case of the 0.9 keV F implant. Since the 10 keV F implant has almost no overlap with the B implant profile, the improvement in activation at short times must be due to the absence of the direct reactions between B and F that occurred in the 0.9 keV case. Since the 10 keV implant also has relatively little overlap with the EOR band, it is unlikely that the suppression of deactivation in this case is related to a change in stability of the EOR band. We propose that deactivation is suppressed by trapping of interstitials as they flow from the EOR band towards the surface.

Interstitial trapping also accounts for the observed cross-over between the 0.9 keV R_S curve and the control curve at longer annealing times, as the initial deactivation caused by the direct B-F interaction is

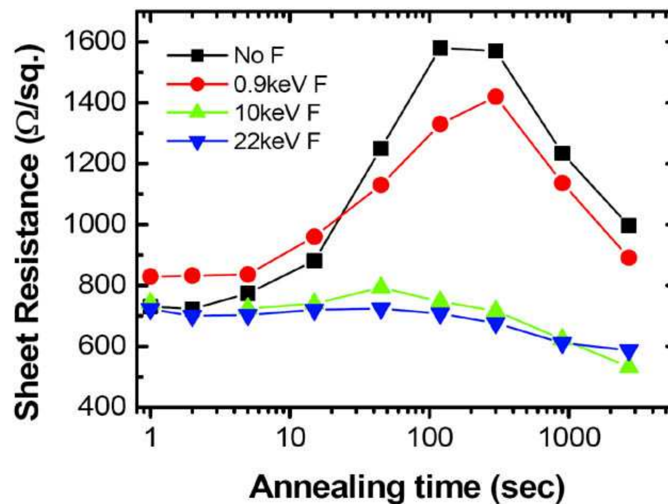

Figure 41: Sheet resistance values for a 0.5 keV B implant after annealing at 800°(a) without F co-implant, (b-d) with 0.9 keV, 10 keV and 21.5 keV F co-implants to a dose of 1×10^{15} cm^{-2}. The 0.9 keV co-implant gives a higher initial sheet resistance, and gives relatively weak protection against deactivation at longer times. The 10 keV and 21.5 keV co-implants leave the initial sheet resistance unimpaired and provide excellent protection against deactivation.

compensated by a reduction in deactivation due to interstitial trapping by the 0.9 keV F implant. In this case there is no overlap whatever between the F implant and the EOR band, thus confirming the dominant role of the interstitial trapping mechanism.

The result of implanting F at 22 keV is very similar to that obtained at 10 keV, and can be attributed to the same mechanism. Data at the lower F dose of 3×10^{14} cm^{-2} (not shown), which still show a clear deactivation peak, show that the deactivation timescale has increased by about 40%, possibly consistent with a small increase in EOR defect stability. However, such an increase could not account for the large reduction in deactivation which we observe. The slightly lower peak R_S values obtained with the 22 keV F implant may arise from the increased separation between the B and F profiles, which minimizes direct B-F interactions in the deeper parts of the diffused B profiles, as well as from an increase in EOR defect stability.

In summary, we have shown that by placing implanted F atoms at depths intermediate between a shallow B implant and a deeper preamorphization end-of-range defect band, one can stabilize the B against deactivation by self interstitials, whilst minimizing deactivation caused by B-F complex formation. The stabilization arises predominantly from the trapping of interstitials at small F-related defects whose structure is as yet unknown, but which may well be F-V clusters. Our results, using ion-implanted B, Ge and F under commercial implantation conditions, are readily applicable to the design and fabrication of advanced high-performance CMOS source-drain structures. Furthermore, our results give a valuable baseline for the modeling of the fluorine effect on dopant diffusion and activation.

For further information, please contact N. E. B. Cowern, Univ. Surrey (Nick.Cowern@surrey.ac.uk).

4 Diffusion in SiGe and Strain Effects

4.1 Implantation and Diffusion of Boron in Germanium

We report the follow up experiments on boron implantation in germanium. Boron was implanted in germanium at 20 keV with 6×10^{14} /cm^2 fluence. As reported in a previous FRENDTECH bulletin a long implantation tail was seen in as-implanted profile. Motivated by the lack of information about boron implantation in germanium, subsequent experiments were carried out to resolve the cause of implantation tail. To this end, crystalline germanium target was pre-amorphised by ^{72}Ge implantation at 400 keV to a fluence of 2×10^{15}/cm^2. Fig. 42 provides the boron concentration profiles for implantation in crystalline and amorphised germanium. The theoretical profile calculated by SRIM on the basis of the assumption of implantation in amorphous target matches the experimental profile for implantation in amorphised germanium. This provides a clear evidence that boron concentration profile for implantation in crystalline germanium is strongly affected by channelling phenomenon. Boron diffusion in Ge following implantation or deposition

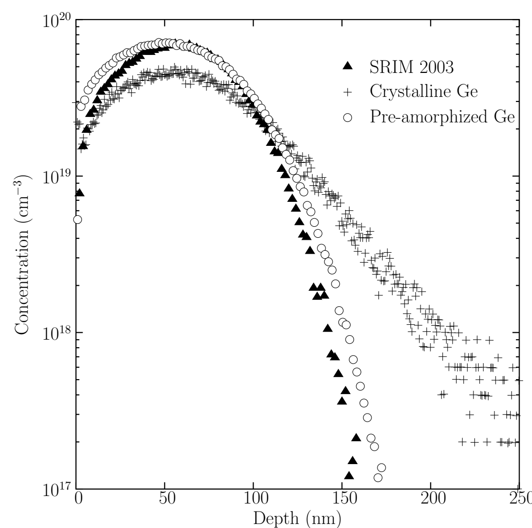

Figure 42: Comparison of boron implantation profile in crystalline and pre-amorphised germanium.

of delta doped MBE grown epitaxial Ge:B layers has been studied with low energy SIMS. Remarkably slow diffusion of B in Ge is observed which corresponds to diffusivities about two orders of magnitude smaller than the lowest values previously estimated in literature. We observe an immobile peak in the annealed profiles which is attributed to concentrations being above the solid solubility limit shown in Fig. 43. Similar values measured for diffusivities in the B implanted layer and epitaxially grown material suggest that the effect of implantation damage on the measured diffusion is negligible. An activation energy of 4.65 ± 0.3 eV is assigned for B diffusion in Ge within the temperature range 800–900 °C from the values presented in Fig. 44. Our results cast doubt on the prevailing picture of vacancy dominated diffusion of B in Ge and suggest that interstitial mediated mechanism should be considered. This experimental conclusion is in agreement with very recent theoretical calculations.

For further information, please contact A. F. Willouhby, Univ. Southampton (A.F.Willoughby@soton.ac.uk).

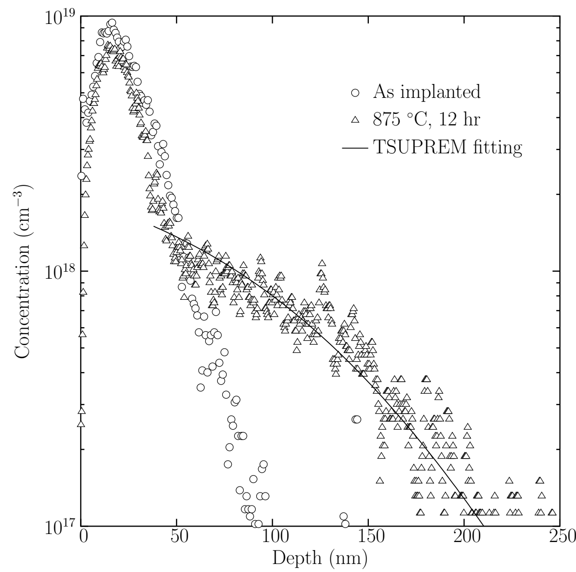

Figure 43: As-implanted and annealed profiles of boron implanted with 5 keV and $3\times10^{13}\,cm^{-2}$ fluence. Diffusion analysis is performed using TSUPREM.

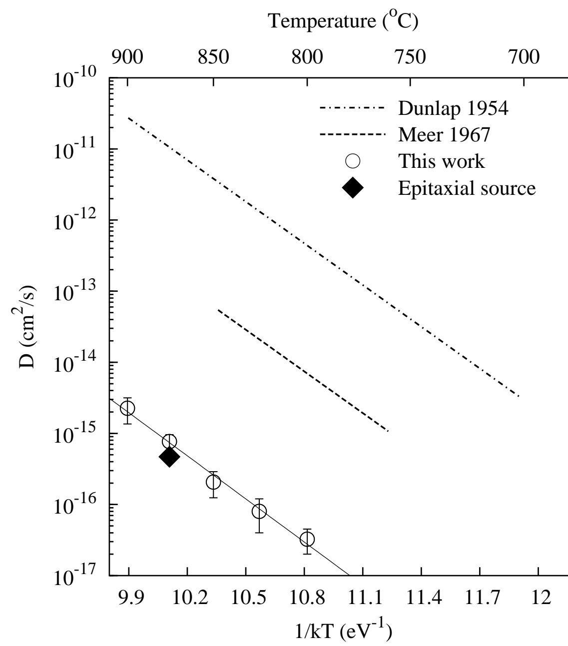

Figure 44: Arrhenius curve for B diffusion in Ge from our study (points) in comparison to literature data [81, 82].

4.2 Effects of Defect Injection on Sb Diffusion in Si and SiGe

Defect injection effects on Sb diffusion has been measured in 10% SiGe by rapid thermal annealing (RTA) in oxygen. Interstitial and vacancy injection were achieved by annealing bare and Si_3N_4 covered sections, respectively. Inert (non-injection) areas were created by depositing a silicon nitride layer over a pre-deposited low temperature oxide (LTO) layer. Diffused profiles show that vacancy injection enhances the diffusion of Sb while interstitial injection retard it, see Fig. 45. Comparison of injection effects in SiGe and Si reveals that there are weaker retardation and enhancement effects in SiGe than in Si, suggesting $f_{\nu(\mathrm{SiGe})} < f_{\nu(\mathrm{Si})}$. It is possible to conclude at this point that Sb diffusion in SiGe is dominated by a vacancy mediated mechanism.

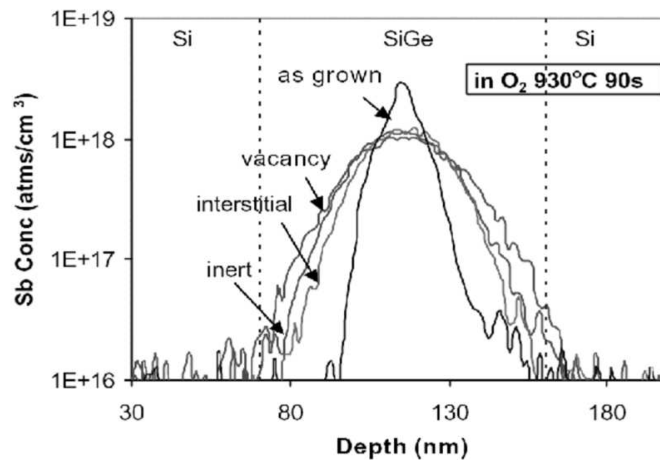

Figure 45: As-grown and annealed profiles for Sb in SiGe. The annealing was performed at 930°C for 90s under inert, interstitial-injection and vacancy-injection conditions.

For further information, please contact A. F. Willouhby, Univ. Southampton (A.F.Willoughby@soton.ac.uk).

4.3 Effects of Defect Injection on As Diffusion in Si and SiGe

We have utilized buried marker layer structures in conjunction with RTA processing to provide direct evidence for a dual vacancy-interstitial mechanism for As diffusion in Si as well as in relaxed $Si_{0.9}Ge_{0.1}$ layers at 1000 °C. An enhancement of As intrinsic diffusivity in $Si_{0.9}Ge_{0.1}$ compared to Si only due to the Ge chemical effect has also been quantified. Qualitatively, a higher contribution of vacancies for As diffusion in Si-Ge as compared to in Si is apparent from Fig. 46.

For further information, please contact A. F. Willouhby, Univ. Southampton (A.F.Willoughby@soton.ac.uk).

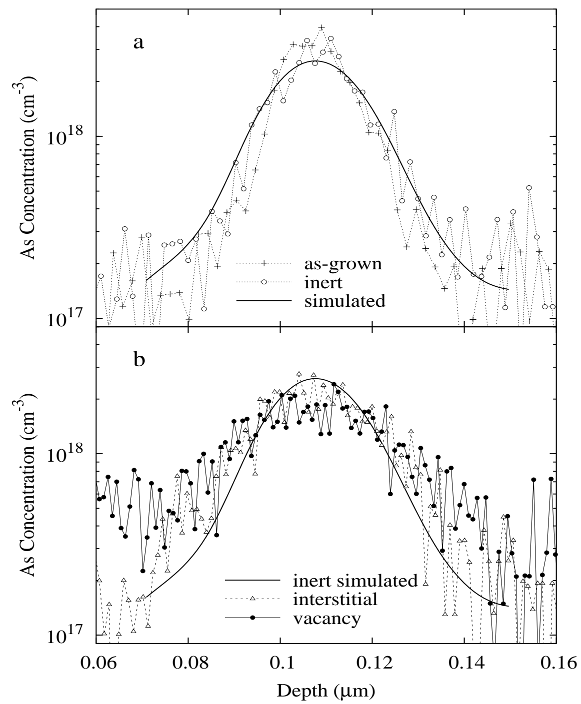

Figure 46: Arsenic concentration profiles in relaxed $Si_{0.9}Ge_{0.1}$: (a) as-grown and inert annealed (b) annealed under defect injection conditions at 1000 °C for 30 s. The solid line in both (a) and (b) represents the best fit to the inert annealed profile.

5 Oxidation

5.1 On the Dry Oxidation Kinetics of Ultra-Thin Oxide

Introduction

The modeling of growth kinetics of ultrathin oxide films is of crucial interest since the next technology nodes require oxide composed of a few atomic planes. To date, the seminal work of Deal & Grove model remains the main approach used in process simulators to describe the oxide growth, even the limitation of this model to describe the initial growth regime ($t_{oxide} \leq 30$ nm) for dry oxidation or the difficulties to extend it to various oxynitration process. Much research work has been dedicated to elucidate the breakdown of the Deal & Grove model in the ultrathin regime but they have not been unanimously accepted. A revision of the Deal & Grove model is clearly necessary to give: (i) a fundamental and quantitative understanding of the interaction between oxygen, nitrogen and silicon at the Si/SiO_2 (ii) the fraction of oxidation taking place strictly at the interface and in the reacting region (iii) the amount of suboxides and interstitials in function of the interface distance and eventually (iv) the amount of nitrogen incorporated during an oxynitridation (NO, N_2O gas).

Reaction rate approach

We developed a new approach assuming that the oxidation process remains basically a diffusion reaction system. The main diffusing species is molecular oxygen O_2 (the oxygen concentration is defined by n_{O_2}) which diffuses in the silicon dioxide and reacts at the interface. The two other species are pure silicon Si (n_{Si}) and silicon dioxide SiO_2 (n_{SiO_2}) created during the oxidation process in the region of reaction. In this model, the oxide thickness is not calculated but is rather a consequence of the evolution of the different species. Two other main differences with the Deal & Grove model are postulated. We do not consider the stationnarity assumption which means that the evolution of the different species (n_{O_2}, n_{Si} and n_{SiO_2}) is time dependent and calculated at each step. Futhermore, the region of reaction is not restricted to the interface and is defined by the overlap between silicon and oxygen. The mathematical formulation of the three steps (diffusion of O_2, reaction with silicon, and creation of silicon dioxide) leads to a system of three equations:

$$\begin{cases} \dfrac{\partial n_{O_2}}{\partial t} = \nabla(D \cdot \nabla n_{O_2}) \quad -k \cdot n_{O_2} \cdot n_{Si} \\ \dfrac{\partial n_{Si}}{\partial t} = -k \cdot n_{O_2} \cdot n_{Si} \\ \dfrac{\partial n_{SiO_2}}{\partial t} = k \cdot n_{O_2} \cdot n_{Si} \end{cases} \tag{4}$$

where k is the reaction rate between the molecular oxygen and silicon and D is the diffusivity of molecular oxygen in the region of reaction.

Test and validation in the ultra-thin regime

We compare here our results with the kinetics of Massoud at atmospheric pressure from 800°C to 1000°C (Figure 47). Thanks to the calibration, we have an excellent agreement between the experimental data and

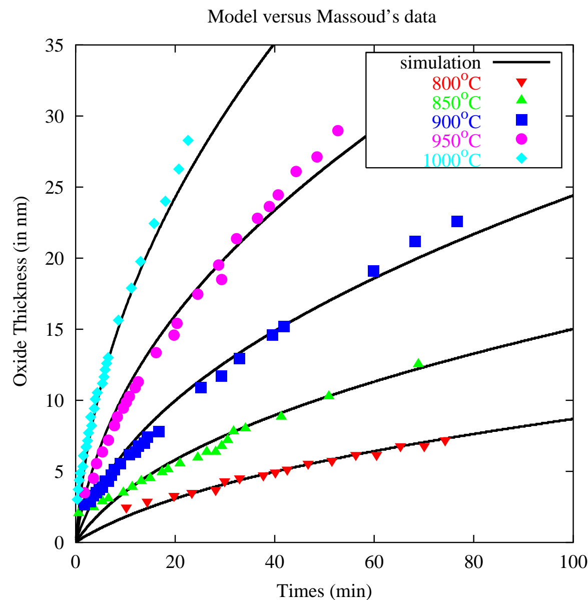

Figure 47: Comparison between the experimental kinetics of MASSOUD for dry oxidation and the kinetics predicted by the new approach.

the model. By adding some additional terms in the growth rate law of Deal& Grove, Massoud succeeds in describing their own experimental kinetics. However no physical reason was given to these aditionnal terms. We succeed in simulating the initial regime where the oxidation is reaction limited with a more strict interpretation of the oxidation process.

In order to test further the model, several experiments mostly at low temperature (725°C, 750°C, 800°C) have been performed to fabricate oxide in the [1.5-5nm] range (Figure 48). Our experiments were performed on (100) silicon substrates (p type doped 5×10^{15} at/cm^3) that previously received a RCA cleaning and 1% HF dip. The oxide growth was carried out in a standard furnace. The oxide thickness has been measured by ellipsometry and validated by TEM measurements (Figure 49). Particular attention has been paid to evaluate the oxide thickness at the end of the initial temperature ramp. The simulation of these different kinetics are reported in the same figure. Since we do not simulate the initial temperature ramp, we shift the theoritical kinetics to reach the experimental thickness at the end of the ramp. An overall good agreement between the experiment and the new approach has been obtained. Furthermore, the simulation with the classical models (Deal&Grove and Massoud) leads to very flat kinetics where almost no oxide growth is observed for the two lowest temperatures (725°C, 750°C) (Fig. 49, 50). The standard approaches are clearly not adapted to this thickness range in contradiction with the new model.

Conclusion

In conclusion, we propose a new approach to describe the dry oxidation in the ultra-thin regime. The new model has been calibrated and we compare with many oxidation kinetics of the literature. Futhermore several experiments have been carried out to confirm the ability of the model to describe the oxidation kinetics in the

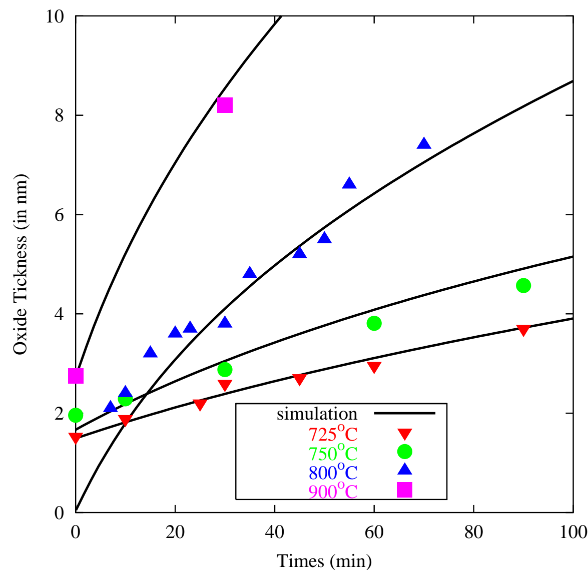

Figure 48: Comparison between the experimental kinetics made at IEMN and the kinetics predicted by the new approach. The experimental kinetics at 800°C is specific since no oxygen is present during the initial temperature ramp and for the simulation a surface free of oxide has been assumed.

[1.5-5 nm] range. These results are very promising for the application to the various oxynitridation processes (NO, N_2O).

For further information, please contact C. Krzeminski, ISEN/IEMN (christophe.krzeminski@isen.iemn.univ-lille1.fr).

5.2 On the Simulation of Oxynitridation Process

Introduction

Silicon oxynitrides are now introduced in production for the 120 and 90 nm technology nodes in order to replace silicon dioxide in the gates of metal oxide semiconductor device. According to the ITRS Roadmap, oxynitrides are assumed to be the dielectric gate material up to the 45 nm technology nodes [83]. The equivalent oxide gate thickness is actual less than 3 nm and is expected to fall down to 0.8 nm in 2009. To date, no manufacturing solution with high-κ dielectric has been identified [84]. High-κ have generally a very poor thermal stability and poor interface characteristics. Moreover, a layer of 0.4 nm silicon oxynitride could still be required in the future as an interface between the channel and the high-κ in order to preserve the channel mobility and the interface characteristics.

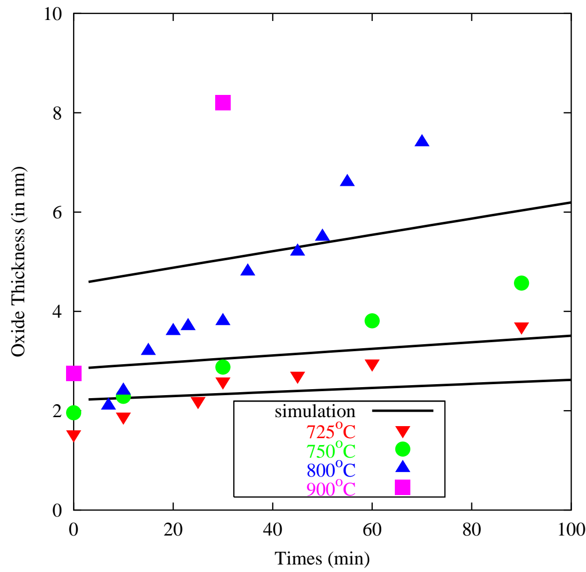

Figure 49: Comparison between the experimental kinetics made at IEMN and the kinetics predicted by Deal and Grove model.

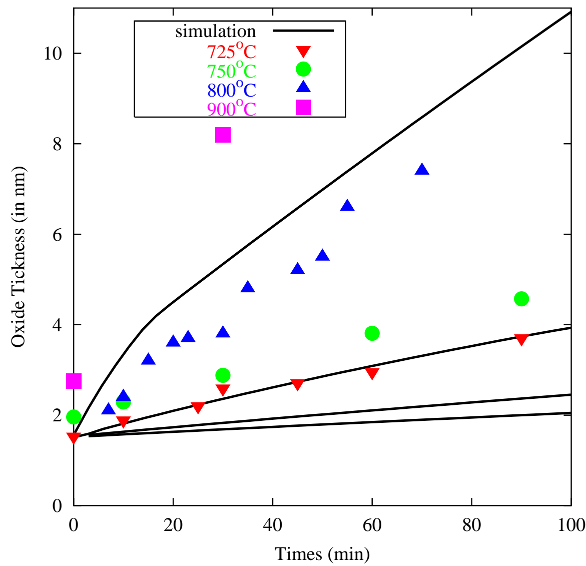

Figure 50: Comparison between the experimental kinetics made at IEMN and the kinetics predicted by Massoud model. Only for the highest temperature (900°C), the variations predicted by the Massoud's model are in agreement with the experiments.

Figure 51: TEM cross section of a 1.9nm oxide resulting of 10 minutes of dry oxidation at 725°C.

Scaling challenges for oxynitrides

The incorporation of nitrogen into the oxide provide several advantages such as the reduction of electrically active defects or traps, improved breakdown properties and reliability. Moreover the presence of nitrogen tends to suppress the diffusion of boron in pMOS . Several methods have been reported in order to form oxynitride : (i) ammonium nitridation (NH_3) and reoxidation , (ii) nitrous oxide (N_2O) oxidation, (iii) nitric oxide (NO) oxidation. The commun drawback of these processes is that the nitrogen peak position is generally located at the silicon/oxide interface, no matter the ambient used. In fact, the ideal nitrogen profile should have a very high nitrogen concentration close to the oxide/poly-Si interface and a few amount of nitrogen at the oxide silicon interface. Several studies suggest the engineering of the nitrogen profile using multisteps oxidation with different ambients. This approach is valid for the 90 nm technlogy nodes. However it has been shown, recently, that NO oxynitride gate oxide does not meet the requirement for the suppression of boron penetration for less than 1.0 nm. Several process have been developped for the next technlogy nodes to form oxynitrides with a low thermal bugdet. Plasma Nitridation PN (RPN or DPN) is the probable candidate since PN has been qualified for the 65 nm technology node [85, 86].

Impact on process simulation?

As shown by the last section, the innovation in process technology in order to improve the properties of the oxynitrides and to keep pace with Moore's law is considerable. The contrast with process modeling is astonishing. At the best, with a good commercial process simulator, you will be able to simulate accurately the oxide growth of a thick oxide by wet oxidation with a stress dependent DEAL and GROVE model. Mostly the simulation of oxide growth reduces to simulate the two dimensional shape of isolation structures (LOCOS, SILO, STI..). The problem of TCAD: "yesterday's technology modeled tomorrow" suggested by LAW is particularly relevant here [87]. On the other side, the experimental optimisation of oxynitride face several physical problems (NBTI, channel mobility reduction, decrease gate leakage current) and qualitative simulations of these effects could be interesting.

As shown by the following figure 52, the tendency is to increase the nitrogen incoporated in the oxide in order to reduce the gate leakage current. However it has been observed, that a very high amount of nitrogen incoporated at the silicon interface leads to an important Negative Bias Temperature Instability (NBTI) in p-channel MOSFETs [88]. The NBTI effect has a strong importance on design issues and circuit reliability [89, 90]. More understanding is needed in order to optimise the nitrogen distribution to reduce the NBTI effects. A recent study [92] stress the influence on the leakage current of the structure of the stack layer (SiON/Si or SiON/SiO_2/Si) and the influence of the [O] concentration in the oxynitride film. The study shows that the optimum concentration [O] is around 40 % in order to minimise the gate leakage current (see Fig. 53). These effects complicate the downscaling and the development of next technology nodes. A physical model able to simulate the nitrogen profile could be be very interesting in order to validate the profile generated experimentaly andto help the device simulation to introduce in their model the influence of nitrogen on the channel mobility and on the reduction of the leakage current.

Reaction rate approach for the simulation of N_2O oxynitridation

The main objective in Frendtech is to improve the situation and to provide physical models in the case of nitrogen compounds. We focus the work on the modelisation of N_2O oxynitridation. This process is much more complex to modelise than the classical (wet or dry) oxidation step. As shown in the figure 54, several mechanisms (gas phase decomposition, oxidation with molecular oxygen and oxidation, nitridation (with

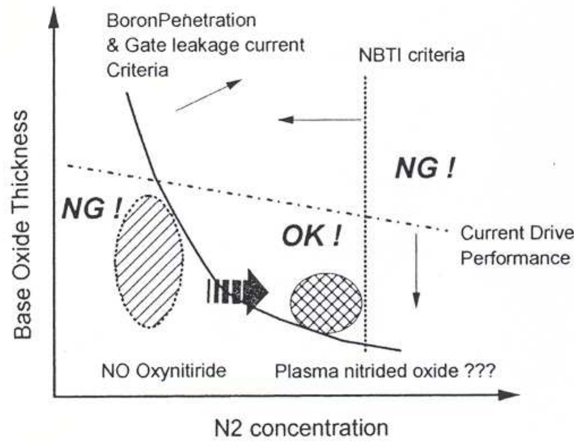

Figure 52: Scheme describing the compromise (of the nitrogen concentration) necessary in order to limit NBTI effect and to decrease the gate leakage current with decreasing oxide thickness (from Toshiba [91]).

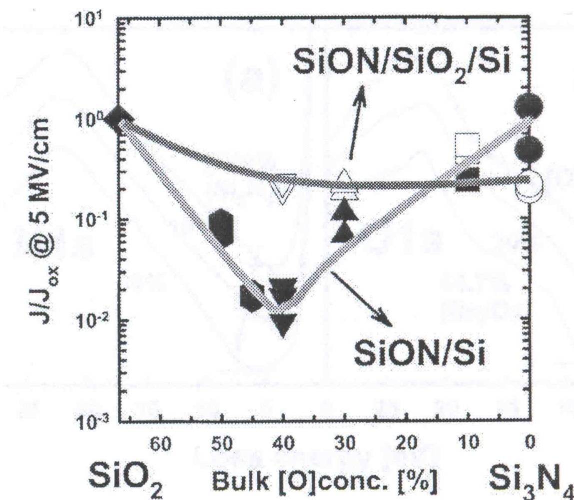

Figure 53: Device simulation study from MURAOKA [92] *et al*. showing the decrease of the relative gate leakage current (J/J_0) with decreasing [O] concentration in the oxynitride. However, the effect is strongly dependent of the structure of the oxide stack. The optimum is obtained for 40 % of oxygen concentration and for a SiON/Si structure.

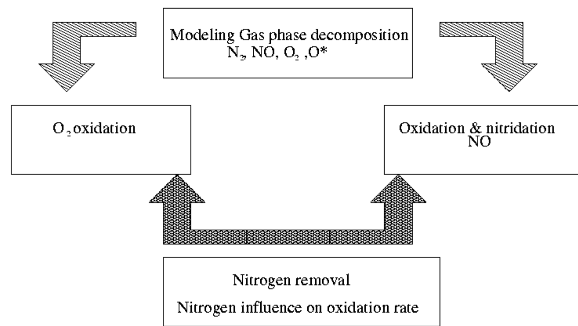

Figure 54: Schematics of the strategy defined to simulate the N_2O oxynitridation step. The various steps and the interaction between the different mechanisms are reported.

NO)) have to be simulated and are still under debate. Furthermore, two parallel reaction mechanisms take place in silicon and interact with each other. The problem has been solved with a two-step scheme. The first step corresponds to the modeling of the gas phase decomposition. The second one tackles the reaction of the decomposition products with silicon.

a) Gas Phase Decomposition

The first part of the work concerns the modeling of the gas phase decomposition. The gas phase concentration of the various species is known to strongly influence the kinetics of oxidation and the nitrogen profile. We follow the approach of ELLIS and BUHRMAN [93] to simulate the gas phase decomposition with a eight reactions scheme:

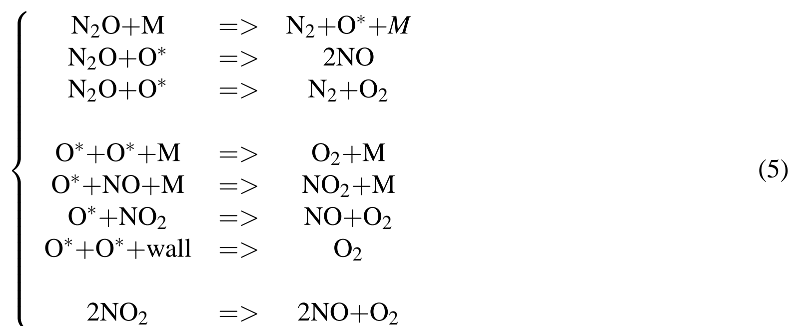

$$\left\{ \begin{array}{ccc} N_2O+M & => & N_2+O^*+M \\ N_2O+O^* & => & 2NO \\ N_2O+O^* & => & N_2+O_2 \\ & & \\ O^*+O^*+M & => & O_2+M \\ O^*+NO+M & => & NO_2+M \\ O^*+NO_2 & => & NO+O_2 \\ O^*+O^*+wall & => & O_2 \\ & & \\ 2NO_2 & => & 2NO+O_2 \end{array} \right. \quad (5)$$

N_2O decomposes in several species (N_2, O_2, NO_2, O^*) with collision partners (denoted by M in the reaction scheme). Figure 55 shows some results of the modeling of the gas decomposition. Only three species remain at the end of the decomposition. The ambient contains almost molecular nitrogen N_2 and molecular oxygen. The amount of NO generated is very small (less than 4%) and increases with the temperature. Finally, we stress that the ambient is mainly composed of molecular oxygen, and the approach described in the first section remains valid if the influence of nitrogen on the reaction rate is incorporated. The simulation of the nitrogen profile requires the modeling of the interaction between NO and silicon.

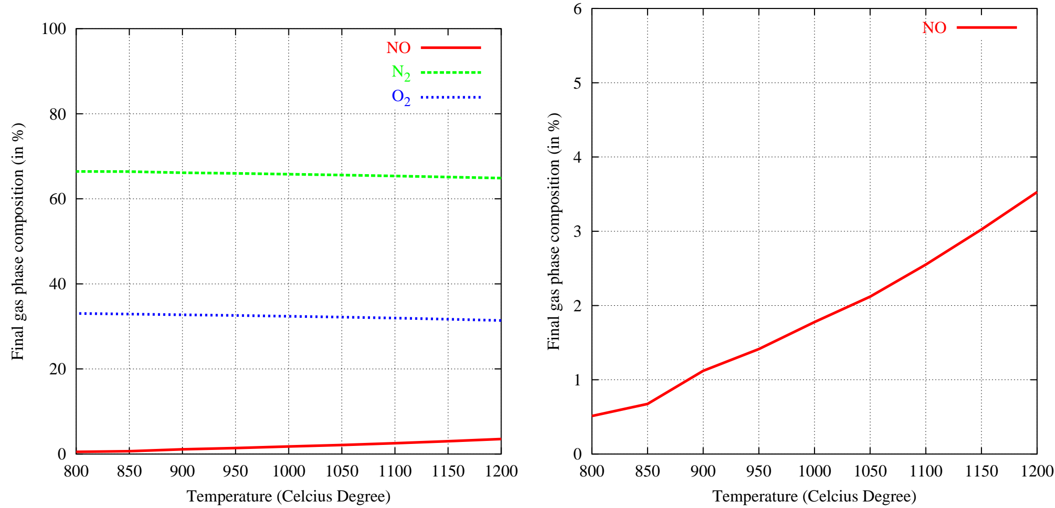

Figure 55: The evolution of concentration of the three species resulting form decomposition (N_2O, O_2, NO) in function of the furnace temperature is reported. On the right, a focus is performed on the evolution of the NO molecule with increasing temperature.

b) Compact Modeling of N_2O Oxynitridation

For the case of the N_2O oxynitridation, we develop a compact model. We use the fact that the final ambient is mostly composed by molecular oxygen and that N_2 is inert for standard temperature processing. The nitrogen compound in the ambient has been estimated to be less than 4% in our simulation of the gas phase. The associated reactions with the NO species can be neglected in order to build-up a compact model. The main diffusing species is molecular oxygen O_2 (the oxygen concentration is defined by n_{O_2}) which diffuses in the silicon dioxide and reacts at the interface. The two other species are pure silicon Si (n_{Si}) and silicon dioxide SiO_2 (n_{SiO_2}) created during the oxidation process in the region of reaction. The mathematical formulation leads to the following system of equations:

$$\left\{ \begin{array}{rcll} \frac{\partial n_{O_2}}{\partial t} &=& \nabla(D \cdot \nabla n_{O_2}) & -k(N) \cdot n_{O_2} \cdot n_{Si} \\ \frac{\partial n_{Si}}{\partial t} &=& -k(N) \cdot n_{O_2} \cdot n_{Si} & \\ \frac{\partial n_{SiO_2}}{\partial t} &=& k(N) \cdot n_{O_2} \cdot n_{Si} & \end{array} \right. \tag{6}$$

The result is therefore a model closed to the dry oxidation except that the reaction rate k($_N$) between the molecular oxygen and silicon is dependent of the incoporated nitrogen. However, the influence of nitrogen can not be described as the standard dopants. We propose that the reaction rate is governed by the competition between the incororation of nitrogen (nitridation) and by the nitrogen removal (for example by atomic oxygen). This assumption leads to the additiion of time dependent part in the expression of the reaction rate. The compact model has been calibrated and confronted to several experiments (see figure 56). Left alone,

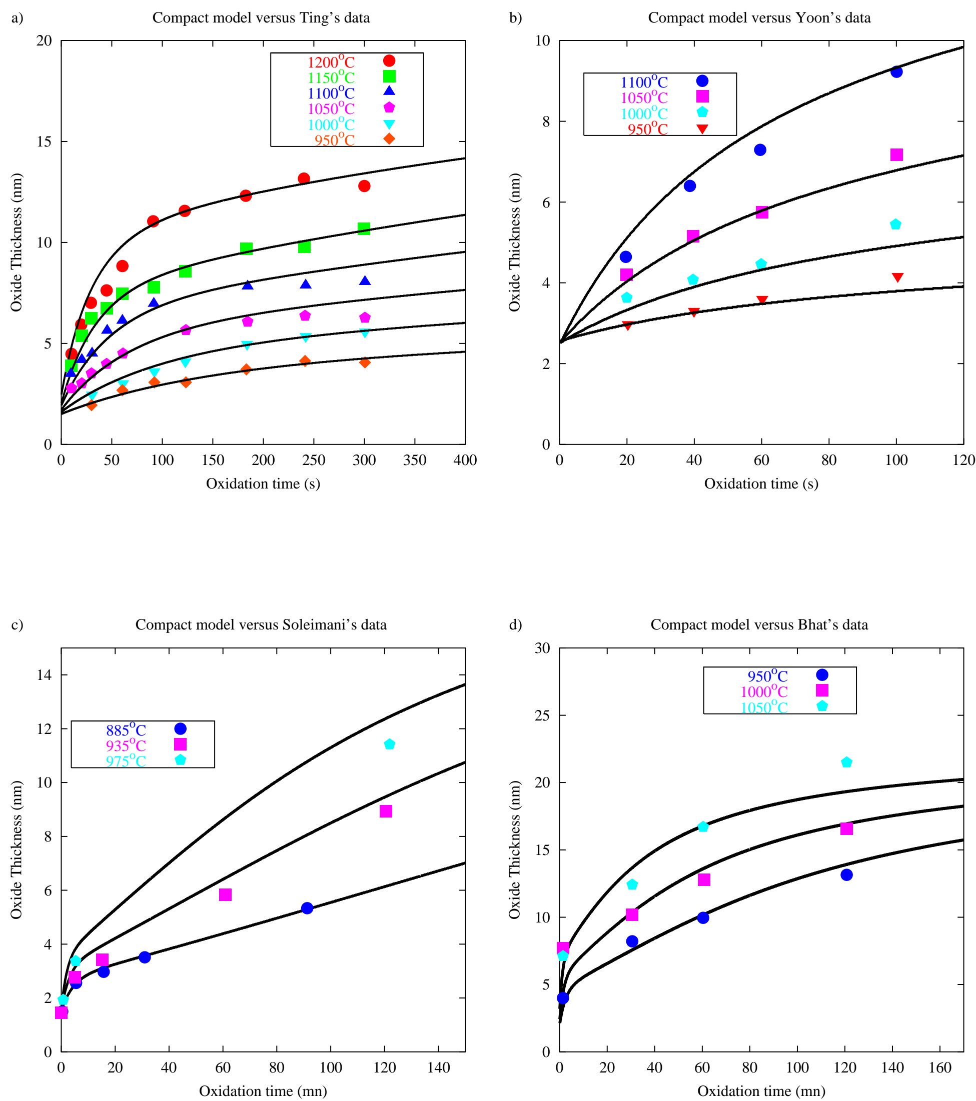

Figure 56: Comparison between the compact model and the experimental kinetics of TING [94] (Fig. 56 .a), YOON [96](Fig. 56.b), SOLEIMANI [97](Fig. 56.c) and BHAT [95](Fig. 56.d)

the initial oxide thickness, the compact model has been able to simulate both the thin and the self-limited regime.

Conclusion

We have presented a compact models to simulate the gas phase decomposition and the oxide growth during an N_2O oxynitridation. A another complex model (where many reactions are considered) have been also

proposed in order to access to a full NO, N_2O oxynitridation simulation. However many parameters and laws have to be extracted. The objective is to consolidate the modelisation of the interaction of the NO molecule with silicon in order to reach a simulation of the nitrogen profile.

For further information, please contact C. Krzeminski, ISEN (christophe.krzeminski@isen.iemn.univ-lille1.fr).

5.3 High quality Ultra-Thin Oxides by Oxidation of Nitrogen-Implanted Silicon

As the dimensions of modern electronic devices decrease the need for thinner and high quality gate dielectrics becomes more demanding. A variety of techniques has been investigated in order to produce ultrathin oxides, such as thermal oxidation in NH_3, NO or N_2O ambient, RTA in pure N_2 ambient, etc. One of these techniques is the oxidation of nitrogen - implanted silicon. Some of the main advantages of N_2 implantation for the formation of thin gate oxides are (some may also apply for different techniques):

(a) The formation of thin gate oxides using high thermal budget. The retardation in oxidation kinetics is attributed to the formation of a nitrogen layer at the SiO_2/Si interface.

(b) Improved electrical characteristics of the resulting oxides as reduction of interface states density.

(c) The suppression of boron penetration from the polysilicon gate into the MOS device channel area, due to the presence of nitrogen in Si/SiO_2 interface prevents this penetration by reducing the boron diffusion coefficient in the gate dielectric.

(d) The ability to create different gate oxide thicknesses across the same wafer using the same thermal budget. This method does not require the masking of the gate oxide during oxidation , which could lead to reduction of its quality.

One of the important disadvantages of the use of nitrogen implantation in silicon as method of growing ultrathin, reliable gate oxides is the formation of dislocation loops in the silicon substrate, which strongly affects the device performance. In order to find a defect free process window a systematic study was performed on the influence of nitrogen implantation energy on oxide growth and on extended defect formation in the silicon substrate [98]. Nitrogen (N_2) was implanted in a wide range of energies (3-150 keV) and doses (5×10^{13} cm^{-2} - 1×10^{15} cm^{-2}) and oxidations were performed at a variety of temperatures (800-900°C) and time intervals. A general result is that the reduction of the oxidation rate decreases as the implantation energy decreases (for every dose and temperature) and consequently nitrogen is implanted closer to the silicon surface, as shown in 57, with the greatest difference observed between the 3 and 25 KeV. Responsible for the above phenomenon is nitrogen out-diffusion, which is more effective as nitrogen has been placed closer to the surface. On the other hand we observed that very low energy nitrogen implantation (3KeV) offers the advantages of a full absence of extended defects in the silicon substrate for all combinations of dose and temperature used. This is true even for high dose implants such as 1×10^{15} cm^{-2} , as can be seen in figure 57, compared to medium energy implant which results in defect formation under the same oxidation conditions, even at much lower implantation doses. A key role for the above result plays the proximity of the silicon surface to the dislocation loop band (of the order of 5 nm), which causes the dissolution of the defects even from the early stage of the oxidation process.

As we have reported previously, the reduction in oxide thickness decreases as the implantation energy decreases and the nitrogen profile is closer to the silicon surface. This was attributed to nitrogen out-diffusion, which is more efficient when nitrogen is placed closer to the surface. In order to support this explanation

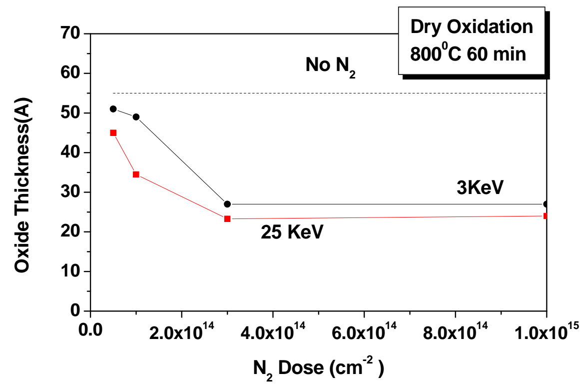

Figure 57: Influence of implantation energy on oxide growth in nitrogen implanted silicon.

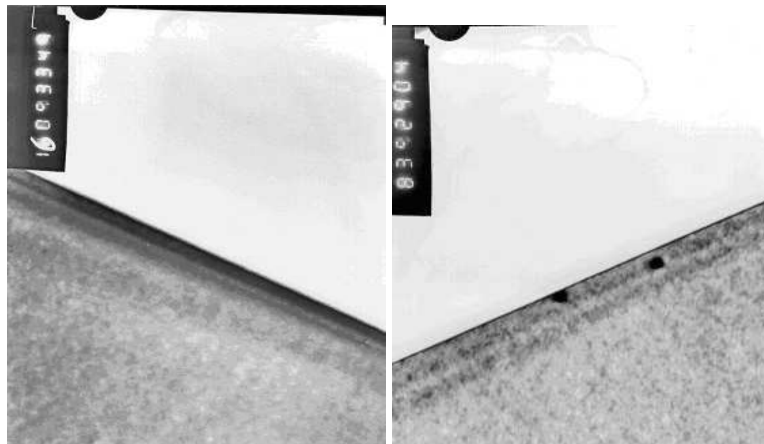

Figure 58: TEM cross section of nitrogen implanted silicon a) E=3KeV, Dose= 1×10^{15} cm^{-2} and b) E=25KeV, Dose= 3×10^{14} cm^{-2}. We observe the full absence of extented defects in the first case.

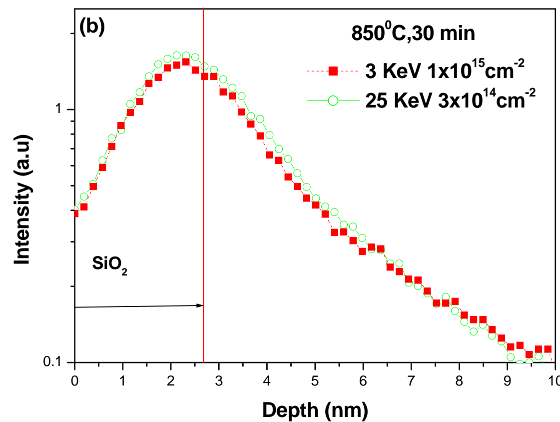

Figure 59: Final nitrogen distribution within the ultrathin oxides of equal thickness formed under the same oxidation conditions using very low (3KeV) and medium (25KeV) implantation energy.

a SIMS study was performed in order to reveal the nitrogen distribution within ultrathin oxides of equal thickness formed at different implantation conditions [99]. Nitrogen distribution was evaluated at INFM by means of a ION-TOF CAMECA IV dual beam ToF-SIMS. In order to avoid trasition phenomena in the SIMS measurements, and improve the quality of the measurements, a capping layer of amorphous silicon (10nm) was deposited by sputtering at room temperature. Some results of the SIMS analysis are shown in Figure 59. Although quantification of the nitrogen content within these ultrathin oxides was not possible, qualitative results could be obtained with accuracy. It was found that pairs of oxides grown at the same conditions and having the same oxide thickness exhibit similar final nitrogen distributions (although they were implanted with different nitrogen condirions). This explains the fact that their final thickness is the same under the oxidation conditions examined, which supports our previous results that formation of ultrathin oxides of similar thickness requires an implantation dose in the case of 3 keV N_2 implanted silicon three times as high as the 25 keV case due to a more effective nitrogen out - diffusion.

In addition in order to investigate the influence of N_2 ion implant energy on the electrical properties of the growing thin oxide layers, Al/SiO_2/p-Si MOS (Metal - Oxide - Semiconductor) capacitors were fabricated on both medium and low energy N_2-implanted samples [100]. We found out that ultrathin oxides grown on very low energy implanted silicon substrates exhibit lower interface state density and leakage currents as shown in Figure 60. Since the nitrogen distributions in the 3 and 25 keV - implanted samples were identical improved electrical properties of the 3 keV case are attributed to the lower interfacial damage and the absence of extended defects in the silicon substrate [101].

For further information, please contact C. Tsamis, IMEL/NCSR ”Demokritos” (C.Tsamis@imel.demokritos.gr).

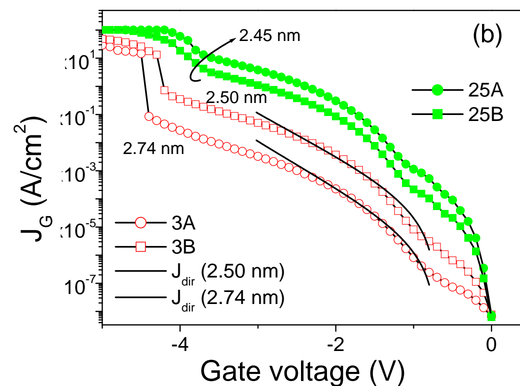

Figure 60: Measured gate current of the Al gate MOS diodes biased in accumulation. Gate oxides are grown on 25 or 3KeV N_2 implanted p-type Si substrates at 800°C for 60 min (pair of samples A) or 850°C for 30 min (pair of samples B).

6 Software development

FRENDTECH was initiated to provide missing models requested by the semiconductor industry for front-end simulation of silicon devices. As a partner of the FRENDTECH team, Integrated Systems Engineering AG (ISE) supported the implementation of the new models in the process simulator FLOOPS-ISE and made five important models available for customers of ISE TCAD 10.0 [102], which has been released in October 2004.

The FRENDTECH defect or TED model is fully integrated in the FLOOPS-ISE model library as well as the model for carbon diffusion and clustering, while the boron-interstitial cluster (BIC) model is partially implemented. The model for indium-carbon pairing is available as a demo example for the implementation of a dopant-dopant interaction. Finally, the model for dry oxidation is implemented as a stand-alone script which allows the calculation of oxide thickness.

In addition to the developed diffusion and activation models, ISE is evaluating the diffusion parameters for point defects and dopants that were used in the FRENDTECH project to be introduced in ISE Advanced Calibration, the standard process calibration for FLOOPS-ISE.

During the FRENDTECH project, ISE has developed a powerful calibration environment for computer aided calibration with secondary ion mass spectrometry (SIMS) data. It has initially been released as part of ISE's TCAD Fab Package 8.5 and will be available as a stand-alone calibration kit for ISE's framework software GENESISe by the end of 2004.

FRENDTECH Defect Model

The FRENDTECH defect model [103] is a physically motivated approach to account for the spatial and temporal evolution of interstitial clusters in ion-implanted silicon. It describes the atom-by-atom growth and dissolution of small and extended self-interstitial agglomerates. Ion implantation is known to generate excess self-interstitials in addition to the injected impurities. These point defects enhance the transient diffusion of certain dopants by forming mobile dopant-interstitial pairs. An effect that counteracts the transient-enhanced

diffusion (TED) is the clustering of self-interstitials to inactive and immobile agglomerates. First, small self-interstitial clusters are formed with up to nine silicon atoms. Extended self-interstitial clusters are then generated from the small clusters through Ostwald ripening by trapping free interstitials to shape defects such as 113 defects and dislocation loops. The implemented model takes into account the different geometries and the formation energies of small clusters and 113 defects, and allows an extension to include dislocation loops.

Since the extended defects expand to sizes of up to several thousand atoms, a method needed to be developed for fast simulation with a reduced number of equations to make the implementation into FLOOPS-ISE possible. FRENDTECH partners proposed a reduction of equations by combining the master equation with a Fokker-Planck modeling [104]. With this method, the fluctuations of the formation energies of the small defects are fully respected, but the smooth evolution of the properties of the larger defects is capitalized for interpolation. The reduction barely affects the prediction of the self-interstitial supersaturation maintained by the extended defects.

FRENDTECH Carbon Model

Carbon has appeared in fabrication processes of integrated systems. Consequently, there is a need to model its evolution in silicon. It has been reported that high carbon concentrations are responsible for a retardation of interstitial-mediated dopant diffusion (for example, boron) and for an enhancement of vacancy-mediated dopant diffusion (for example, antimony). Within FRENDTECH, N. E. B. Cowern and B. Colombeau met the challenge of formulating a model for carbon diffusion and activation [105]. They suggested a five-stream carbon diffusion model with a dominating interstitial kick-out mechanism. The influence of the dissociative Frank-Turnbull mechanism is minor. For high concentrations, carbon clustering with interstitials inevitably must be considered.

The model is the default model for carbon diffusion in FLOOPS-ISE 10.0. The kick-out mechanism is always switched on. Optionally, users may enable the Frank-Turnbull mechanism and the carbon interstitial clustering model if needed.

A. La Magna et al. [106] studied the influence of carbon on indium diffusion and activation in silicon. Besides the kick-out-type model for the defect-driven migration of both species, they assumed that indium-carbon pairs can form. In agreement with experimental data, the simulation predicts that carbon co-implantation increases the electrical activation of indium, while the indium diffusion can be limited by the interstitial and, eventually, indium trapping by carbon.

The modeling of the indium-carbon pair formation has been implemented as an FLOOPS-ISE example for the FRENDTECH examples library of release 10.0.

FRENDTECH BIC model

The boron-interstitial cluster model of FLOOPS-ISE 10.0 is not fully equal to the one presented by C. Ortiz et al. (see Section 3.7) within FRENDTECH. All reactions are included, but the implemented model does not take into account the charge states of the boron-interstitial agglomerates. ISE plans to make available the binding energies and charge statement treatment of the BIC model of FRENDTECH at a later stage. So far, the BIC model has proved to give excellent results for boron marker layer experiments. The calibration of the model for ultra shallow junction profiles is still ongoing.

Summary

By the end of FRENDTECH, five models are implemented in the commercial process simulator FLOOPS-ISE. These models are ready for being used by dozens of companies and hundreds of universities. As the perhaps most remarkable achievement, the physics-based model for defect kinetics has been fully integrated in the FLOOPS-ISE library and successfully applied in 1D and 2D simulations. It may become accepted as the most accurate model for TED in commercial TCAD software.

7 Publications of the consortium

Published Papers

1. J. M. Bonar, M. S. A. Karunaratne, R. W. Price, H. A. W. El-Mubarek, J. Zhang, A. F. W. Willoughby, P. Ashburn: “The effect of defect injection on B in SiGeC”, Third International Conference SiGe(C) Epitaxy and Heterostructures, 83-85 (2002).

2. J.M. Bonar, A. H. Dan, M. S. A. Karunaratne, A.F.W. Willoughby, M. G. Dowsett, R. J. H. Morris, W. Lerch: “RTA defect injection for analysis of B and Sb diffusion in Si and SiGe”, 4th International Conference on Materials for Microelectronics and Nanoengineering 169-170, London, UK: IOM Communications Ltd (2002).

3. F. Cristiano, B. Colombeau, B. de Mauduit, C. Bonafos, G. Benassayag, A. Claverie: “Thermal Evolution of Extrinsic Defects in Ion Implanted Silicon: Current Understanding and Modelling (invited)”, Mat. Res. Soc. Symp. Proc. 717, “Silicon Front-End Junction Formation Technologies”, edited by D. F. Downey, M. E. Law, A. P. Claverie, M. J., Rendon, C5.7.1-C5.7.12 (2002).

4. C. Tsamis, D. Skarlatos, I. Raptis, D. Tsoukalas, P. Calvo, B. Colombeau, F. Cristiano, A. Claverie: “Annealing behavior of locally confined dislocation loops under inert and oxidizing ambient”, Mat. Res. Soc. Symp. Proc. 717, “Silicon Front-End Junction Formation Technologies”, edited by D. F. Downey, M. E. Law, A. P. Claverie, M. J., Rendon, C5.8.1-C5.8.6 (2002).

5. A. Claverie, F. Cristiano, B. Colombeau, E. Scheid, B. De Mauduit: “Thermal Evolution of Interstitial Defects in Implanted Silicon (invited)”, Proceedings of the 14th International Conference on Ion Implantation Technology, 538-543 (2002).

6. D. Skarlatos, C. Tsamis, D. Tsoukalas: “Oxidation of nitrogen-implanted silicon: Energy dependence of oxide growth and defect characterization of the silicon substrate”, J. Appl. Phys. 93(3), 1832-1838 (2003).

7. A. Claverie, B. Colombeau, B. De Mauduit, C. Bonafos, X. Hebras, G. Ben Assayag, F. Cristiano: “Extended defects in shallow implants (invited)”, Appl. Phys. A 76, 1025-1033 (2003).

8. X. Hebras, F. Cristiano, N. Cherkashin, W. Lerch, S. Paul, B. Pawlak, R. Surdeanu, A. Claverie: “Structure and thermal evolution of small clusters found in ultra low energy high dose boron implanted silicon”, Electrochemical Society Proceedings 2003-14 “Advanced Short-Time Thermal Processing for Si-Based CMOS Devices”, edited by F. Roozeboom, E. Gusev, L.J. Chen, M.C. Ozturk, D.L. Kwong, P.J. Timans, 67-72 (2003).

9. A. Claverie, F. Christiano, B. Colombeau, X. Hebras, P. Calvo, N. Cherakshin, E. Scheid, B. de Mauduit: "Relation between thermal evolution of interstitial defects and transient enhanced diffusion in silicon (invited)", Electrochemical Society Proceedings 2003-14 "Advanced Short-Time Thermal Processing for Si-Based CMOS Devices", edited by F. Roozeboom, E. Gusev, L.J. Chen, M.C. Ozturk, D.L. Kwong, P.J. Timans, 73-82 (2003).

10. S. Scalese, M. Italia, A. La Magna, G. Mannino, V. Privitera, M. Bersani, D. Giubertoni, M. Barozzi, S. Solmi, P. Pichler: "Diffusion and electrical activation of indium in silicon", J. Appl. Phys. 93(12), 9773-9782 (2003).

11. P. Deák, A. Gali, A Sólyom, P. Ordejón, K. Kamaráas, and G. Battistig: "Studies of boron-interstitial clusters in Si", J. Phys.: Condens. Matter 15, 4967-4977 (2003).

12. B. Colombeau, N. E. B. Cowern, F. Cristiano, P. Calvo, N. Cherkashin, Y. Lamrani, and A. Claverie: "Time evolution of the depth profile of 113 defects during transient enhanced diffusion in silicon", Appl. Phys. Lett. 83(10), 1953-1955 (2003).

13. N. E. B. Cowern, B. Colombeau, E. Lampin, F. Cristiano, A. Claverie, Y. Lamrani, R. Duffy, V. Venezia, A. Heringa, C. C. Wang, C. Zechner: "Physics-Based Diffusion Simulations for Preamorphized Ultrashallow Junctions", Mat. Res. Soc. Symp. Proc. 765, "CMOS Front-End Materials and Process Technology", edited by T.-J. King, B. Yu, R. J. P. Lander, S. Saito, D6.8.1-D6.8.6 (2003).

14. S. Scalese, A. La Magna, G. Mannino, V. Privitera, M. Bersani, D. Giubertoni, S. Solmi, P. Pichler: "Indium in silicon: a study on diffusion and electrical activation", Mat. Res. Soc. Symp. Proc. 765, "CMOS Front-End Materials and Process Technology", edited by T.-J. King, B. Yu, R. J. P. Lander, S. Saito, D6.13.1-D6.13.6 (2003).

15. S. Uppal, A. F. W. Willoughby, J. M. Bonar, N. E. B. Cowern, R. J. H. Morris, M. Bollani: "Diffusion of Boron in germanium and $Si_{1-x}Ge_x$ (x¿50%) alloys", Mat. Res. Soc. Symp. Proc. 765, "CMOS Front-End Materials and Process Technology", edited by T.-J. King, B. Yu, R. J. P. Lander, S. Saito, D6.16.1-D6.16.6 (2003).

16. A. La Magna, S. Scalese, P. Alippi, G. Mannino, V. Privitera, M. Bersani, C. Zechner: "Role of the indium-carbon interaction on In diffusion and activation in Si", Appl. Phys. Lett. 83(10), 1956-1958 (2003).

17. E. Lampin, F. Cristiano, Y. Lamrani, A. Claverie, B. Colombeau, N. E. B. Cowern: "Prediction of boron transient enhanced diffusion through the atom-by-atom modeling of extended defects", J. Appl. Phys. 94(12), 7520-7525 (2003).

18. P. Deák, Á. Gali, P. Pichler, H. Ryssel: "Quantum Mechanical Studies of Boron Clustering in Silicon", E. Krause, W. Jäger, M. Resch: High Performance Computing in Science and Engineering '03, Berlin, Germany: Springer, 381-392 (2003).

19. F. Cristiano, X. Hebras, N. Cherkashin, A. Claverie, W. Lerch, S. Paul: "Clusters Formation in Ultralow-Energy High-Dose Boron-Implanted Silicon", Appl. Phys. Lett. 83(26), 5407-5409, (2003).

20. F. Cristiano, N. Cherkashin, X. Hebras, P. Calvo, Y. Lamrani, E. Scheid, B. de Mauduit, B. Colombeau, W. Lerch, S. Paul, A. Claverie: "Ion Beam Induced Defects in Crystalline Silicon", Nuclear Instruments and Methods in Physics Research B 216, 46-56 (2004).

21. D. Skarlatos, M. Perego, C. Tsamis, S. Ferrari, M. Fanciulli, D. Tsoukalas: “Nitrogen Distribution during Oxidation of Low and Medium Energy Nitrogen-Implanted Silicon”, Nuclear Instruments and Methods in Physics Research B 216, 75-79 (2004).

22. B. Colombeau, N. E. B. Cowern, F. Cristiano, P. Calvo, Y. Lamrani, N. Cherkashin, E. Lampin, A. Claverie: “Depth Dependence of Defect Evolution and TED during Annealing”, Nuclear Instruments and Methods in Physics Research B 216, 90-94 (2004).

23. E. Lampin, F. Cristiano, Y. Lamrani, B. Colombeau: “Coupling of Atom-by-Atom Calculations of Extended Defects with B Kick-Out Equations: Application to the Simulation of Boron TED”, Nuclear Instruments and Methods in Physics Research B 216, 95-99 (2004).

24. P. Calvo, A. Claverie, N. Cherkashin, B. Colombeau, Y. Lamrani, B. de Mauduit, F. Cristiano: “Thermal Evolution of 113 Defects in Silicon: Transformation against Dissolution”, Nuclear Instruments and Methods in Physics Research B 216, 173-177 (2004).

25. Y. Lamrani, F. Cristiano, B. Colombeau, E. Scheid, P. Calvo, H. Schäfer, A. Claverie: “Direct Evidence of the Recombination of Silicon Interstitial Atoms at the Silicon Surface”, Nuclear Instruments and Methods in Physics Research B 216, 281-285 (2004).

26. P. Alippi, A. La Magna, S. Scalese, V. Privitera: “Energetics and Diffusivity of Indium-Related Defects in Silicon”, Phys. Rev. B 69, 085213, (2004).

27. B. J. Pawlak, R. Surdeanu, B. Colombeau, A. J. Smith, N. E. B. Cowern, R. Lindsay, W. Vandervorst, B. Brijs, O. Richard, F. Cristiano: “Evidence on the Mechanism of Boron Deactivation in Ge-Preamorphized Ultrashallow Junctions”, Appl. Phys. Lett. 84(12), 2055-2057 (2004).

28. G. Mannino, V. Privitera, S. Scalese, S. Libertino, E. Napolitani, P. Pichler, N. E. B. Cowern: “Effect of Oxygen on the Diffusion of Nitrogen Implanted in Silicon”, Electrochemical and Solid State Letters 7(8), G161-G163 (2004).

29. D. Skarlatos, E. Kapetanakis, P. Normand, C. Tsamis, M. Perego, S. Ferrari, M. Fanciulli, D. Tsoukalas: “Oxidation of Nitrogen-Implanted Silicon: Comparison of Nitrogen Distribution and Electrical Properties of Oxides Formed by Very Low and Medium Energy N_2^+ Implantation”, J. Appl. Phys. 96(1), 300-309 (2004).

30. S. Uppal, A. F. W. Willoughby, J. M. Bonar, J. Zhang: “Evidence for a vacancy and interstitial mediated diffusion of As in Si and $Si_{0.9}Ge_{0.1}$”, Appl. Phys. Lett. 84(4), 552-554 (2004).

31. S. Uppal, A. F. W. Willoughby, J. M. Bonar, N. E. B. Cowern, T. Grasby, R. J. H. Morris, M. G. Dowsett: “Diffusion of boron in germanium at 800-900C”, J. Appl. Phys. 96(3), 1376-1380 (2004).

32. B. Colombeau, A.J. Smith, N.E.B. Cowern, B.J. Pawlak, F. Cristiano, R. Duffy, A. Claverie, C.J. Ortiz, P. Pichler, E. Lampin, C. Zechner: “Current Understanding and Modeling of B Diffusion and Activation Anomalies in Preamorphized Ultra-Shallow Junctions (invited)”, Mat. Res. Soc. Symp. Proc. 810, “Silicon Front-End Junction Formation-Physics and Technology”, edited by P. Pichler, A. Claverie, R. Lindsay, M. Orlowski, W. Windl, C3.6.1-C3.6.12 (2004).

33. N. Cherkashin, P. Calvo, F. Cristiano, B. de Mauduit, A. Claverie: “On the “Life” of 113 Defects”, Mat. Res. Soc. Symp. Proc. 810, “Silicon Front-End Junction Formation-Physics and Technology”, edited by P. Pichler, A. Claverie, R. Lindsay, M. Orlowski, W. Windl, C3.7.1-C3.7.6 (2004).

34. P. Alippi, A. La Magna, S. Scalese, V. Privitera: “Indium in Silicon: Interactions With Native Defects and with C Impurit”, Mat. Res. Soc. Symp. Proc. 810, “Silicon Front-End Junction Formation-Physics and Technology”, edited by P. Pichler, A. Claverie, R. Lindsay, M. Orlowski, W. Windl, C6.3.1-C6.3.5 (2004).

35. C. J. Ortiz, P. Pichler, V. Haublein, G. Mannino, S. Scalese, V. Privitera, S. Solmi, W. Lerch: “Boron-Interstitial Cluster Kinetics: Extraction of Binding Energies From Dedicated Experiments”, Mat. Res. Soc. Symp. Proc. 810, “Silicon Front-End Junction Formation-Physics and Technology”, edited by P. Pichler, A. Claverie, R. Lindsay, M. Orlowski, W. Windl, C7.1.1-C7.1.6 (2004).

36. S. Scalese, V. Privitera, M. Italia, A. La Magna, P. Alippi, L. Renna: “Role of C and Ge in the Electrical Activation of In Implanted in Silicon”, Mat. Res. Soc. Symp. Proc. 810, “Silicon Front-End Junction Formation-Physics and Technology”, edited by P. Pichler, A. Claverie, R. Lindsay, M. Orlowski, W. Windl, C8.7.1-C8.7.6 (2004).

37. S. Uppal, J. M. Bonar, J. Zhang, A. F. W. Willoughby: “Arsenic Diffusion in Si and $Si_{0.9}Ge_{0.1}$ Alloys: Effect of Defect Injection”, Mat. Res. Soc. Symp. Proc. 810, “Silicon Front-End Junc Formation-Physics and Technology”, edited by P. Pichler, A. Claverie, R. Lindsay, M. Orlowski, W. Windl, C9.3.1-C9.3.6 (2004).

Accepted Publications and Presentations

1. P. Alippi, A. La Magna, S. Scalese, V. Privitera: “Theoretical Investigations on Indium-Related Defects in Silicon”, Proceedings of 3rd International Conference on Computational Modeling and Simulation of Materials CIMTEC 2004, Acireale, May 30th- June 4th 2004, Techna Group, Faenza, Italy, (in print).

2. C. J. Ortiz, P. Pichler, T. Führer, F. Cristiano, A. Claverie, B. Colombeau, and N. E. B. Cowern, “A physically-based model for the spatial and temporal evolution of self-interstitial agglomerates in ion implanted silicon,”, J. Appl. Phys., vol. 96, November 2004 (in print).

3. C.J. Ortiz, F. Cristiano, B. Colombeau, A. Claverie, N.E.B. Cowern: “Modeling of Extrinsic Extended Defect Evolution in Ion-Implanted Silicon upon Thermal Annealing”, Materials Science and Engineering B (in print).

4. P. Pichler, C. J. Ortiz, B. Colombeau, N.E.B. Cowern, E. Lampin, A. Claverie, F. Cristiano, W. Lerch, S. Paul: “On the Modeling of Transient Diffusion and Activation of Boron during Post-Implantation Annealing”, Invited presentation at the IEDM 2004, San Francisco, USA, December 12-15, 2004.

5. B. Colombeau, A. J. Smith, N. E. B. Cowern, W. Lerch, S. Paul, B. J. Pawlak, F. Cristiano, X. Hebras, C. Ortiz, P. Pichler: “Electrical Deactivation and Diffusion of Boron in Preamorphized Ultrashallow Junctions: Interstitial Transport and F Co-Implant Control”, accepted for presentation at the IEDM 2004, San Francisco, USA, December 12-15, 2004.

6. C. J. Ortiz, P. Pichler, W. Lerch, S. Paul, G. Mannino, S. Scalese: “Predictive Simulation of the Formation of Ultra-Shallow Junctions by Non-Amorphizing Boron Implantation”, invited presentation at the conference on “Recent Advances in Ultra Shallow Junctions”, Povo, Italy, November 24-25, 2004.

Submitted Publications

1. S. Scalese, A. La Magna, M. Italia, S. Pannitteri, V. Privitera, R. Duffy, M. J. P. Hopstaken: "Quantitative measurements of two-dimensional ultra-shallow B profiles in Si by selective chemical etching", submitted to J. Electrochem. Soc.

2. Peter Deák, A. Gali, A. Sólyom, A. Buruzs, and T. Frauenheim: "Electronic Strutcure of Boron-Interstitial Clusters in Silicon", submitted to J. Phys. C: Condens. Matter.

8 Contributors

Fraunhofer IISB, Erlangen, Germany

Schottkystrasse 10, 91058 Erlangen, Germany

Dr. Peter Pichler
Dr. Christophe Ortiz
Mr. Gerald Schneider
Dr. Dorothée Stiebel

CEMES/CNRS, Toulouse, France

CEMES/CNRS: 29 rue Jeanne Marvig, BP 94347, 31055 Toulouse Cedex 4, France

Dr. Alain Claverie
Dr. Gerard Ben Assayag
Dr. Caroline Bonafos
Dr. D. Chassaing
Dr. Nikolay Cherkashin
Dr. Bernadette de Mauduit
Dr. L. Vincent

LAAS/CNRS, Toulouse, France

LAAS/CNRS: 7 avenue du Colonel Roche, 31077 Toulouse Cedex 4, France

Dr. Filadelfio Cristiano (LAAS)

CNR-IMM, Catania, Italy

Stradale Primosole 50, 95121 Catania, Italy

Dr. Vittorio Privitera
Dr. Paola Alippi
Dr. Antonio La Magna
Dr. Giovanni Mannino
Dr. Silvia Scalese

IEMN, Lille, France

IEMN-ISEN, Avenue Poincaré, BP 69, 59652 Villeneuve d'Ascq Cedex, France

Dr. Evelyne Lampin
Dr. Christophe Krzeminski
Dr. Vincent Senez

IMEL/NCSR "Demokritos", Athens, Greece

15310 Aghia Paraskevi, Greece

Prof. Dimitris Tsoukalas
Dr. Christos Tsamis
Dr. Dimitris Skarlatos
Dr. D. Davazoglu

ISE AG, Zurich, Switzerland

Affolternstrasse 52, 8050 Zurich, Switzerland

Dr. Christoph Zechner
Dr. Ibrahim Avci
Dr. Hans-Petter Lien
Dr. Mark Johnson
Dr. Andreas Scholze
Dr. Nikolas Zographos

MTA-MFA, Budapest, Hungary

MTA-MFA: P.O. Box 49, 1525 Budapest

Dr. Gabor Battistig
Dr. Ádám Antalné
Dr. István Barsony
Dr. Miklós Fried
Dr. Zoltán Hajnal
Dr. N. Q. Khán
Dr. Tivadar Lohner
Dr. Peter Petrik
Dr. Olivér Polgár
Mr. Béla Varga
Mr. János Volk

Budapest University of Technology and Economics, Budapest, Hungary

Department of Atomic Physics, Budafoki ut 8, 1111 Budapest, Hungary

Prof. Peter Deák
Dr. Ádam Gali

PITS Leuven

Kapeldreef 75, 3001 Leuven, Belgium

Dr. Ray Duffy
Dr. Doombos
Dr. Meunier-Beillard
Dr. Peter Stolk

University of Southampton, UK

Engineering Materials Department, SO17 1BJ Southampton, UK

Prof. Arthur Willoughby
Dr. Janet Bonar
Dr. Suresh Uppal

University of Surrey, UK

Research Chair of Nanoscale Materials Processing, School of Electronics and Physical Sciences, Guildford, Surrey GU2 7XH, UK

Prof. Nick E. B. Cowern
Dr. Benjamin Colombeau

References

[1] `http://www.leb.e-technik.uni-erlangen.de/forsch/techsim/upper/`

[2] D.J. Eaglesham, P.A. Stolk, H.J. Gossmann and J.M. Poate, Appl. Phys. Lett., 65, 2305 (1994).

[3] F.Cristiano, N.Cherkashin, X.Hebras, P.Calvo, Y.Lamrani, E.Scheid, B.de Mauduit, A.Claverie, B.Colombeau, W.Lerch and S.Paul, Nucl. Inst. and Meth. B, 216 (2004) 46

[4] N.Cherkashin, P.Calvo, F.Cristiano, B.de Mauduit and A.Claverie, MRS Spring 2004, MRSSP vol. 810 (2004) 103

[5] P.A. Stolk, H.-J. Gossmann, D.J. Eaglesham, D.C. Jacobson, C.S. Rafferty, G.H. Gilmer, M. Jaraiz, J.M. Poate, H.S. Luftman, T.E. Haynes, J. Appl. Phys. 81, 6031 (1997).

[6] P.Calvo, A.Claverie, N.Cherkashin, B.Colombeau, Y.Lamrani, B.de Mauduit and F.Cristiano, Nucl. Inst. and Meth. B, 216 (2004) 173

[7] A.Claverie, B.Colombeau, B.de Mauduit, C.Bonafos, X.Hebras, G.Ben Assayag and F.Cristiano, Applied Physics A, 76 (2003) 1025-1033

[8] W.Lerch, S.Paul, J.Niess, F.Cristiano, Y.Lamrani, P.Calvo, N.Cherkashin, D.F.Downey and E.A.Arevalo, Proc. Of the 205th Electrochem. Soc. Spring Meeting, San Antonio, 2004, PV 2004-01

[9] F. Cristiano, N. Cherkashin, P. Calvo, Y. Lamrani, X. Hebras, A. Claverie, W. Lerch and S. Paul, Mat. Sci. Eng. B, in press.

[10] N. E. B. Cowern, G. Mannino, P. A. Stolk, F. Roozeboom, H. G. A. Huizing, J. G. M. van Berkum,W. B. de Boer, F. Cristiano, A. Claverie and M. Jaraiz, Phys. Rev. Lett. 82, 4460 (1999).

[11] T. Fühner, A. Erdmann, R. Farkas, B. Tollkühn, and G. Kókai in *EvoWorkshops* (G. R. Raidl et al., eds.), vol. 3005 of *Lecture Notes in Computer Science*, pp. 208–218, Springer, 2004.

[12] N. E. B. Cowern, G. Mannino, P. A. Stolk, F. Roozeboom, H. G. A. Huizing, J. G. M. van Berkum,W. B. de Boer, F. Cristiano, A. Claverie and M. Jaraiz, Phys. Rev. Lett. 82, 4460 (1999).

[13] F.Cristiano, P.Calvo, N.Cherkashin, Y.Lamrani, B.Colombeau, B.de Mauduit and A.Claverie, February 2003.

[14] P.A. Stolk, H.-J. Gossmann, D.J. Eaglesham, D.C. Jacobson, C.S. Rafferty, G.H. Gilmer, M. Jaraiz, J.M. Poate, H.S. Luftman, T.E. Haynes, J. Appl. Phys. 81, 6031 (1997).

[15] A. Claverie, B. Colombeau, B. de Mauduit, C. Bonafos, X. Hebras, G. Ben Assayag and F. Cristiano, Appl. Phys. A, 76 (2003) 1025.

[16] J. Kim, F. Kirchoff et al., Phys. Rev. Lett. 87, 503 (2000).

[17] D.J. Eaglesham, P.A. Stolk, H.J. Gossmann and J.M. Poate, Appl. Phys. Lett., 65, 2305 (1994).

[18] B. Colombeau, N. E. B. Cowern, F. Cristiano, P. Calvo, N. Cherkashin, Y. Lamrani, and A. Claverie, Appl. Phys. Lett., 83 (2003) 1953.

[19] C. J. Ortiz, P. Pichler, T. Fühner, F. Cristiano, A. Claverie, B. Colombeau, and N. E. B. Cowern, "A physically-based model for the spatial and temporal evolution of self-interstitial agglomerates in ion implanted silicon," *J. Appl. Phys.*, vol. 96, (October 2004).

[20] M. Omri, B. de Mauduit and A. Claverie, MRS Symp. Proc., 568 (1999) 219.

[21] V. C. Venezia, R. Kalyanaraman, H. J. Gossmann, C. S. Rafferty and P. Werner, Appl. Phys. Lett., 79 1429 (2001) 1429.

[22] D. R. Lim, C. S. Rafferty and F. P. Klemens, Appl. Phys. Lett., 67 (1995) 2302.

[23] N.E.B Cowern, D. Alquier, M. Omri, A. Claverie and A. Nejim, Nucl. Instr. Meth. in Phys. Res. B, 148 (1999) 257-261.

[24] K. Moller, Kevin S. Jones, and Mark E. Law, Appl. Phys. Lett. 72(20) p2547, (1998)

[25] A. C. King, A. F. Gutierrez, A. F. Saavedra, and K. S. Jones, J. Appl. Phys. 93 (2003) 2449

[26] Y. Lamrani, F. Cristiano, B. Colombeau, E. Scheid, P. Calvo, H. Schafer and A. Claverie, Nucl. Instr. Meth. in Phys. Res. B, 216 (2004) 281-285.

[27] N.E.B. Cowern, K.T.F. Janssen, G.F.A. van de Walle and D.J. Gravesteijn, Phys. Rev. Lett. 65, 2434 (1990).

[28] E. Lampin, F. Cristiano, Y. Lamrani, A. Claverie, B. Colombeau and N. E. B. Cowern, J. Appl. Phys., 94 (2003) 7520.

[29] Y.Kim. H. Z. Massoud, and R. B. Fair, J. Electron. Mater. 18, 143 (1989).

[30] V. Krishnamoorthy, B. Beaudet, K. S. Jones, and D. Venables, Tech. Dig.-Int. Electron Devices Meet. 1997 , 638.

[31] E. Schroer, V. Privitera, F. Priolo, E. Napolitani, and A. Carnera, Appl. Phys. Lett., 76 (21), p. 3058 (2000)

[32] S. Whelan, V. Privitera, G. Mannino, M. Italia, C. Bongiorno, A. La Magna and E. Napolitani, J. Appl. Phys, 90 (8), p. 5997 (1998)

[33] S. Solmi, M. Ferri, M. Bersani, D. Giubertoni and V. Soncini, J. Appl. Phys, 94 (4), p. 4950 (2003)

[34] T. S. Chao, M. C. Liaw, C. H. Chu, C. Y. Chang, C. H. Chien, C. P. Hao and T. F. Lei, Appl. Phys. Lett. **69**, 1781 (1996).

[35] A. Alberti,, F. la Via, S. Ravesi and E. Rimini, Appl. Phys. Lett. **79**, 3419 (2001); A. Alberti, F. la Via and E. Rimini, Appl. Phys. Lett. **81**, 55 (2002)

[36] H. Sawada and K. Kawakami, Phys. Rev. B **62**, 1851 (2000).

[37] P. A. Schultz and R. P. Messmer, Phys. Rev. B **34**, 2532 (1986).

[38] H. Sawada, K. Kawakami, A. Ikari and W. Ohashi, Phys. Rev. B **65**, 075201-1 (2002).

[39] P. A. Schultz and J. S. Nelson, Appl. Phys. Lett. **78**, 736 (2001).

[40] L. S. Adam, M. E. Law, K. S. Jones, O. Dokumaci, C. S. Murthy and S. Hegde, J. Appl. Phys. 87, 2282 (2000)

[41] R. S. Hockett, Appl. Phys. Lett. 54, 1793 (1989).

[42] T. Itoh and T. Abe, Appl. Phys. Lett. 53, 39 (1988).

[43] G. Mannino, V. Privitera, S. Scalese, S. Libertino, E. Napolitani, P. Pichler and N. E. B.Cowern, "Effect of Oxygen on the Diffusion of Nitrogen Implanted in Silicon", Electrochemical and Solid-State Letters **7**, G161-163 (2004).

[44] R. Baron, M. H. Young, J. K. Neeland, O. J. Marsh, Appl. Phys. Lett. **30**, 594 (1977).

[45] S. Scalese, M. Italia, A. La Magna, G. Mannino, V. Privitera, M. Bersani, D. Giubertoni, M. Barozzi, S. Solmi, P. Pichler, J. Appl. Phys. **93**, 9773 (2003).

[46] R. Baron, J. P. Baukus, S. D. Allen, T. C. McGill, M. H. Young, H. Kimura, H. V. Winston, and O. J. marsh, Appl. Phys. Lett. **34**, 257 (1979).

[47] `http://www.tec.ufl.edu/ flooxs`: FLOOPS process simulator, ISE TCAD Release 9.0, User's Manual, ISE AG, Zurich, in print.

[48] P. Alippi, A. La Magna, S. Scalese, V. Privitera, Phys. Rev. B **69**, 085213 (2004).

[49] G. Kresse and J. Hafner, Phys. Rev. B **47**, 558 (1993); *ibidem* **49**, 14251 (1994); G. Kresse and J. Furthmüller, Comput. Mater. Sci. **6**, 15 (1996); Phys. Rev. B **54**, 11169 (1996).

[50] H. Jonsson, G. Mills and K. W. Jacobsen, in "*Classical and Quantum Dynamics in Condensed Phase Simulations*", edited by B. J. Berne, G. Ciccotti and D. F. Coker (World Scientific, 1998).

[51] M. Ramamoorthy, and T. P. Pantelides, Phys. Rev. Lett. **76**, 4753 (1996). J. S. Nelson, P. A. Schultz, and A. F. Wright, Appl. Phys. Lett. **73**, 247 (1998).

[52] A. La Magna, S. Scalese, P. Alippi, G. Mannino, V. Privitera, M. Bersani, and C. Zechner, Appl. Phys. Lett. **83**, 1956 (2003).

[53] C. Spinella, G. D'Arrigo, J. Vac. Sci. Technol. B **18**, 576 (2000).

[54] G. D'Arrigo, C. Spinella, Microsc. Microanal. **6**, 237 (2000).

[55] C. Spinella, V. Raineri, F. La Via, S.U. Campisano, J. Vac. Sci. Technol.B **14** (1), 414 (1996).

[56] C. Spinella, V. Raineri, S.U. Campisano, J. of Electrochem. Soc. **142** (5), 1601 (1995).

[57] A. La Magna, S. Scalese, M. Renna, L. La Magna, S. Coffa, in press on *Computational Modeling and Simulation of Materials*, Proceedings of 3rd International Conference, CIMTEC ed. (2004).

[58] G. Garozzo, A. La Magna, S. Coffa, G. D'Arrigo, N. Parasole, M. Renna, C. Spinella, Comp. Mat. Sci. **24**, 246 (2002).

[59] A. La Magna, G. D'Arrigo, G. Garozzo, C. Spinella, Mat. Sci. Eng B **102**, 43 (2003).

[60] V. Lehmann, *Electrochemical of Silicon*, ed. Wiley - VHC Verlag GmbH (2002).

[61] S. Solmi, M. Bersani, M. Sbetti, J. Lundsgaard Hansen, and A. Nylandsted Larsen, J. Appl. Phys., **88**(8), 4547–4552 (2000).

[62] W. Windl, X.-Y. Liu, and M. P. Masquelier, phys. stat. sol. (b), **226**(1), 37–45 (2001).

[63] J. Yamauchi, N. Aoki, and I. Mizushima, Phys. Rev. B, **63**, 073202 (2001).

[64] W. Windl, IEICE Trans. Electron., **E86-C**(3), 269–275 (2003).

[65] C. J. Ortiz, P. Pichler, V. Häublein, G. Mannino, S. Scalese, V. Privitera, S. Solmi, and W. Lerch, Mat. Res. Soc. Symp. Proc. **810**, C7.1.1–C7.1.6 (2004).

[66] P. Deák, A. Gali, A. Sólyom, P. Ordejón, K. Kamarás, and G. Battistig, J. Phys. C: Condensed Matter, 15, 4767-4977 (2003).

[67] P. Deák, A. Gali, A. Sólyom, A. Buruzs, and Th. Frauenheim, J. Phys. Condens. Matter., to be published (2004).

[68] P. Deák, A. Gali, A. Sólyom, and Th. Frauenheim, Phys. Rev. B, in preparation

[69] C. Liao, Y. Wang and S. Yang, Nucl. Intr. Methods, A422, (1999) 863

[70] J. Liu, X. Lu, X. Wang, W.-K. Chu, Nucl. Intr. Methods, B190 (2002) 107

[71] D. F. Downey, J. W. Chow, E. Ishida, and K. S. Jones, Appl. Phys. Lett. **73**, 1263 (1998)

[72] G. Impellizzeri, J.H.R. dos Santos, S. Mirabella, F. Priolo, E. Napolitani, and A. Camera, Appl. Phys. Lett. **84**, 1862 (2004)

[73] B.J. Pawlak, R. Surdeanu, B. Colombeau, A.J. Smith, N.E.B. Cowern, R. Lindsay, W. Vandervorst, B. Brijs, O. Richard and F. Cristiano, Appl. Phys. Lett., **84**, 2005 (2004)

[74] B. Colombeau, A. Smith, N.E.B. Cowern, B. Pawlak, F. Cristiano, R. Duffy, C. Ortiz, P.Pichler, E. Lampin and C. Zechner, Mat. Res. Soc. Symp. Proc. **810**, C3.6 (2004)

[75] M. Diebel, S. Chakravarthi, S.T. Dunham, C.F. Machala, S. Ekbote, and A. Jain, Mat. Res. Soc. Symp. Proc. **765**, D6.15.1 (2003)

[76] P.J. Simpson, Z. Jenei, P. Asoka-Kumar, R.R. Robison, and M.E. Law, Appl. Phys. Lett. **85**, 1538 (2004)

[77] A. Mokhberi, R. Kasnavi, P.B. Griffin, and J.D. Plummer, Appl. Phys.Lett. **80**, 3530 (2002)

[78] J.M. Jacques, L.S. Robertson, K.S. Jones, M.E. Law, M.Rendon, and J. Bennett, Appl. Phys. Lett. **82**, 3469 (2003)

[79] R. Duffy, V.C. Venezia, A. Heringa, B.J. Pawlak, M.J.P. Hopstaken, G.C.J. Mass, Y. Tamminga, T. Dao, F. Roozeboom and L. Pelaz, Appl. Phys. Lett. **84**, 4283 (2004)

[80] W. Lerch, S. Paul, J. Niess, F. Cristiano, Y. Lamrani, P. Calvo, N. Cherkashin, D.F. Downey, and E.A. Arevalo, Proc. Electrochem. Soc. 2004-01, pp. 90-105, (2004)

[81] W. C. Dunlap, Jr., Physical Review **94**, 1531 (1954).

[82] W. Meer and D. Pommerring, Zeitschrift für Angewandte Physik, **23**, 369 (1967).

[83] Front End Process part, International Technology Roadmap for Semiconductors, 2003.

[84] C. HOBBS *et al*.,"Fermi Level Pinning at the PolySi/metal Oxide Interface Part I & II", *IEEE transactions on Electron Devices*,Vol. 51, No 6, 2004.

[85] B. TAVEL,"Thin oxynitride solution for digital and mixed-signal 65nm CMOS platform", *International electron Device Meeting*, 27.6.1, p. 643, 2003

[86] http://www.appliedmaterials.com/products/fep_gatestack.html

[87] M. E. LAW,"Process modeling for future technologies", *IBM J. Res. and Dev.*, Vol. 46, No 2/3, 2002.

[88] M. HOUSSA, C. PARTHASARATHY, N. ESPREUX, J. L. AUTRAN and N. REVIL, "Impact of Nitrogen on Negative Bias Temperature Instability in p-Channel MOSFETs", *Electrochemical and Solid-State Letters*, Vol6, No. 12, G146, 2003.

[89] M. A. ALAM,"A critical Examination of the Mechanics of dynamic NBTI for pMOSFETs", *International electron Device Meeting*, 14.4.1, p. 345, 2003

[90] Y.-H. LEE, N. MIELKE, B. SABI, S. STADLER, R. NACHMAN and S. HU,"Effect of pMOS Bias-Temperature Instability on Circuit Reliability Performance", *International electron Device Meeting* , 14.6.1, p. 353, 2003

[91] S. INABA et al. ,"Device Performance of Sub-50nm CMOS with Ultra-Thin Plasma Nitrided Gate Dielectrics", *International electron Device Meeting*, 27.4.1, p. 651, 2002.

[92] K. MURAOKA, K. KURIHARA, N. YASUDA and H. SATAKE, *Journal of Applied Physics*, " Optimum structure of deposited ultrathin silicon oxynitride film to minize leakage current", Vol. 94, No 3, p 2038, 2003.

[93] K. A. ELLIS and R. A. BUHRMAN, "Nitrous oxide processing for silicon oxynitride gate dielectrics",*IBM Journal of Research and Development*, Vol. 43, No 3, 1999.

[94] W. TING, H. WANG, J. LEE and D. L. KWONG,"Growth Kinetics of Ultrathin SiO_2 Films Fabricated by Rapid Thermal Oxidation of Si substrates in N_2O, *J. Appl. Phys.*, Vol. 70, No 2, p 1072-1074, 1991.

[95] M. BHAT, H. JIA and D. L. KWONG, "Growth Kinetics of oxides during furnace oxidation of Si in N_2O ambient", *J. Appl. Phys.*, Vol. 78, No 4, 1995.

[96] G. W. YOON, A. B. JOSHI, J. AHN and D. L. KWONG,"Thickness uniformity and electrical properties of ultrathin gate oxides grown in N_2O ambient and by rapid thermal processing", *J. Appl. Phys.*, Vol. 72, No 12, 1982.

[97] H. R. SOLEIMANI, A. PHILIPOSSIAN and B. DOYLE, "A study of the growth Kinetics of SiO_2 in N_2O", *Technical Digest of the 1992 IEDM conference*, p631., 1992

[98] D. Skarlatos, C. Tsamis and D. Tsoukalas, Oxidation of nitrogen - implanted silicon : energy dependence of oxide growth and defect characterisation of the silicon substrate, J. Applied Physics, 93 (3), p. 1832-1838 (2003)

[99] D. Skarlatos, M. Perego, C. Tsamis, S. Ferrari, M. Fanciulli, D. Tsoukalas, Nitrogen distribution during oxidation of low and medium energy nitrogen-implanted silicon, Nuclear Instruments and Methods in Physics Research section b-beam interactions with materials and atoms , 216: 75-79 Feb 2004

[100] E. Kapetanakis, D. Skarlatos, C. Tsamis, P. Normand and D. Tsoukalas, Influence of implantation energy on the electrical properties of ultra-thin gate oxides grown on nitrogen implanted Si-substrates, Appl. Physics Lett., 82 (26), p.4764-4766 (2003)

[101] D. Skarlatos, E. Kapetanakis , P. Normand, C. Tsamis , M. Perego , S. Ferrari, M. Fanciulli, D. Tsoukalas , Oxidation of nitrogen-implanted silicon: Comparison of nitrogen distribution and electrical properties of oxides formed by very low and medium energy N_2 implantation, Journal of Applied Physics, 96 (1): 300-309 Jul 1 2004

[102] ISE TCAD Release 10.0, User s Manual, Integrated Systems Engineering Zurich, Switzerland, 2004.

[103] C. J. Ortiz et al., ”A Physically-Based Model for the Spatial and Temporal Evolution of Self-Interstitial Agglomerates in Ion-Implanted Silicon,” submitted to Journal of Applied Physics, 2004.

[104] E. Lampin et al., ”Combined master equations and Fokker-Planck modeling of the kinetics of extended defects in Si,” submitted to Applied Physics Letters, 2004.

[105] B. Colombeau and N. E. B. Cowern, ”Modeling of the chemical-pump effect and C clustering,” to be published in Semiconductor Science and Technology, 2004.

[106] A. La Magna et al., ”Role of the indium-carbon interaction on In diffusion and activation in Si,” Applied Physics Letters, vol. 83, no. 10, pp. 1956-1958, 2003.